TECHNISCHE
UNIVERSITÄT
WIEN

Critical Current Properties and Flux Pinning in Ba122 Superconductors

DISSERTATION

zur Erlangung des akademischen Grades
Doktor der technischen Wissenschaften

eingereicht von

Dipl.-Ing. Daniel Kagerbauer

Matrikelnummer: 1025417

eingereicht an der Fakultät für Physik der Technischen Universität Wien

unter der Leitung von:
Privatdoz. Dipl.-Ing. Dr.techn. Michael Eisterer

Wien, 1. Oktober 2020

Abstract

In the family of iron based superconductors Ba122 is a very fruitful compound for experimental and theoretical investigations. Superconductivity is induced in this system through electron doping (Co), hole doping (K) or isovalent doping (P). All these compounds have similar phase diagrams where, in the under-doped region, superconductivity and antiferromagnetism are in close proximity. Doping the parent compound suppresses the antiferromagnetic phase until, at a certain concentration, the Néel temperature vanishes. At this concentration a Quantum Critical Point is speculated to be hidden in the superconducting region. Superconductivity emerges in the antiferromagnetic phase and the critical temperature, T_c, increases with increasing dopant concentration until a maximum is reached where the sample is optimally-doped. Higher dopant concentration results in a suppression of T_c. This leads to a superconducting dome in the phase diagram with close proximity to the antiferromagnetic phase.

A very important parameter for applications is the critical current density, J_c. This parameter strongly depends on flux pinning resulting from inhomogeneities in the material. Previous studies observed a sharp peak in the doping dependence of J_c in the Co-, P- and K-doped system, while T_c varies much smoother around the maximum. This sharp peak in J_c is unexpected since a similar variation as for T_c is expected. A suitable experimental technique to tackle this mismatch is neutron irradiation which can be carried out at the research reactor of the Atominstitut. Therefore, the critical current density and the critical temperature of all three doping systems of Ba122 were measured prior to and after the neutron irradiation. J_c was obtained from the irreversible magnetization measured in a Superconducting Quantum Interference Device magnetometer and in a Vibration Sample Magnetometer. T_c was obtained by AC susceptibility measurements.

The high quality single crystals for these investigations were provided by the Material Science Department of the National Institute of Advanced Industrial Science and Technology (AIST) in Tsukuba, Japan. Crystals of all three doping systems of Ba122 were available with different doping concentrations covering the superconducting dome of each system.

After neutron irradiation, the peak in the doping dependence of J_c shifts to higher dopant concentrations, broadens and roughly follows the shape of the doping dependence of the respective T_c in all three doping systems. Moreover, a power law between J_c and T_c was observed in all irradiated crystals, which is explained by relations between superconducting parameters and T_c. The power law seems to be universal for Ba122, however, it is not clear at the moment if it also holds for other high temperature superconductors. The power law does not hold for the pristine crystals which indicates that the doping dependence of J_c results from the doping dependence of the pinning efficiency which was calculated for the pristine crystals using the power law correlation. It showed a larger pinning efficiency in the under-doped area which decreases with further doping for all three doping systems. The under-doped area is the area where superconducticity and antiferromagnetism are in close proximity.

Further understanding of the flux pinning in Ba122 can help to improve the critical current properties of this material for future applications. Moreover, the extension of the power law found in this thesis to other high temperature superconductors could lead to a better understanding of high temperature superconductivity.

Kurzfassung

Ba122 ist eine sehr vielversprechende Verbindung für experimentelle und theoretische Untersuchungen in der Familie der Eisensupraleiter. Supraleitung wird in diesem System durch das Dotieren von Elektronen (Co), Löchern (K) oder durch isovalente Dotierung hervorgerufen. Die Phasendiagramme all dieser Verbindungen haben das gemeinsame Auftreten von Antiferromagnetismus und Supraleitung im unterdotierten Bereich gemeinsam. Die Dotierung der nicht supraleitenden Startverbindung unterdrückt die antiferromagnetische Phase bis bei einer bestimmten Dotierungskonzentration die Néel Temperatur verschwindet. Bei dieser Dotierungskonzentration wird auch die Existenz eines quantenkritischen Punktes diskutiert. Supraleitung tritt in der antiferromagnetischen Phase auf und die kritische Temperatur T_c nimmt mit steigender Dotierungskonzentration zu, bis ein Maximum bei der sogenannten optimalen Dotierung erreicht wird. Weiteres Dotieren führt zu einer Abnahme von T_c und zur Bildung einer kuppelförmigen supraleitenden Phase welche sich in der Nähe der antiferromagnetischen Phase befindet.

Ein wichtiger Parameter für Anwendungen ist die kritische Stromdichte J_c die stark von der Flussverankerung an Inhomogenitäten im Material abhängt. Eine frühere Arbeit entdeckte eine Spitze in der Dotierungsabhängigkeit von J_c in Co, P und K dotiertem Ba122, wobei T_c deutlich weniger variierte. Die scharfe Spitze in J_c ist unerwartet, weil eine vergleichbare Dotierungsabhängikeit wie von T_c erwartet werden würde. Eine experimentelle Methode um diesen Unterschied zu untersuchen ist die Bestrahlung mit Neutronen, welche im Versuchsreaktor am Atominstitut durchgeführt werden kann. Dazu wurden die kritische Stromdichte und die kritische Temperatur der Proben vor und nach der Bestrahlung gemessen. J_c wurde aus der irreversiblen Magnetisierung berechnet welche mit Hilfe eines SQUID-Magnetometers und eines Vibrationsmagnetometers gemessen wurde. Die kritische Temperatur wurde durch Wechselfeld-

suszeptibilitätsmessungen bestimmt.

Die qualitativ sehr hochwertigen Einkristalle für diese Untersuchungen wurden vom Material Science Department of the National Institute of Advanced Industrial Science and Technology (AIST) in Tsukuba in Japan zur Verfügung gestellt. Einkristalle aller drei Dotierungen mit verschiedenen Dotierungskonzentrationen welche die kuppelförmige supraleitende Phase abdecken standen zur Verfügung.

Nach der Neutronenbestrahlung verschob sich die Spitze in der Dotierungsabhängigkeit von J_c in allen drei untersuchten Systemen zu einer höheren Dotierungskonzentration und verbreiterte sich. Die Dotierungsabhängigkeit von J_c nach der Bestrahlung war vergleichbarer mit der kuppelförmigen supraleitenden Phase die durch die Dotierungsabhängigkeit von T_c entsteht. Dieser ähnliche Verlauf führte zur Entdeckung eines Potenzgesetzes zwischen J_c und T_c in den bestrahlten Proben, welches durch Zusammenhänge zwischen supraleitenden Parametern und T_c erklärt wurde. Dieses Potenzgesetz scheint universell für Ba122 zu sein, es ist aber nicht klar ob es auch für andere Hochtemperatursupraleiter gilt. Das Potenzgesetz findet man nicht in den unbestrahlten Proben, was darauf hindeutet, dass die Dotierungsabhängigkeit von J_c durch die Dotierungsabhängigkeit der Flussverankerungseffizienz hervorgerufen wird. Die Dotierungsabhängigkeit der Flussverankerungseffizienz der unbestrahlten Kristalle wurde mit Hilfe des Potenzgesetzes berechnet und nimmt von ihrem höchsten Wert im unterdotierten Bereich mit weiterer Dotierung ab. Der unterdotierte Bereich ist jener Bereich, in dem Supraleitung und Antiferromagnetismus gemeinsam auftreten.

Ein besseres Verständnis der Flussverankerung in Ba122 könnte dabei helfen die kritischen Ströme dieses Materials für zukünftige Anwendungen zu verbessern. Außerdem könnte die Erweiterung des Potenzgesetzes auf andere Hochtemperatursupraleiter zu einem besseren Verständnis der Hochtemperatursupraleitung führen.

Acknowledgments

I would like to thank my supervisor Michael Eisterer for the opportunity to carry out this thesis. He had always time to discuss results and give advice for further steps. He encouraged me to follow my own ideas, which was motivating and challenging.

Next, I would like to thank my colleagues at AIST in Japan for providing the best samples and hosting me twice in Japan. Hiroshi Eisaki for the possibility to stay at AIST and all the motivating discussions we had. Shige for being patient with me when showing me how to grow single crystals and for the nice cooperation. Dongjoon and Hiraku also for very fruitful cooperation. Furthermore, I would like to thank all my Japanese colleagues for letting me experience nice and interesting Japanese food and drinks. For all of that: ありがとうございました！

A big thank you to all my colleagues in the low temperature physics group at the Atominstitut. Thank you to my former colleagues David, Thomas, Hannes, Murph and May. Also, thank you to my present colleagues Franz, David, Mattia and Raphael. To all of you, thank you for the great time during my thesis and for a lot of input for my scientific work.

I would like to thank Marina Putti and Tsuyoshi Tamegai for taking the time and effort to review my thesis.

Also, I would like to thank my friends and my family for their understanding and their help to clear my mind during the challenging times of this thesis.

Finally, I would like to thank my partner in life and colleague Sigrid for all the support and motivation she gave me throughout this thesis, especially during the time of writing the thesis. Thank you very much for that!

Nomenclature

The following list describes frequently used symbols in this work. If not stated otherwise, SI units are used throughout this thesis.

$\boldsymbol{\Delta T_{\mathrm{c}}}$	reduction of the critical temperature after neutron irradiation
$\boldsymbol{\eta}$	pinning efficiency
$\boldsymbol{\eta_{\mathrm{irr}}}$	constant pinning efficiency of the irradiated samples
$\boldsymbol{\eta_{\mathrm{pris}}}$	pinning efficiency of the pristine samples
$\boldsymbol{\kappa}$	Ginzburg-Landau parameter
$\boldsymbol{\lambda}$	magnetic penetration depth
$\boldsymbol{\lambda_{\mathrm{L}}}$	London penetration depth
$\boldsymbol{\Phi_0}$	flux quantum
$\boldsymbol{\Psi}$	superconducting wave function in the Ginzburg-Landau theory
$\boldsymbol{\Psi_\infty}$	equilibrium value of the superconducting wave function
$\boldsymbol{\rho_s}$	superfluid density
$\boldsymbol{\sigma_{\mathrm{dc}}}$	DC conductivity
$\boldsymbol{\xi}$	Ginzburg-Landau coherence length
$\boldsymbol{\xi_0}$	average extension of a Cooper pair from BCS theory

$\boldsymbol{a, b, c}$	dimensions of a single crystal along the crystallographic axis, respectively
$\boldsymbol{B}$	magnetic induction
$\boldsymbol{B_c}$	thermodynamic critical field
$\boldsymbol{B_{c1}}$	lower critical field of a type-II superconductor
$\boldsymbol{B_{c2}}$	upper critical field of a type-II superconductor
$\boldsymbol{E_{\mathrm{cond}}}$	condensation energy density
$\boldsymbol{E_{\mathrm{core}}}$	core energy per unit length of a flux line
$\boldsymbol{H^*}$	field at which the sample is fully penetrated according to Bean's critical state model
$\boldsymbol{H_{\mathrm{app}}}$	applied magnetic field
$\boldsymbol{H_{\mathrm{self}}}$	magnetic self field
$\boldsymbol{J_{\mathrm{c,irr}}}$	critical current density of the irradiated crystals
$\boldsymbol{J_{\mathrm{c,pris}}}$	critical current density of the pristine crystals
$\boldsymbol{J_{\mathrm{c}}}$	critical current density
$\boldsymbol{J_{\mathrm{d}}}$	depairing current density
$\boldsymbol{k}$	coeficient of the power low relation between critical current density and critical temperature
$\boldsymbol{l^*}$	electron mean free path
$\boldsymbol{m}$	mass of the particles in the Ginzburg-Landau theory described by Ψ
$\boldsymbol{m^*}$	effective mass of a charge carrier
$\boldsymbol{m_{\mathrm{irr}}}$	irreversible magnetic moment
$\boldsymbol{n_s}$	density of superconducting electrons
$\boldsymbol{q}$	charge of the particles in the Ginzburg-Landau theory described by Ψ

$\boldsymbol{T}_{\mathbf{c,10\%}}$	temperature where 10% of the magnetic moment in the superconducting phase is reached
$\boldsymbol{T}_{\mathbf{c,90\%}}$	temperature where 90% of the magnetic moment in the superconducting phase is reached
$\boldsymbol{T}_{\mathbf{c,tan}}$	tangent criterion for the critical temperature
$\boldsymbol{T}_{\mathbf{c0}}$	critical temperature of a pristine crystal
$\boldsymbol{T}_{\mathbf{c}}$	temperature of the superconducting state, $T_{\mathrm{c},10\%}$ used in this thesis
$\boldsymbol{T}_{\mathbf{N}}$	Néel temperature of the antiferromagnetic orderded phase
$\boldsymbol{V}$	volume of a single crystal
$\boldsymbol{x}$	dopant concentration
$\boldsymbol{x}_{\boldsymbol{J_c,max}}$	dopant concentration where the critical current density is maximal in the pristine crystals

List of Tables

List of Figures

Contents

Chapter 1

Introduction and Theory

The experiments in this thesis were performed with iron based superconductors. Therefore, this class of high temperature superconductors will be introduced in this chapter with a short historical background and recent progress. Additionally, fundamental theoretical descriptions of superconductivity and high temperature superconductivity will be motivated and summarized. Last, this introduction will be concluded with the motivation and background for this thesis.

1.1 Iron Based Superconductors

High temperature superconductors are very diverse materials. There are two big classes and several other materials. These two classes are: (1) the cuprates where high temperature superconductivity was first discovered [1]; and (2) the iron based superconductors which include the iron pnictides (with the pnictide element As or P) and the iron chalcogenides (with chalcogenide element S, Se, or Te). The latter where first discovered in 2008 [2] which shortly lead to the discovery of several members of this new class of high temperature superconductors. These numerous iron based superconductors are categorized into several families. The first discovered material was LaFeAsO and belongs to the so-called 1111 family [2]. After its discovery several new families of iron based superconductors were discovered. The structure of 1111 is quite complicated, therefore, researchers were searching for iron based superconductors with a simpler structure which are more suitable for applications. LiFeAs was the first member of the 111 family [3]. An even simpler iron based superconductor was discovered with FeSe, a member of the 11 family [4]. This material is also very interesting from a theoretical point of view because its very simple structure enables research on the pairing mechanism or other fundamental properties of high temperature superconductivity. But, the materials most investigated so far are members of the 122 family. The first discovered member of this family was potassium doped $BaFe_2As_2$ [5]. Single crystals of this family are investigated in this theses and a more detailed description of these materials will be given in Sec. 2.1. The most recent discovered family of iron based superconductors is the so-called 1144 family [6, 7]. Some of these materials are quite interesting for application because it is not necessary to dope them to introduce superconductivity which eliminates inhomogeneity in the superconducting properties. Moreover, in a member of this family, namely $EuRbFe_4As_4$, superconductivity and antiferromagnetism coexists in a certain temperature range which gives the opportunity to investigate the interplay between these antagonist phenomena.

All iron based superconductors have a layered structure with Iron Arsenide layers (in the 11 family the respective layers are Iron Selenium layers) in common. These layers can be compared to the Copper Oxide layers in cuprates and are essential for superconductivity in these materials. The layered structure of high temperature superconductors is often a problem for applications because it results in a bigger anisotropy of superconducting parameters as in conventional superconductors. This anisotropy is smaller in iron based superconductors than in cuprates [8]. For application, grain boundaries pose a limiting factor for the current transport. This problem is overcome in cuprates by the complicated structure of coated conductors which limits the grain boundary angle and keeps it under its critical angle. This is the angle above which the current passing through a grain boundary decreases significantly. This value is larger in iron based materials compared to cuprates making them more tolerant to grain misalignment [9]. Another advantage of iron based superconductors is their metallic nature compared to the brittle ceramic cuprates which makes the processing easier.

The superconducting state is restricted by a critical temperature of up to 55 K in 1111 materials under high pressure [10]. Under ambient pressure T_c can get up to 38 K in 122 materials [5]. Iron based superconductors are clearly unconvential superconductors but they differ substantially from other high temperature superconductors like the cuprates. The pairing mechanism is still heavily debated. It seems that its symmetry is not d-wave but a certain form of s-wave (s_{++} and s_{+-} are discussed). Contrarily, a doping dependence ot the pairing symmetry is discussed where there would exist d-wave pairing for highly doped systems. Regardless the uncertainty about the pairing symmetry, the proximity of an antiferromagnetic phase in several iron based superconductors seem to play an important role. For example, spin density wave fluctuations are discussed among possible pairing mechanisms. The antiferromagnetism and superconductivity in the 122 family are not just in close proximity, but there is a range where they overlap [11]. This rises the question how these two phases occur together. At the moment, there is evidence that they are in a microscopic coexistence [12].

Concluding this summary of iron based superconductors, they are the newest class of high temperature superconductors and they serve as playground likewise for theoretical and experimental research. Additionally, there are promising results for future applications, maybe in a niche, for iron based superconductors [8, 13, 14].

1.2 Ginzburg-Landau-Theory

The London theory for superconductors [15] is able to explain the penetration of magnetic fields into superconductors in principle, but sometimes fails to reproduce the experimental values. Additionally, the theory assumes a constant density of superconducting electrons, n_s, which makes it impossible to describe a mixed state of superconducting and normal conducting areas, like the mixed state in type-II superconductors. To solve this problem, Ginzburg and Landau used Landau's theory for second order phase transitions [16] and applied it on superconductivity [17]. The theory for phase transitions of second order requires an order parameter which is zero above the transition and finite below it. Ginzburg and Landau identified this order parameter as a complex wave function of the superconducting state, Ψ, whose absolute square represents the density of superconducting electrons n_s. This order parameter is now used to expand the free energy density near the transition temperature. Therefore, strictly speaking the Ginzburg-Landau-Theory is just valid close to the phase boundary: for example near T_c. Nevertheless it seems also to fit experimental results at lower temperatures. This theory was formulated before the BCS-theory, so Cooper-pairs or their condensation where not known at that time. After the formulation of the microscopic BCS-theory the macroscopic Ginzburg-Landau-theory was not much-noticed until Gor'kov was able to show that the latter was a limiting case of the microscopic theory. That connected the microscopic with the macroscopic theory. Already before that, Abrikosov solved the Ginzburg-Landau-equations for the mixed state and predicted the existence of flux lines [18, 19].

The Ginzburg-Landau-Theory with the above outlined concepts lead to the two Ginzburg-Landau equations describing the evolution of the order parameter Ψ:

$$\frac{1}{2m}\left(-\mathrm{i}\hbar\vec{\nabla}-q\mu_0\vec{A}\right)^2\Psi+\alpha\Psi+\beta|\Psi|^2\Psi=0\,, \tag{1.2.1}$$

$$\vec{j}_{\mathrm{s}}=\frac{q\hbar}{2m\mathrm{i}}\left(\Psi^*\vec{\nabla}\Psi-\Psi\vec{\nabla}\Psi^*\right)-\frac{q^2\mu_0}{m}|\Psi|^2\vec{A}\,. \tag{1.2.2}$$

Where α and β are the expansion coefficients of the free energy for the second and fourth order of the order parameter Psi, respectively. The complex wave function Ψ describes particles with the mass m and the charge q. Considering Cooper pairs: $m = 2m_e$ and $|q| = 2e$. The above system of differential equations must be supplemented by boundary conditions for a complete description. Often, this condition is the restriction of the supercurrent to the volume of the superconductor. Thus, the supercurrent does not pass thorough the surface of the superconductor.

A further investigation of Eq. 1.2.1 and Eq. 1.2.2 shows that they contain two characteristic lengths. The derivation of these can be found, for example, in [20] and should be just summarized here. For the derivation, the order parameter in the Ginzburg-Landau-equations is normalized to its equilibrium value, Ψ_∞, sufficiently far away from any interface. The second London equation can be obtained from Eq. 1.2.2 by using the relation $n_s = |\Psi_\infty|^2$ which corresponds to the assumption of a constant density of the superconducting charge carriers made in the London theory. This equation contains the London penetration depth

$$\lambda_{\mathrm{L}}=\sqrt{\frac{m}{\mu_0 q^2 n_s}} \tag{1.2.3}$$

which is the first characteristic length in the Ginzburg-Landau-Theory and gives the length scale on which the magnetic field (or the supercurrents) can change. This is the same penetration depth as obtained from London theory. The second length can be derived from Eq. 1.2.1. There the quantity $-\hbar^2/(2m\alpha)$ has the dimension of a squared length which can be interpreted as the

Ginzburg-Landau coherence length

$$\xi = \sqrt{\frac{-\hbar^2}{2m\alpha}} \; . \tag{1.2.4}$$

It is the length scale within which the order parameter (Cooper pair density) can change.

The above described situation is true for clean materials but further adaptions have to be made to describe dirty superconductors which is a very important application field of the Ginzburg-Landau-theory. The parameter used to characterize a dirty superconductor is the electron mean free path, l^*, which is the average distance a charge carrier can travel between two collisions. Thus, the effective London penetration depth, λ, can be written as:

$$\lambda^2 = \lambda_\mathrm{L}^2 \, \frac{\xi_0}{l^*} \; . \tag{1.2.5}$$

ξ_0 is the coherence length of the BCS theory corresponding to the average extension of a Cooper pair. Moreover, the Ginzburg-Landau coherence length is modified for $l^* << \xi_0$ in the following way:

$$\xi = \sqrt{\xi_0 \; l^*} \; . \tag{1.2.6}$$

The magnetic penetration depth, λ, and the Ginzburg-Landau coherence length, ξ can be combined to the temperature independent so-called Ginzburg-Landau parameter $\kappa = \lambda/\xi$. This parameter is used to distinguish between type-I and type-II superconductors. Its value is smaller than $1/\sqrt{2}$ for type-I superconductors and bigger for type-II superconductors.

It is now possible to relate the two length scales to the critical fields using the Ginzburg-Landau-Theory. The thermodynamic critical field, B_c, is associated to the difference between the free enthalpy of the superconducting and the normal conducting state. Using ξ and λ it can be written as

$$B_\mathrm{c} = \frac{\Phi_0}{2\sqrt{2}\pi\lambda\xi} \; , \tag{1.2.7}$$

with the flux quantum Φ_0. Abrikosov showed that in the limit $\kappa >> 1/\sqrt{2}$ (which is fulfilled for all high temperature superconductors) the lower critical field B_c1 can be related to the magnetic penetration depth:

$$B_\mathrm{c1} = \frac{\Phi_0}{4\pi\lambda^2} \left(\ln\kappa + 0.08\right) \; . \tag{1.2.8}$$

The lower critical field is the field where magnetic flux first penetrates into a type-II superconductor. The value 0.08 in Eq. 1.2.8 includes the interaction between the vortices in a triangular lattice [21, 19, 20]. Furthermore, a simple expression for the upper critical field B_{c2} can be found from the solution of the Ginzburg-Landau equations:

$$B_{c2} = \frac{\Phi_0}{2\pi\xi^2} \ . \tag{1.2.9}$$

The upper critical field is a boundary for the superconducting state. At higher fields superconductivity is not stable any more.

1.3 Depairing Current Density

This section addresses the derivation of the maximum possible current density according to the Ginzburg-Landau-Theory. The starting point are the two Ginzburg-Landau equations Eq. 1.2.1 and Eq. 1.2.2 and the assumption of a thin wire elongated along the x direction. A thin wire simplifies the calculation because if its diameter is smaller than both λ and ξ the Cooper pair density can be assumed as constant. The ansatz for the superconducting wave function is $\Psi = \Psi_0 e^{ikx}$. Inserting this in Eq. 1.2.2 results in the superconducting current density in x-direction:

$$j_{s,x} = q\Psi_0^2 \frac{\hbar k - \mu_0 A_x q}{m} = q\Psi_0^2 v_x \ . \tag{1.3.1}$$

Here the expression of the Cooper pair velocity v_x is used. The next step is to insert the ansatz in Eq. 1.2.1. This leads to

$$\frac{1}{2} m v_x^2 + \alpha + \Psi_0^2 \beta = 0 \ , \tag{1.3.2}$$

by also using the expression of the Cooper pair velocity. This equation can be used to express Ψ_0:

$$\Psi_0^2 = n_s \left(1 - \frac{m v_x^2}{2|\alpha|}\right) \ . \tag{1.3.3}$$

The following two statements are used to obtain this expression. First, the coefficient α from the Taylor series expansion of the free energy in the Ginzburg-Landau-Theory is always negative in the superconducting state. Second, the two coefficients α and β are connected by the density of the Cooper pairs in the following way: $-\alpha/\beta = n_s$. Eq. 1.3.3 shows that the density of Cooper pairs decreases if their velocity increases. The superconducting current density as a function of the Cooper pair velocity is obtained by inserting Eq. 1.3.3 into Eq. 1.3.1. There are now two contributions working against each other in the superconducting current density. On the one hand an increasing Cooper pair velocity increases the superconducting current density, but on the other hand this increasing velocity decreases the density of the Cooper pairs. The maximum velocity can be calculated with $\frac{dj_{s,x}}{dv_x} = 0$ and leads to the maximum superconducting current density which will be called depairing current density, J_d, from here on:

$$J_\mathrm{d} = \frac{2}{3} q \sqrt{\frac{2|\alpha|}{3m}} n_s \, . \tag{1.3.4}$$

This equation can be rewritten in the well-known form by using the expression for the magnetic penetration depth [Eq. 1.2.3], the expression for the coefficient $\alpha = -\frac{1}{\mu_0}\frac{B_\mathrm{c}^2}{n_s}$ (from the difference between the free energy in the superconducting and normal conducting phase), and the definition of B_c [Eq. 1.2.7]:

$$J_\mathrm{d} = \frac{\Phi_0}{3\sqrt{3}\pi\mu_0\lambda^2\xi} \tag{1.3.5}$$

Since the above expression for J_d is derived from Ginzburg-Landau theory it is just valid near the phase boundary. But, several experiments showed that the Ginzburg-Landau theory is also valid at lower temperatures. This is achieved by introducing the correct temperature dependence of the superconducting parameters.

It is also possible to derive a similar expression for the depairing current density using the microscopic BCS theory [20, 22]. There, the Cooper pair velocity is compared to the energy gap. The so-obtained BCS expression for J_d depends on the same parameters but is bigger by the factor $(3/2)^{3/2} \approx 1.84$ than the Ginzburg-Landau expression.

1.4 Critical Current Density

The depairing current density was calculated in the last section following the Ginzburg-Landau theory and by a restriction to small superconductors compared to ξ and λ, thus there are further modifications necessary for bigger superconductors like the ones used in this thesis. These samples will be entered by flux lines in a field between B_{c1} and B_{c2} which is reached already by the self-field of the currents in the samples. These flux lines interact via the Lorentz force with the currents in the superconductor and move perpendicular to the current flow direction unless an additional force acting opposite to the Lorentz force prevents such a movement. Without this force, the movement of the flux lines induces an electric field and, furthermore, dissipates energy due to the resistive behavior. The force counteracting the Lorentz force is called pinning force since it pins the flux lines to fixed positions in the material. This pinning results from a dependence of the free energy of the system on the spatial position of the flux lines caused by local inhomogeneities in the material. Thus, some locations are energetically favorable for the flux lines and energy is needed to remove them from these positions. These local inhomogeneities can be grain boundaries, voids, impurities, normal conducting inclusions etc. resulting in variations of ξ or λ and therefore of B_c. A simple example for a pinning center is a normal conducting rod with the diameter ξ. If a flux line is positioned exactly on this rod the whole condensation energy for the normal conducting flux line core (with the diameter ξ) is saved for this configuration. Therefore, this position is energetically favorable for the flux line.

The pinning of flux lines rather than the depairing limits the current transport in superconductors with flux lines present. The resulting limit is the critical current density, J_c. Thus, the flux lines are pinned until the critical current is reached and flux lines start to move for higher currents which leads to energy dissipation. The contributions of flux line pinning and depairing to the critical current density can be separated by writing J_c as a product of the pinning efficiency, η, and the depairing current density. Thus, the critical current density can be written as

$$J_c = \eta \cdot J_d \; . \tag{1.4.1}$$

The pinning efficiency is a material parameter and sums up the effects of all microscopic pinning centers present in the sample. The fundamental superconducting parameters, penetration depth and coherence length, are represented by the depairing current density.

The parameter η is limited by two cases. The first case is a clean superconductor without pinning centers and flux lines present which can not sustain a loss free current density because the movement of flux lines dissipates energy. Thus, the pinning efficiency in this case is zero.

The second case is a superconductor where all flux lines are pinned to pinning centers. This can be estimated using the core energy per unit length of a flux line [23]. Therefore, the condensation energy density, $E_{\mathrm{cond}} = \frac{B_{\mathrm{c}}}{2\mu_0}$, is multiplied by the area of the normal conducting flux line core, $\xi^2\pi$. This results in the core energy per unit length, $E_{\mathrm{core}} = \frac{\Phi_0^2}{16\pi\mu_0\lambda}$. The pinning force per unit length can be estimated as $f_p \approx E_{\mathrm{core}}/\xi$ because the superconducting order parameter changes on the length scale of ξ. This force should compensate the Lorentz force per unit length, $f_L = \int\int J_{\mathrm{c}} B \, dS$, resulting from the critical current density in the superconductor. The integral over B gives the flux quantum, therefore the Lorenz force is: $f_L = J_{\mathrm{c}}\Phi_0$. If these two forces are equal the critical current density is maximal. The maximum critical current density can be expressed with J_{d} from Eq. 1.3.5 as

$$J_{\mathrm{c},max} = \frac{3\sqrt{3}}{16} J_{\mathrm{d}} \, . \tag{1.4.2}$$

The prefactor of J_{d} is the maximum achievable pinning efficiency, η_{max}. Thus, approximately 32% of the depairing current density is the universal maximum reachable critical current density [23, 24]. The universality is given because all material parameters are governed by J_{d}.

1.5 Uemura relation

The investigation of correlations in high temperature superconductors is of great interest since the discovery of superconductivity in cuprates. These correlations between physical quantities are used as experimental hints on the origin of superconductivity in these materials. One of the most known scaling relations is the so-called Uemura relation (also Uemura scaling or Uemura-plot). It was discovered as a universal correlation for cuprate superconductors [25]. The reported correlation is a direct proportionality of the transition temperature, T_{c}, and the superfluid density, ρ_s (superconducting carrier density, n_s, divided by the effective mass, m^*). Furthermore, the superconducting carrier density is proportional to $1/\lambda^2$ leading to the relation used in this thesis:

$$T_{\mathrm{c}} \propto \frac{1}{\lambda^2} \, . \tag{1.5.1}$$

At first this correlation was only described as valid for under-doped cuprates but later it was shown that it is also valid for over-doped cuprates [26]. Moreover, there is evidence that the iron based superconductors also fulfill the Uemura relation [27, 28, 29].

A scaling which can be thought of as an extension of the Uemura relation is the so-called Homes scaling [30]. This scaling is a direct proportionality between ρ_s and T_c multiplied with the DC conductivity close to the transition, σ_{dc}. Using the magnetic penetration depth this can be written as

$$\sigma_\mathrm{dc} T_\mathrm{c} \propto \frac{1}{\lambda^2} \; . \tag{1.5.2}$$

The Homes scaling did not fail for the over-doped cuprates like the Uemura relation in early works. As mentioned above, it was shown that for very clean materials also the over-doped cuprates follow the Uemura relation [26]. Therefore, the purity of the materials seems to play an important role in these scaling relations. This can be accounted for (as it is done in the Holmes scaling) by multiplying T_c with the DC conductivity. σ_dc is proportional to $1/m^*$ which cancels the dependence of the superfluid density on the effective mass. This seems to recover the scaling for over-doped cuprates [30].

Generally speaking, the relation between superfluid density and transition temperature can be used to make predictions about the condensation mechanism. BCS theory describes the condensation as taking place simultaneously with the pair formation. Thus, T_c is related to the energy gap and depends only weakly and indirectly on the superfluid density. This theoretical framework does not describe the Uemura relation because it would assume that T_c and ρ_s are independent of each other. Additionally, the Uemura relation shows that doping is not a primary factor for T_c. It effects T_c just indirect via the charge carrier density. The direct proportionality between T_c and ρ_s rather is evidence for a local superconducting phase with a Bose-Einstein-Condensation taking place at T_c. The pseudogap temperature in cuprates could be interpreted as the temperature where this pair formation takes place [31]. The normal state between the pseudogap temperature and T_c would be described by the mixture of electrons and pre-formed pairs. All this interpretation attempts are still debated and a lot of experimental work tries to solve the many still open questions. Additionally, it is not clear how to interpret this in iron based superconductors where no pseudogap temperature is reported so far.

1.6 Motivation and Background

The starting point and motivation for this thesis were extensive measurements on the doping dependence of the critical current density and transition temperature in three doping systems of the 122 family iron based superconductor. T_c as a function of the dopant concentration, x, shows a dome like shape in these compounds. Contrarily, $J_\mathrm{c}(x)$ shows a sharp peak which was measured in the potassium, phosphorous, and cobalt doped compound [32, 33, 34, 35]. The discrepancy between $T_\mathrm{c}(x)$ and $J_\mathrm{c}(x)$ is unexpected because it would be expected at first glance that they vary in a similar way. There are three explanation attempts: (1) A variation of superconducting parameter (such as condensation energy, coherence length, or magnetic penetration depth) as a function of doping similar to J_c; (2) A doping dependent defect structure (pinning); (3) An exotic mechanism like a quantum critical point. At the moment, it is not clear if there is a universal explanation for the shape of $J_\mathrm{c}(x)$ for all doping systems or if the reasons are different in each system.

This thesis aims to investigate samples of potassium, phosphorous, and cobalt doped Ba122 with doping concentrations spanning the whole superconducting dome. The attempt to distinguish between the proposed explanations is neutron irradiation. This technique is known to introduce isotropic defects up to a size of a few nanometer, which have proven to be more efficient for flux pinning than the crystallographic defects in the pristine crystals. Each doping set of samples will be irradiated with the same fluence resulting in a similar pinning landscape in all samples after irradiation. Therefore, the pinning in samples with different doping concentration should be equal after irradiation. Now the doping dependence of J_c should reflect the doping dependence of the superconducting parameters or a fingerprint of an exotic pinning mechanism. Furthermore, it is possible to compare the different doping systems after irradiation and discuss possible differences or similarities. The understanding of the dopant concentration dependence of the critical current density, and its change after irradiation, can help to draw conclusions on the mechanism underlying the unexpected behavior of $J_\mathrm{c}(x)$. This understanding can help to improve the loss-free currents of iron based superconductors for future applications by the modification of microscopic (pinning) landscape or optimizing the doping level and system.

Chapter 2

Samples and Experimental Methods

The samples investigated in this theses are iron based superconductors of the 122 family. A more detailed description of the samples is given in this chapter. All samples were characterized prior to and after neutron irradiation. The properties of interest are the critical temperature, T_c, and the critical current density, J_c. The measurement techniques and evaluation methods for these properties are also described in this chapter.

2.1 Samples

The iron based superconductors investigated in this theses are single crystals of the $\mathrm{BaFe_2As_2}$ (Ba122) family which have the crystal structure shown in Fig. 2.1.1(a). Superconductivity is introduced in this compound either via external pressure or via doping [11]. This work will focus on the latter case. There are three different possibilities to dope Ba122 which differ in the doping site and the valence of the dopant. Electron doping is realized by replacing Fe with, for example, Co resulting in $\mathrm{Ba(Fe_{1-x}Co_x)_2As_2}$ where x is the dopant concentration. These materials exhibit a T_c of up to 24 K at optimal doping. It is also possible to introduce superconductivity by an isovalent replacement of As with P resulting in $\mathrm{BaFe_2(As_{1-x}P_x)_2}$ with a T_c of up to 29 K.

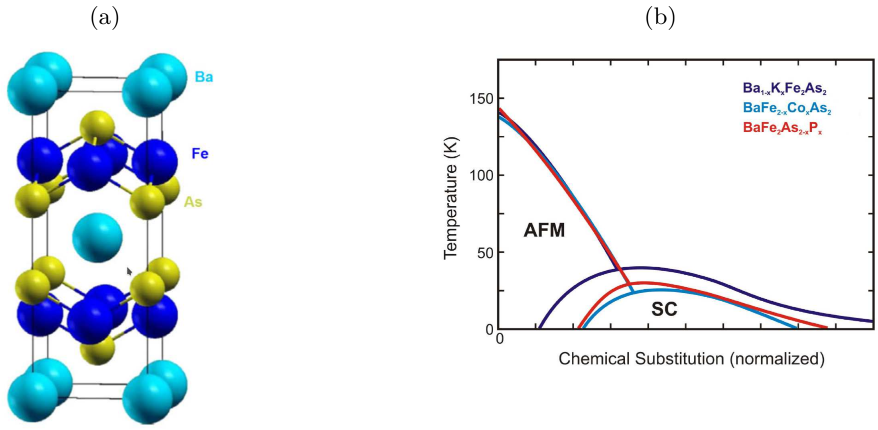

Fig. 2.1.1: (a) Crystal structure of the parent compound of Ba122 [11]. (b) Phase diagrams of the three doping systems (potassium, phosphorous, cobalt) of Ba122 used in this theses [36]. The dopant concentration is normalized to show all doping systems in one diagram. The superconducting and the antiferromagnetic phase are denoted as SC and AFM, respectively.

Finally, hole doping can be realized by replacing Ba with K resulting in $\mathrm{Ba}_{1-x}\mathrm{K}_x\mathrm{Fe}_2\mathrm{As}_2$. This doping system reaches a T_c of up to 40 K which is the highest T_c of the 122 family.

The phase diagrams of all three doping systems of Ba122 described above are very similar. They exhibit an antiferromagnetic phase which is suppressed by doping and a superconducting phase emerging in a doping range where it coexists with antiferromagnetism. T_c increases, peaks, and decreases again upon further doping forming a superconducting dome. Especially, the doping range with the coexistence of antiferromagnetism and superconductivity is of great interest, because it is not clear at present how these two phases occur together, but there is evidence that they are in a microscopic coexistence [12]. The phase diagrams of K, Co and P-doped Ba122 are shown superimposed in Fig. 2.1.1(b) to show the similarities. Additional, the antiferromagnetic transition is accompanied by a structural transition from a tetragonal crystal structure, at high temperatures, to a orthorombic crystal structure at low temperatures. It has to be noted that these transitions do not happen at exactly the same temperatures but at temperatures close together depending on the doping system.

The potassium (BaK122), phosphorous (BaP122), and cobalt (BaCo122) doped single crystals were grown at the National Institute of Advanced Industrial Science (AIST) in Tsukuba, Japan by the flux method following References [37][38][39] using KAs, $\mathrm{Ba}_2\mathrm{As}_3$/$\mathrm{Ba}_2\mathrm{P}_3$, and FeAs as self-flux, respectively. The dopant concentration of the single crystals is adjusted by the

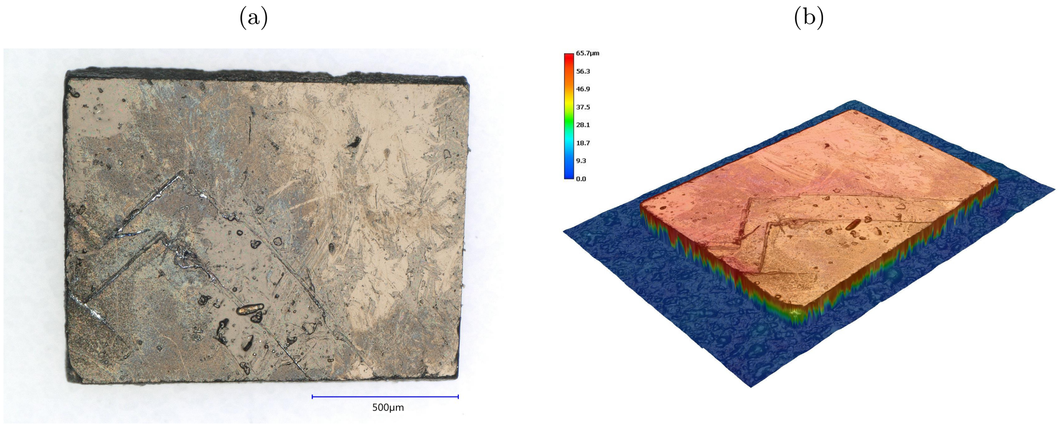

Fig. 2.1.2: (a) Topview of a typical single crystal. (b) 3D image of the crystal shown in (a) recorded with a digital microscope.

ratio of the used precursors. This ratio is the nominal doping concentration which is not necessarily the same as the actual doping concentration of the crystals after the heat treatment. The actual doping concentration is measured after the crystal growth by, for example, energy dispersive X-Ray spectroscopy (EDX) in a scanning electron microscope (SEM) or inductively coupled plasma (ICP) analysis. Summarizing, the nominal and the actual doping concentration in BaK122 is similar [37] and quite different in BaCo122 [38] and BaP122. However, this relation is known which makes it possible to grow crystals with a specific actual doping concentration. Whenever the term doping level is used in this thesis it refers to the actual doping because it is the doping concentration in the single crystals, which is more important for further measurements and interpretations. The used samples with names, doping levels and dimensions are listed in Tab. 2.1, 2.2, and 2.3 for BaK122, BaP122 and BaCo122, respectively. A typical single crystal is shown in Fig. 2.1.2. Each of the three sample sets include under-, optimally-, and over-doped crystals spanning the whole superconducting dome.

2.2 Magnetization Measurements

The critical current density and critical temperature were measured magnetically in this thesis. The measurements were carried out in a Vibrating Sample Magnetometer (VSM) and a Superconducting Quantum Interference Device (SQUID). This section will describe the devices and

sample name	doping level	a (mm)	b (mm)	c (μm)
Ba122K023	0.23	1.0	0.75	71
Ba122K025	0.265	0.8	0.4	40
Ba122K030	0.30	1.35	0.95	78
Ba122K033	0.33	1.0	0.65	50
Ba122K036	0.36	1.15	0.7	68
Ba122K040	0.40	1.35	1.1	97
Ba122K050	0.50	1.2	0.55	87

Tab. 2.1: Table of K-doped Ba122 samples with doping levels and dimensions

sample name	doping level	a (mm)	b (mm)	c (μm)
Ba122P024	0.24	0.95	0.45	126
Ba122Pnom4.2%	0.28	1.8	1.4	67
Ba122Pnom5%sud	0.29	0.8	0.45	41
Ba122P030Masa	0.30	1.05	0.75	23
Ba122P030	0.31	1.2	0.85	50
Ba122P033	0.33	1.5	0.65	42
Ba122Pnom5%sod	0.35	1.0	0.55	21
Ba122P038-2	0.38	1.1	0.9	88

Tab. 2.2: Table of P-doped Ba122 samples with doping levels and dimensions

sample name	doping level	a (mm)	b (mm)	c (μm)
Ba122Co005	0.05	1.46	1.33	99
Ba122Co0057	0.057	1.39	1.28	53
Ba122Co006	0.06	1.46	1.41	61
Ba122Co007	0.07	1.57	1.38	50
Ba122Co008	0.08	0.97	0.83	106
Ba122Co0095	0.095	1.66	0.97	58

Tab. 2.3: Table of Co-doped Ba122 samples with doping levels and dimensions

the evaluation of the parameters of interest. The critical current density was measured mainly with a VSM; therefore, the description of the device is included in Sec. 2.2.1. The description of the SQUID magnetometer is included in Sec. 2.2.2 because the measurements of the transition temperature were performed in this device.

2.2.1 Critical Current Density

A widely used method for the determination of the critical current density, J_c, is the measurement of the magnetic moment of a sample as a function of temperature and applied magnetic field. This magnetic moment can be used, with additional constraints, to calculate the average critical current density in the sample. The constraints regard the geometry of the critical current flow and are given by Bean's critical state model [40]. This model assumes that the only present current density in the sample is the critical current density. Furthermore, the critical current density is assumed to be constant and field independent in the whole sample. The magnetization process of an infinitely long sample with radius R is shown in Fig. 2.2.1. The response of the sample to an increasing applied field is shown in Fig. 2.2.1(a). It starts with a small applied magnetic field resulting in a flux density gradient inside the sample [see first field step in Fig. 2.2.1(a)]. This gradient represents the critical current density in this area screening the applied magnetic field which decreases linearly from its initial value at the sample surface to zero at a certain position inside the sample. Increasing the applied field increases this area inside the sample where the screening currents flow. At a certain field this flux front reaches the center of the sample and the critical current flows in the whole sample [see second field step in Fig. 2.2.1(a)]. This field is called penetration field, H^*. A further increase of the applied field leads to a parallel shift of the profile established in the sample [see further field steps in Fig. 2.2.1(a)]. The response of the sample to a decreasing field after the prior described increasing field steps is shown in Fig. 2.2.1(b). The starting point of the decreasing field is the last profile shown in Fig. 2.2.1(a). A decreasing applied field results in a flux density gradient in the opposite direction as for an increasing field. This results in the situation shown in the first field step in Fig. 2.2.1(b) where the field starts to decrease close to the sample surface but stays the same in the center of the sample. Decreasing the applied field to zero does not result in zero field inside the sample but

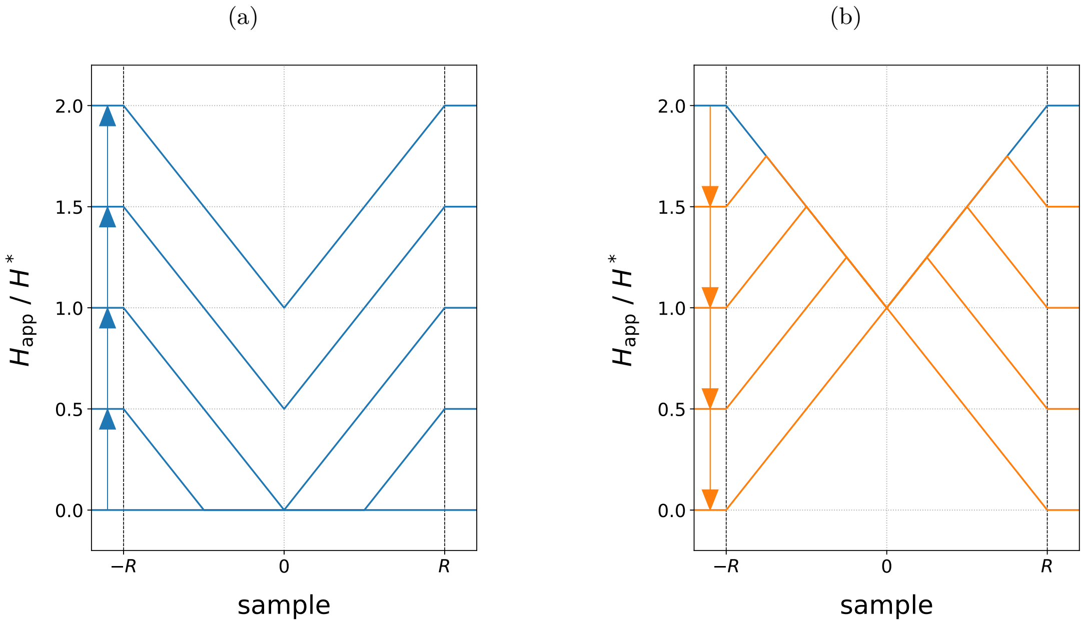

(a) (b)

Fig. 2.2.1: Bean's critical state model for an infinitely long sample with radius R: (a) A magnetic field is applied to the sample starting from zero. The arrows show the field steps in which the external field is increased. According to Bean's critical state model, the only possible current in the sample is the critical current which is represented by the constant slope of the field inside the sample. At a field of H^* the sample is fully penetrated by the magnetic field and a further increase of the applied field leads to a parallel shift of the field profile. (b) The field decrease starts with the field profile established at $2\,H^*$ in (a) shown in blue. The decrease of the field takes place with the same field steps as the field increase which is indicated by the arrows. A small field decrease changes the field at the surface of the superconductor but the field in the center stays unchanged [see first field decrease step]. Returning the applied field back to zero results in a remanent magnetization inside the sample.

rather to a remanent magnetization of the superconductor. The maximum field still present in the sample is the penetration field, H^*. Furthermore, Fig. 2.2.1 shows that an applied field of at least $2\,H^*$ is necessary to reverse the field profile in a superconductor.

The critical current density of interest in this thesis is J_c in the ab-plane. Thus, the magnetic field was applied parallel to the crystallographic c-axis and only the vector component of the magnetic moment parallel to the applied field was measured. Considering the current flow in the crystallographic ab-plane of a cuboid sample and the definition of the magnetic moment, $\vec{m} = \frac{1}{2}\int \vec{r} \times \vec{J}\, d^3r$, resulting from a current density $\vec{J}$ leads to the following equation for the critical current density:

$$J_c = \frac{4\,|m_{\mathrm{irr}}|}{Vb(1-b/3a)}\ . \tag{2.2.1}$$

The magnetic moment which needs to be assessed by the measurement is the irreversible magnetic moment m_{irr} resulting from the flux pinning in the sample. This is done by measuring a hysteresis loop. It is important to note that Eq. 2.2.1 is only valid for a sample fully penetrated by the magnetic field, e.g. the current flows just in one direction inside the sample parallel to the nearest surface. Therefore, prior to a hysteresis loop the sample was magnetized with a negative field bigger than $2\,H^*$. Afterwards, the magnetic moment was measured from zero to the maximum field (increasing field branch) and back to zero again (decreasing field branch). The difference between these two branches is $2\,m_{\mathrm{irr}}$ as a function of the applied field H_{app}. A Vibrating Sample Magnetometer (VSM), which will be described in the following, was used to record these hysteresis loops at different temperatures.

The underlying physical principle of a VSM is Faraday's law of induction. The magnetic moment of the sample induces a voltage in the pick-up coils of the VSM due to its vibration. This voltage is measured with a lock-in amplifier locked to the frequency of the vibration. The measured voltage is directly proportional to the magnetic moment of the sample and the proportionality constant is determined with a calibration measurement of a sample with known magnetic properties.

The VSM used in this thesis is equipped with a variable temperature insert (VTI) where temperatures between 4.2 K and 350 K can be reached. The applied field ranges from -5 T to 5 T. This can be a problem for the irradiated single crystals because of the strong increase of the critical current density after the neutron irradiation [41]. There it can happen that it is no longer possible to reach $2\,H^*$ and reverse the field with the available 5 T and thus not fulfill the requirement to use Eq. 2.2.1 for the evaluation of J_{c}. There are two ways, used in this thesis, to overcome this problem. First, it is possible to change the measurement method to a so-called field-cooled measurement where the sample is cooled through its T_{c} in an applied magnetic field. If this applied field is higher than H^* the sample is fully penetrated for the measurement with a slightly changed procedure. Thus, only H^* and not $2\,H^*$ are needed which lies in the field range of the VSM. For a field-cooled measurement, the magnetic moment is measured only to the maximum H_{app} and not back to zero. Furthermore, just the branch from zero to the maximum H_{app} is used for the evaluation. This can be justified because the critical current density is very high and therefore the reversible part of the magnetization is negligible. Second, the use of a magnetometer equipped with a bigger magnet would solve the problem. Fortunately, a Superconducting Interference Device (SQUID) magnetometer with a 7 T magnet is available for this thesis. The magnetic field provided by this magnetometer is sufficient to overcome $2\,H^*$ also for the irradiated single crystals. But, the measurement principle of the magnetic moment (will be described shortly in Sec. 2.2.2) is different than in a VSM which leads to another problem. For the magnetic measurement of J_{c} the electric field criterion is not chosen by the experimenter but by the used magnetometer set-up. The measurement in a VSM is usually done by constantly sweeping the magnetic field which defines the electric field criterion. On the other hand, the electric field criterion in a SQUID magnetometer is defined by the magnetic relaxation rate or the creep rate. These two criteria can differ significantly from each other making it difficult to compare measurements between these two magnetometers. The measurements of each individual sample will be done in the same magnetometer prior and after neutron irradiation to ensure that a change in J_{c} is not due to the chosen magnetometer.

The result of the above described procedure are magnetization loops, consisting of the increasing and the decreasing branch, at different temperatures which need to be evaluated [see Fig. 2.2.2(a)]. The simplest evaluation method for J_{c} is to use Eq. 2.2.1 which results in the critical current density as a function of the applied field. This is a sufficient evaluation method for several applications, but strictly speaking it is only a first approximation of J_{c}. Inside the sample not just the applied field is present, but also the field induced by the current density itself. The latter is used as a correction to the first approximation. With this correction, J_{c} can be given as function of the magnetic induction, B, and not of the applied field, H_{app}, which is closer to the actual material properties. The magnetic moment measured in a magnetometer is always a value for the whole sample volume. Since the field induced by the current density is not constant in the sample, an averaged value is used for the correction. This averaged field is called self-field, H_{self}, of the sample and used to correct both field branches of the hysteresis loop. For the increasing field branch the self-field points in the opposite direction as the applied field, decreasing it. Thus the actual magnetic field, B, for each measurement point in the increasing field

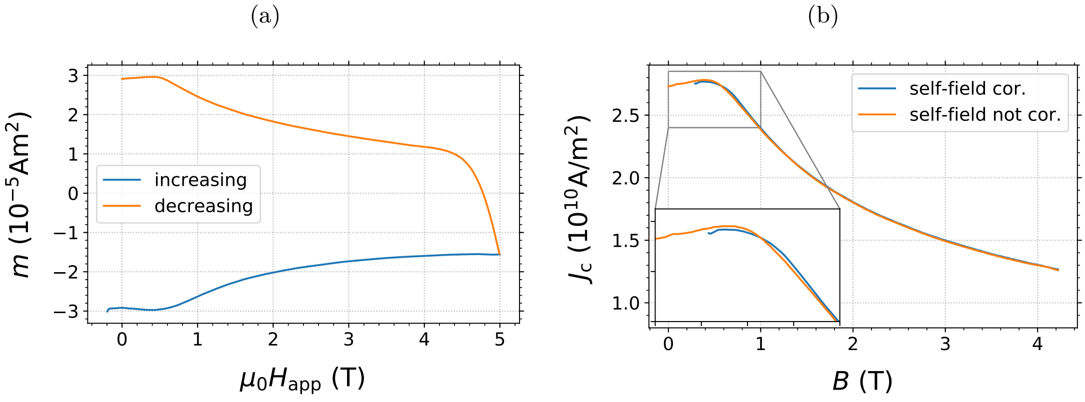

Fig. 2.2.2: Evaluation of the critical current density with and without self-field correction: (a) Measured hysteresis loops with increasing and decreasing branch labeled. (b) Critical current density calculated with $m(H)$ from (a) with and without a self-consistently self-field correction. The insert shows the low field range where the biggest differences between the self-field corrected and the not self-field corrected critical current density occur.

branch is: $B = H_{\rm app} - H_{\rm self}$. Contrary, the actual magnetic field is increased in the decreasing field branch: $B = H_{\rm app} + H_{\rm self}$. This change of the actual magnetic field of each data point shifts both field branches and thus $m_{\rm irr}$ changes. Furthermore, a change of $m_{\rm irr}$ also changes $J_{\rm c}$. This difference is shown in Fig. 2.2.2(b) where an evaluation without a self-field (first approximation with Eq. 2.2.1) and with a self-field correction is shown. The presence of the self-field is visible in $J_{\rm c}(B)$ because only field values bigger than the self-field are possible. The calculation of $J_{\rm c}$ and the self-field is done self-consistently in this thesis following [42]. This more complex evaluation of the critical current density is necessary because $J_{\rm c}$ and thus the self-field becomes large in the investigated samples. Additionally, $J_{\rm c}(B)$ is independent of the sample geometry which simplifies the comparison of properties of different samples in one doping system.

2.2.2 Critical Temperature

The critical temperature, $T_{\rm c}$, is an important quantity for a superconductor and there are two main techniques to determine it experimentally. First, it can be determined by measuring the resistivity of a sample as a function of the temperature. The second way, which is used in this thesis, is to measure $T_{\rm c}$ magnetically. This measurement can be subdivided further into two different methods: DC and AC susceptibility measurements. Both of these techniques probe the

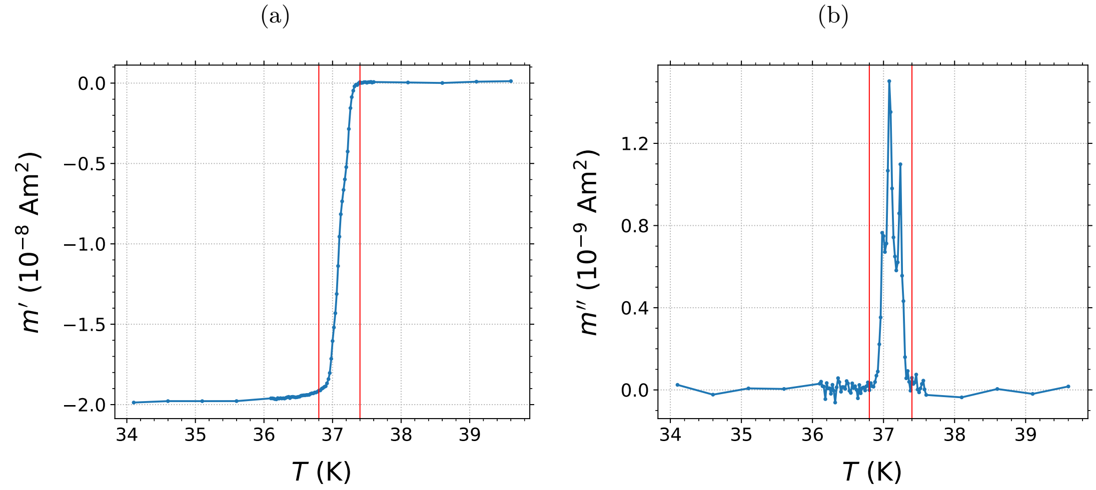

Fig. 2.2.3: Typical AC susceptibility measurement which is used to determine the critical temperature: (a) In-phase magnetic moment, m', as a function of temperature. (b) Out-of-phase magnetic moment, m'', as a function of temperature. The vertical red lines are at the same temperatures as in (a) and show the temperature range where dissipation takes place.

Meißner state of the superconductor by measuring the magnetic moment of the sample. For DC susceptibility measurements, a constant magnetic field is applied to the sample and the magnetic moment is measured as a function of the temperature. The applied field has to be smaller than H_{c1} for type-II superconductors to ensure the Meißner state of the sample. An AC susceptibility measurement probes the response of the sample to a small (in general smaller than the applied fields in DC susceptibility measurements) AC magnetic field. This response can be divided into an in-phase and an out-of-phase component of the magnetic moment. The first is the same as the one resulting from a DC measurement and the latter is a measure for the dissipation in the sample. Thus, a superconductor shows a peak in the out-of-phase component because energy is dissipated during the superconducting to normal conducting transition which can be seen in Fig. 2.2.3.

T_{c} is measured in this thesis by means of AC susceptibility as described above. This was done in a superconducting quantum interference device (SQUID) magnetometer (MPMS quantum design). A SQUID is a very complex device and a full description would be out of scope of this thesis, hence literature should be consulted for a more comprehensive description [43]. The basic principles are the flux quantization in a superconducting ring and the Josephson Effect.

These combined with sophisticated read-out electronics result in the most sensitive magnetometer available.

The AC susceptibility measurements to determine T_c were done with the magnetic field applied along the crystallographic *c*-axis of the samples and an amplitude of 30 μT. At the beginning of a measurement the sample was cooled to 5 K for centering in the SQUID magnetometer. This temperature was chosen because it is deep in the superconducting state. After this centering, the sample was warmed up above T_c to avoid trapped flux in the sample. The magnetic moment was then measured from a starting temperature higher than T_c to a certain temperature smaller than T_c [see Fig. 2.2.4 for an example measurement]. The transition from the normal conducting to the superconducting state is not a Heaviside step function, but there is a certain transition width. This requires the definition of a criterion for the transition temperature. There are several criteria used in literature, three of them are shown in Fig. 2.2.4. The criterion used throughout this thesis is the 10% criterion, which is the temperature at which 10% of the magnetic moment in the superconducting phase is reached. Thus, whenever T_c is used in this thesis it refers to $T_{\mathrm{c},10\%}$. The critical temperature $T_{\mathrm{c},90\%}$ is the temperature where 90% of the magnetic moment in the superconducting phase is reached. The third definition of the critical temperature is via the tangent criterion, $T_{\mathrm{c,tan}}$. There, a linear function is fitted to the transition range and $T_{\mathrm{c,tan}}$ is defined as the temperature where this linear fit reaches zero magnetic moment (or the magnetic moment in the normal conducting phase). An additional parameter used to characterize the superconducting transition is the transition width which is defined as: $\Delta T_\mathrm{c} = T_{\mathrm{c},10\%} - T_{\mathrm{c},90\%}$. All these temperatures are summarized in Fig. 2.2.4.

2.3 Neutron Irradiation

The irradiation with neutrons is a powerful method for the investigation of superconductors. Samples can be characterized prior to and after the irradiation minimizing sample-to-sample variation. Neutron irradiation introduces defects in the sample through nuclear collisions or reactions. These are the only possible ways how the neutral neutrons can interact with the sample. This interaction depends on the neutron cross section of the individual elements in the sample and therefore is quite complicated. Additionally, the neutrons usually used for irradiation

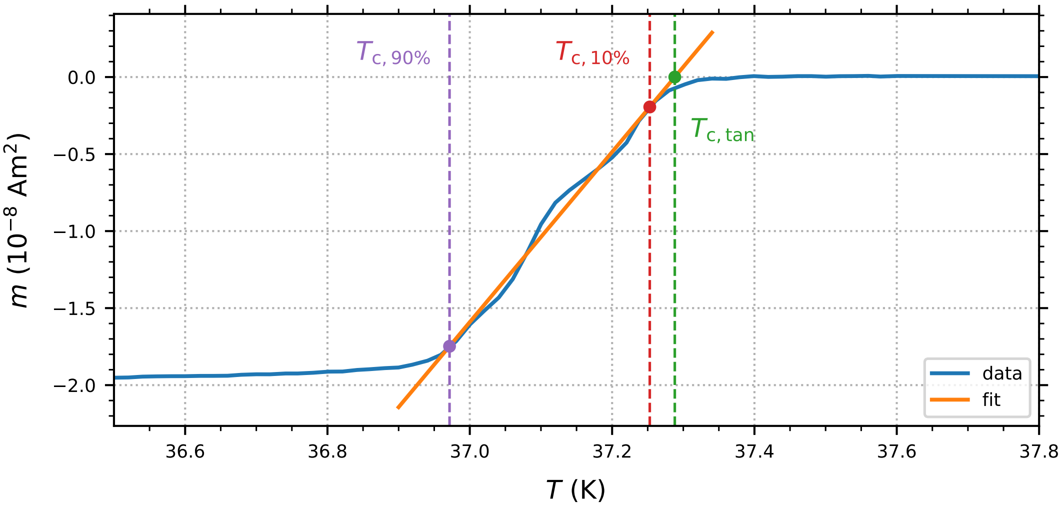

Fig. 2.2.4: Evaluation of the critical temperature. The in-phase magnetic moment is plotted as a function of temperature and a linear fit to the data in the transition is shown. The vertical lines denote the critical temperatures resulting from the different criteria. $T_{c,90\%}$ and $T_{c,10\%}$ are the temperatures where 90% and 10% of the magnetic moment in the superconducting phase is reached, respectively. $T_{c,\tan}$ is the critical temperature using the tangent criterion. It is defined as the temperature where the linear fit in the transition reaches the magnetic moment of the normal conducting phase (often zero).

stem from fission processes and thus have no fixed energy but rather a wide energy spectrum between 0.1 and 10 MeV. The penetration depth of these neutrons is several tens of centimeters, thus for the used single crystals the irradiation produces a homogeneous defect structure in the whole sample. The observation of these defects is a challenging task and was done with TEM in cuprates [44, 45, 46] and MgB_2 [47] but so far not in iron based superconductors. However, a similar defect structure is expected [23]. Namely, a homogeneously distributed high density of spherical defects with a diameter of approximately 5 nm.

The neutron irradiation in this thesis was carried out in the TRIGA research reactor at the Atominstitut, TU Wien. All samples of each doping set were irradiated together to ensure that they are all exposed to the same fluence. Prior to irradiation, the samples of a doping set together with a nickel foil were vacuum sealed in a quartz tube which minimizes the possibility of reactions between the air in the quartz tube and the samples during the irradiation. The nickel foil was used to measure the neutron fluence applied to the samples. Therefore, the ^{58}Co activity of the nickel foil was measured by γ-spectroscopy after the irradiation. The samples were thoroughly cleaned prior to the irradiation, which in combination with the vacuum sealing protected the samples from damage during the irradiation. All samples of one set were irradiated together. They were distinguished by their dimensions to prevent a mix up of the individual samples. The first irradiated set were the K-doped single crystals. They were irradiated for the same time period twice resulting in fast neutron fluences of $1.7 \cdot 10^{21}$ m^{-2} and $3.4 \cdot 10^{21}$ m^{-2}. The change of the properties between these two irradiation steps was small, thus the two other sets were irradiated just once to $3.4 \cdot 10^{21}$ m^{-2} corresponding to an irradiation time of 24 hours and 40 minutes [48].

Chapter 3

Results

The following chapter summarizes all collected data using the samples specified in Sec. 2.1 with the measurement techniques described in Sec. 2.2. It is organized in three sections: one for each doping system of Ba122. The main focus is on the comparison between properties of pristine and irradiated samples. Also, the critical temperature and the critical current density prior to and after irradiation is shown as a function of the doping concentration.

3.1 BaK122

Superconductivity is introduced in BaK122 ($Ba_{1-x}K_xFe_2As_2$) by hole doping which is realized by replacing barium with potassium. The phase diagram of BaK122, like every member of the Ba122 family, shows not only a superconducting phase but also an antiferromagnetic phase which is present in the under-doped range. Fig. 3.1.1 shows these doping levels and the area where superconducivity and antiferromagnetism are present. The investigated single crystals have dopant concentrations which cover the whole superconducting dome. More under-doped samples are included in the measurement set to cover the peak in $J_c(x)$ which is located at a lower doping concentration than the one in $T_c(x)$ [32]. The maximum T_c is reached at a potassium concentration between 0.3 and 0.4. This wide range is a result of the flat $T_c(x)$ curve [32]. The doping with maximum T_c is often referred to as optimally-doped and is located at 0.36 in the used sample set. This name can be misleading, especially in this doping system, because the

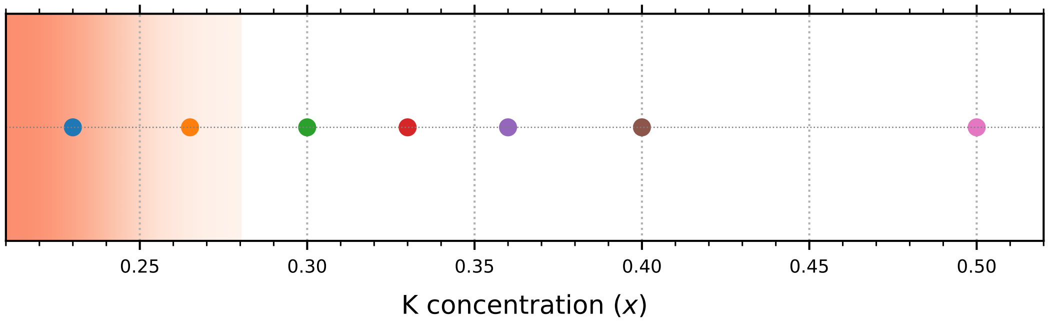

Fig. 3.1.1: Investigated doping levels of BaK122. The proximity to antiferomagnetism is indicated by the shaded area where a darker color represents a higher Néel temperature.

doping concentration regarding maximum J_c is different from the maximum in T_c. The optimal T_c doping divides the set in under- and over-doped samples.

The results of the BaK122 samples are presented in the following in two subsections, one for the pristine crystals and one for the irradiated crystals.

3.1.1 Pristine Crystals

The critical temperature and the critical current density of the pristine crystals were measured before the irradiation. The $m(T)$ curves of all samples are shown in Fig. 3.1.2. All transitions are sharp and no double transitions are present. Hence, the single crystals are homogeneous and of high quality. This is also true for the under- and over-doped samples which tend to be not as homogeneous as the optimally-doped crystals.

The magnetic moment as a function of the temperature is measured and evaluated according to Sec. 2.2.2. This results in a critical temperature for each doping level. Fig. 3.1.3 shows T_c as a function of the doping level. This plot nicely shows the dome shaped superconducting phase of the phase diagram. The values of T_c are in agreement with published data [32, 33]. T_c ranges from 23 K to a maximum value of 38.8 K for the optimally-doped crystal in this set.

The other quantity of interest is the critical current density. Fig. 3.1.4 shows J_c as a function of magnetic induction and temperature for all doping levels. These doping levels can be divided in two groups: under-doped samples and optimally- to over-doped samples. The under-doped samples exhibit potassium concentrations between 0.23 and 0.3. They show the appearance of

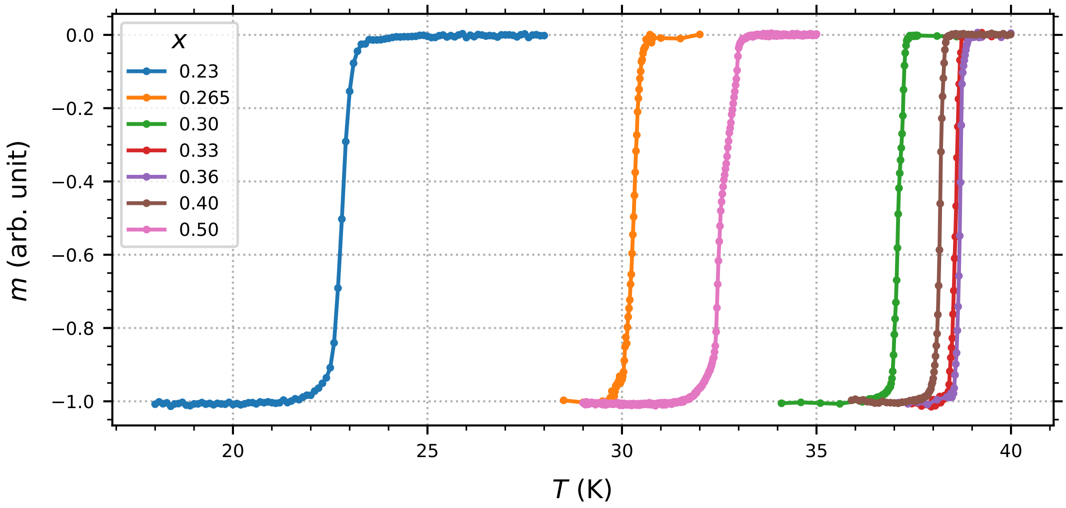

Fig. 3.1.2: Normalized magnetic moment as a function of the temperature for the pristine BaK122 samples.

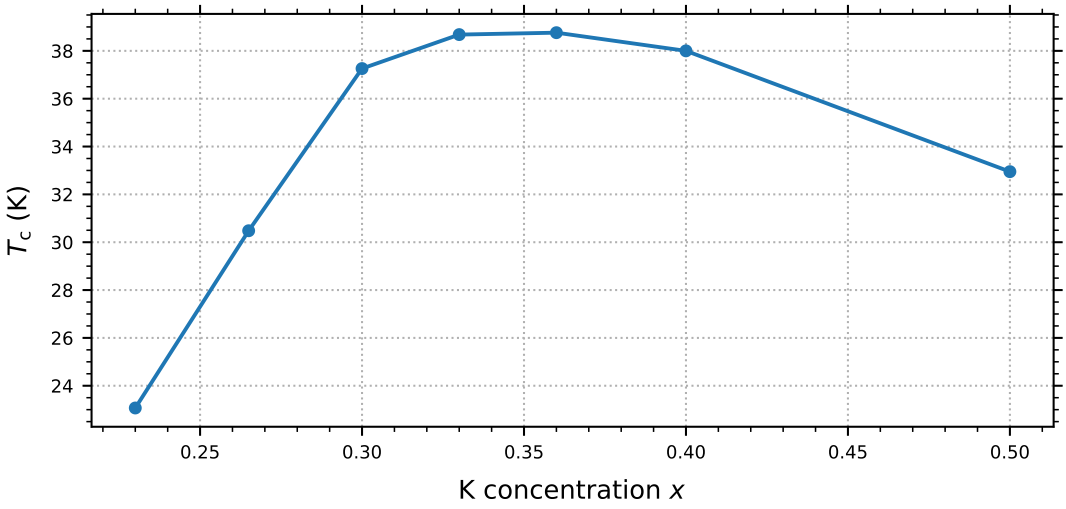

Fig. 3.1.3: Critical temperature of the pristine BaK122 samples as a function of the K concentration.

a so-called fishtail or second peak effect at higher temperatures. The fishtail occurs because the magnetization, and with it J_c, does not decrease monotonically with increasing applied field. At a certain temperature dependent field J_c shows a second peak. This is associated with an order-disorder transition in the flux line lattice. In the low field range, the elastic energy of the flux line lattice dominates whereas the pinning energy dominates at higher fields. This increasing influence of pinning results in an increase of J_c and the appearance of a peak. The position of this peak is temperature dependent and shifts into the measurement range for higher temperatures which can be seen in Fig. 3.1.4(a)-(c).

The optimally- and over-doped samples are the samples with a potassium concentration higher than 0.3. They do not show a fishtail except the sample with a K concentration of 0.5. These results suggest a disappearance of the fishtail at a doping level around 0.3 and then a reappearance at high doping levels. There are contradicting results on the presence and disappearance of a fishtail in BaK122 [32]. Nevertheless, the current results suggest a dependence of the appearance of the fishtail on the doping concentration.

The critical current density of the under-doped samples is higher than $10^9\,\mathrm{A/m^2}$ in the whole measured field range for temperatures up to 15 K. This J_c value is often used as a threshold value for practical applications. The sample with $x = 0.3$ has a J_c above $10^{10}\,\mathrm{A/m^2}$ at 5 K up to almost 2 T. J_c is in general smaller for $x > 0.3$, but shows small field dependence up to the highest reached fields of 5 T. The sample with the highest potassium concentration shows the smallest J_c which also decreases stronger with increasing fields than for the other samples.

It is already visible that $J_c(x)$ varies differently than $T_c(x)$ by comparing the critical current densities of the samples with doping concentration 0.3 [Fig. 3.1.4(c)] and 0.36 [Fig. 3.1.4(e)]. The difference in T_c between these two samples is about 1 K which is approximately 3%. Whereas, J_c of the sample with $x = 0.3$ is almost twice as big as J_c of the one with $x = 0.36$. This difference can be seen even better by plotting $J_c(x)$ at a fixed field for different temperatures which is shown in Fig. 3.1.5, where the mismatch between $T_c(x)$ and $J_c(x)$ is clearly visible. The former varies only little for the investigated samples forming the superconducting dome. Contrarily, the latter shows a peak in the under-doped range. This discrepancy is strongest for J_c at low temperatures but remains present also for higher temperatures. Additionally, the over-doped crystals show a small critical current density compared to the under-doped samples

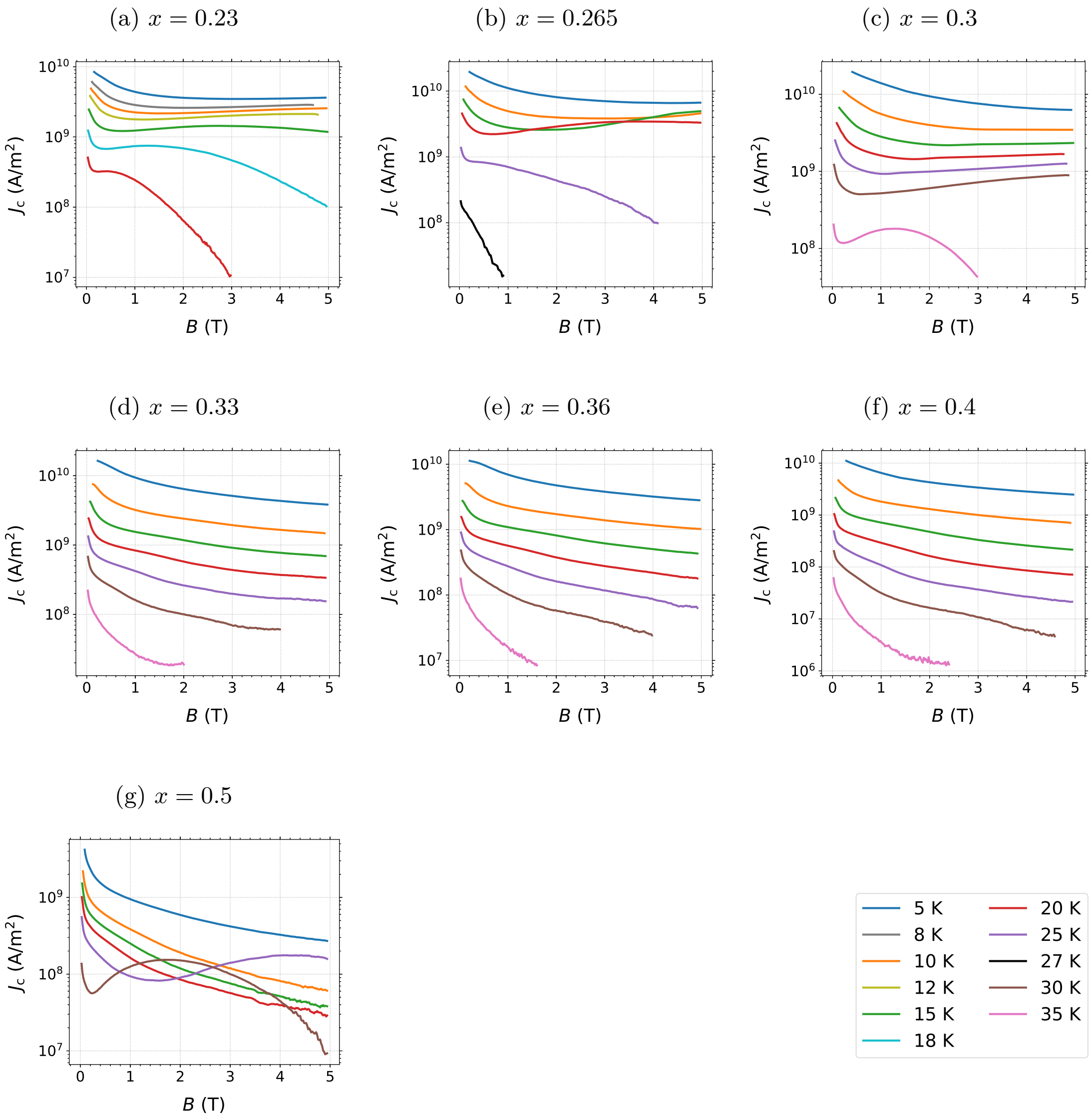

(a) $x = 0.23$ (b) $x = 0.265$ (c) $x = 0.3$

(d) $x = 0.33$ (e) $x = 0.36$ (f) $x = 0.4$

(g) $x = 0.5$

Fig. 3.1.4: Critical current density of the pristine BaK122 samples. Each subplot shows $J_c(B)$ at different temperatures for one dopant concentration.

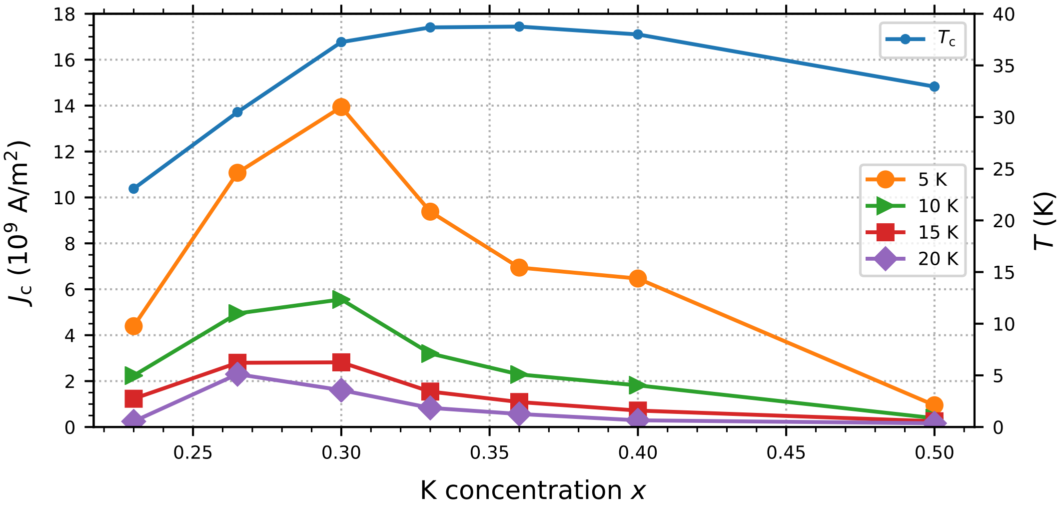

Fig. 3.1.5: Critical current density and critical temperature of the pristine BaK122 samples as a function of the K concentration. J_c is shown at $B = 1$ T and different temperatures.

and regarding their higher T_c. This peak in $J_c(x)$ persists also for higher fields but the shape changes because of the appearance of a fishtail in the under-doped samples.

3.1.2 Irradiated Crystals

The sample set characterized in Sec. 3.1.1 was irradiated with neutrons as described in Sec. 2.3. These samples where irradiated twice for the same time period resulting in neutron fluences of $1.7 \cdot 10^{21}$ m^{-2} and $3.4 \cdot 10^{21}$ m^{-2}. After each irradiation step the samples were characterized again.

The critical temperature decreased for all samples of the set. Fig. 3.1.6 shows $m(T)$ of the sample with $x = 0.3$ before irradiation and after each irradiation step. The transition shifts to smaller temperatures but the shape does not change. Moreover, the magnetic moment in the superconducting phase is the same for pristine and irradiated crystal which is an indication that the superconducting volume fraction did not change. Therefore, the measurement shows that the crystal was not damaged through the neutron irradiation. The other potassium doped crystals show similar behavior as the measurement shown in Fig. 3.1.6 except the sample with $x = 0.5$. The $m(T)$ curves for the sample with $x = 0.5$ are shown in Fig. 3.1.7. The pristine crystal shows

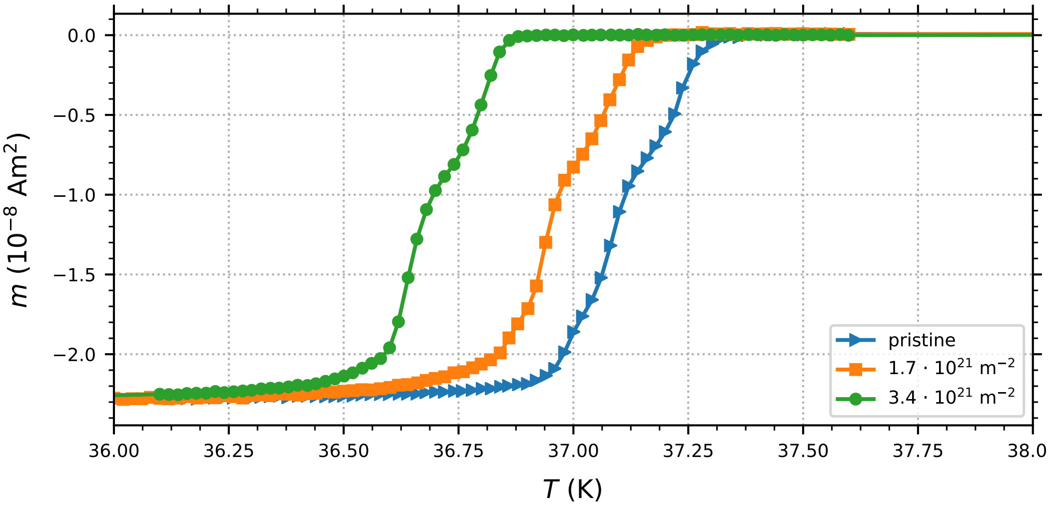

Fig. 3.1.6: Magnetic moment as a function of temperature of the sample with K concentration $x = 0.3$. $m(T)$ is shown for the pristine crystal and after each irradiation step.

a double transition and a tail reaching to lower temperatures. After the first irradiation, the double transition almost vanishes but the tail persists. Further irradiation increases the double transition but it is still smaller than in the pristine crystal.

The change of T_c after neutron irradiation for all samples except $x = 0.5$ is summarized in Fig. 3.1.8. The sample with $x = 0.5$ is excluded because the shape of the transition changed after irradiation which is shown in Fig. 3.1.7. Fig. 3.1.8 shows the reduction of the critical temperature, ΔT_c, normalized to T_c of the pristine crystals, T_c0, for all doping concentrations to account for the different T_c in the pristine samples. After the first irradiation step (pristine $\rightarrow 1.7 \cdot 10^{21}\mathrm{m}^{-2}$) the reduced decrease of T_c is almost constant for all doping concentrations. Further irradiation ($1.7 \cdot 10^{21}\mathrm{m}^{-2} \rightarrow 3.4 \cdot 10^{21}\mathrm{m}^{-2}$) results in more scattering, but no clear trend can be observed. However, the smallest reduction of T_c is measured around the optimal doping concentration in agreement with measurements on electron irradiated BaK122 [49]. Overall, the reduction of the critical temperature is small (i.e. up to 3%) after irradiation.

The critical current density of the irradiated crystals is shown in Fig. 3.1.9. J_c of all samples increased due to the introduction of a more efficient pinning landscape through the neutron irradiation. The fishtail vanishes for the under-doped samples. It is also no longer present for

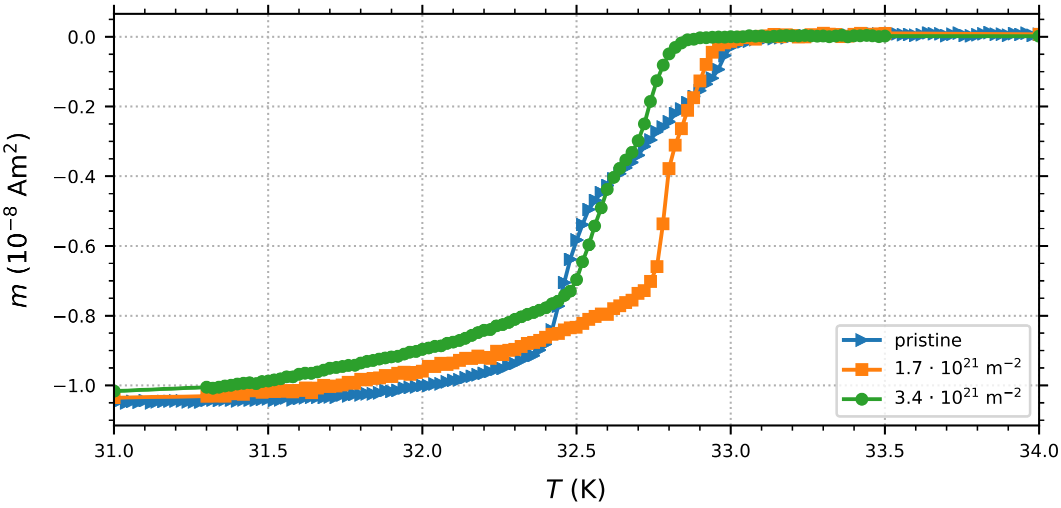

Fig. 3.1.7: Magnetic moment as a function of temperature of the sample with K concentration $x = 0.5$. $m(T)$ is shown for the pristine crystal and after each irradiation step.

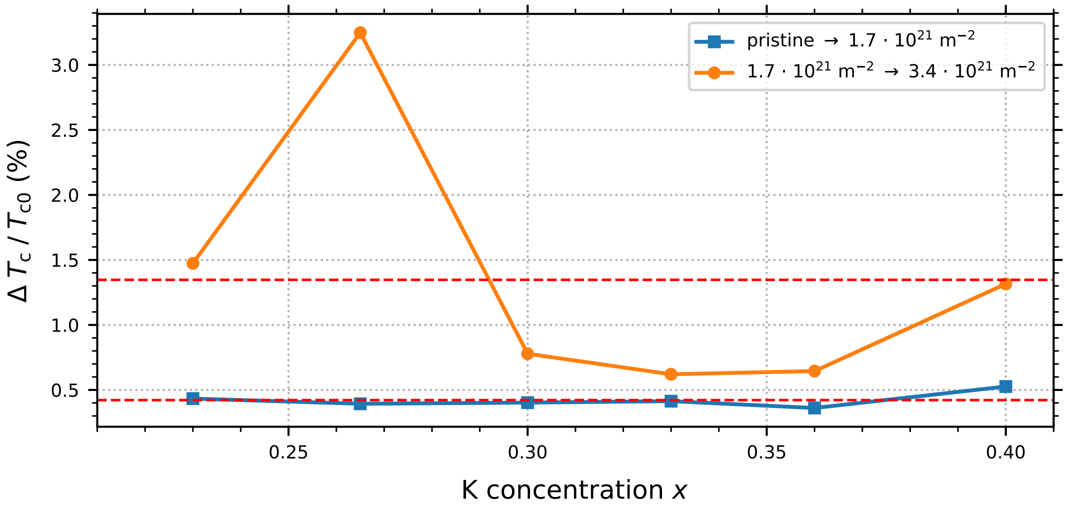

Fig. 3.1.8: Relative reduction of T_c after each irradiation step in percent as a function of the K concentration.

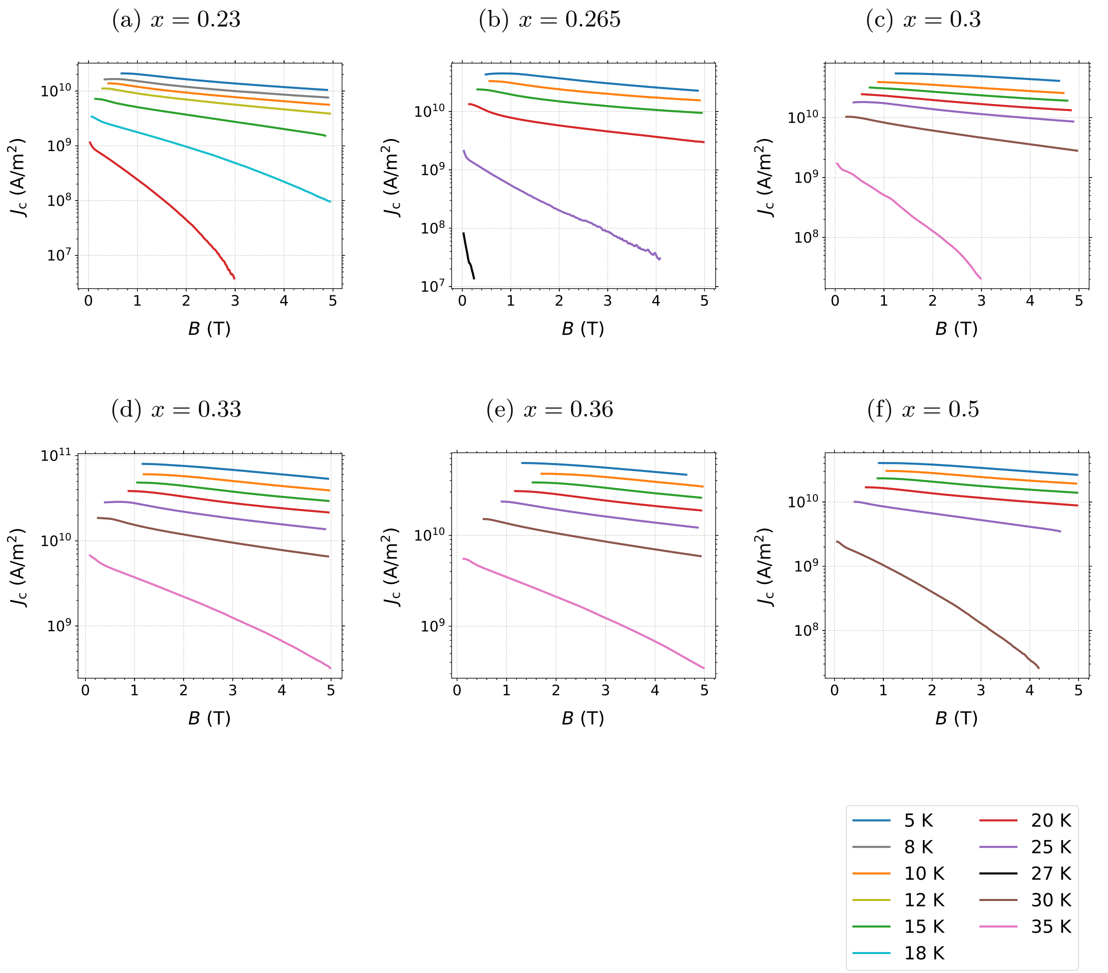

(a) $x = 0.23$ (b) $x = 0.265$ (c) $x = 0.3$

(d) $x = 0.33$ (e) $x = 0.36$ (f) $x = 0.5$

Fig. 3.1.9: Critical current density of the BaK122 samples irradiated to a fluence of $3.4 \cdot 10^{21}\,\mathrm{m}^{-2}$. Each subplot shows $J_c(B)$ at different temperatures for one dopant concentration.

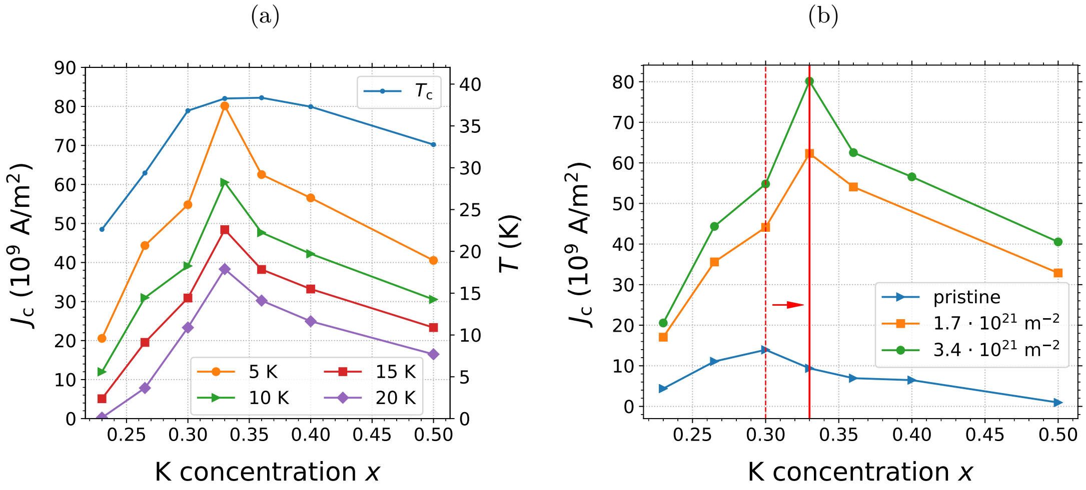

Fig. 3.1.10: Critical current density as a function of the K concentration of the samples irradiated to a fluence of $3.4 \cdot 10^{21}\mathrm{m}^{-2}$. (a) $J_c(x)$ at 1 T and different temperatures alongside with $T_c(x)$ of the irradiated BaK122 samples. (b) Comparison of $J_c(x)$ of the pristine crystals and after each irradiation step. The shift of the maximum is indicated by the red arrow.

the sample with $x = 0.5$. The field dependence of J_c is in general smaller than for the pristine samples. J_c is higher than $10^9\mathrm{A/m}^2$ for temperatures up to 30 K and fields up to 5 T in the samples with doping concentration between 0.3 and 0.36. This is also true for temperatures smaller than 20 K for the sample with $x = 0.5$. The increase of J_c is bigger for the over-doped samples and the highest J_c value of $8 \cdot 10^{10}\mathrm{A/m}^2$ is reached by the sample with $x = 0.33$ at self-field [see Fig. 3.1.9(d)]. The increase of the critical current density leads to an increase of the self-field of the samples. This takes place in all samples and can be seen in Fig. 3.1.9. The self-field reaches values of up to 1.5 T in the presented samples. Fig. 3.1.9 misses a plot of the sample with $x = 0.4$ which was characterized as pristine crystal [see Fig. 3.1.4(f)]. This sample showed such a high self-field after the first irradiation step to $1.7 \cdot 10^{21}\mathrm{m}^{-2}$ that it was not possible to evaluate J_c in a big enough temperature and field range [see Sec. 2.2.1]. Therefore, the sample was not irradiated further. Fortunately, a sample with the same doping concentration was previously measured at a fluence of $3.4 \cdot 10^{21}\mathrm{m}^{-2}$ in the Low Temperature and Superconductivity Group at Atominstitut [50]. The data set is available and is used for the $J_c(x)$ investigations. This is justified by the agreement of T_c and J_c of the pristine crystals.

J_c of the samples with $0.3 \leq x \leq 0.36$ varies only little between doping levels [see Fig. 3.1.9(c)-(e)].

A similar behavior is observed comparing T_c of these samples. This contrasts the behavior of the pristine crystals where $J_c(x)$ shows a distinctively different shape than $T_c(x)$. Fig. 3.1.10(a) shows J_c as a function of the dopant concentration for different temperatures at $B = 1$ T or self-field if it exceeds 1 T. This plot includes $T_c(x)$ to show the similar shape compared to $J_c(x)$. This similarity has one outlier namely the sample with $x = 0.33$. It forms a small peak which is preserved at all measured temperatures. The drastic change of $J_c(x)$ due to neutron irradiation can be seen in Fig. 3.1.10(b) where J_c is plotted at 5 K and 1 T for the different irradiation steps. J_c increases due to the introduction of a pinning landscape which is more efficient than the intrinsic defects of the crystals for all samples. Before irradiation the peak in $J_c(x)$ is in the under-doped area which shifts to the doping level where the maximum T_c is reached. This shift happens already after the first irradiation step. Further irradiation increased J_c in a similar way for all doping concentrations. The increase of J_c is bigger for optimally- and over-doped samples compared to under-doped ones.

3.2 BaP122

Superconductivity is introduced in BaP122 ($BaFe_2(As_{1-x}P_x)_2$) by an isovalent replacement of arsenic with phosphorous. This doping is different than the hole or electron doping because it is an isovalent doping and superconductivity emerges through internal pressure in the lattice due to the different sizes of arsenic and phosphorous. The existence of a quantum critical point (QCP) is discussed in this doping system [51]. This QCP and its appearance by a peak in the magnetic penetration depth was associated with a sharp peak in $J_c(x)$ [34]. Therefore, the doping levels of this set were chosen to cover the superconducting dome and additionally to resolve the sharp peak in $J_c(x)$. The distribution of the doping of the used crystals is shown in Fig. 3.2.1, where the high density of samples around the optimal doping of approximately $x = 0.3$ can be seen. This is the doping where the sharp peak in $J_c(x)$ was previously observed [32].

3.2.1 Pristine Crystals

The magnetic moment as a function of temperature was measured for all samples in this set and used to evaluate the critical temperature. The respective $m(T)$ curves are shown in Fig. 3.2.2

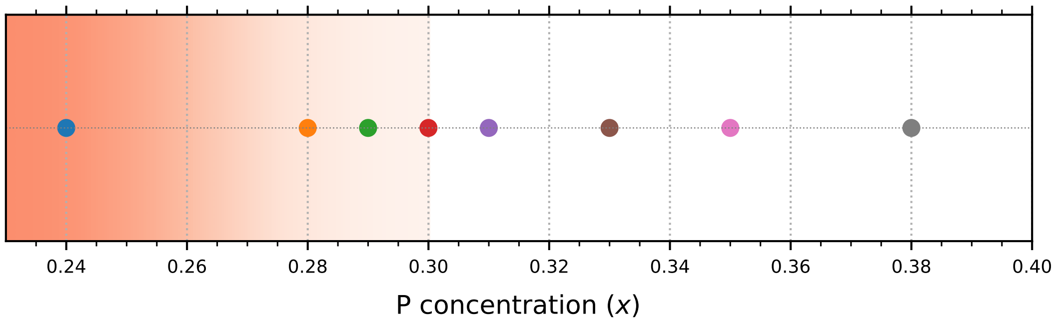

Fig. 3.2.1: Investigated doping levels of BaP122. The proximity to antiferomagnetism is indicated by the shaded area where a darker color represents a higher Néel temperature.

for all doping levels. The crystals with a doping range $0.26 \leq x \leq 0.31$ show sharp transitions with very similar values for T_c. The transitions for the crystals out of this range are broader and show a tail to lower temperatures. The crystal with the highest ($x = 0.38$) and the crystal with the lowest ($x = 0.24$) doping concentration exhibit the broadest transitions from normal to superconducting. Additionally, the sample with $x = 0.24$ shows a double transition.

The $m(T)$ curves from Fig. 3.2.2 were evaluated following Sec. 2.2.2 to further investigate the doping dependence of the transition temperature. T_c as a function of the dopant concentration is plotted in Fig. 3.2.3, where the superconducting dome with a flat maximum around $x = 0.3$ can be seen. From this maximum doping T_c decreases slowly to the over-doped samples. This decrease is stronger to the under-doped side of the superconducting dome. Unfortunately not that many under-doped samples were available, leading to a gap between $x = 0.28$ and $x = 0.24$. All the T_c values are in agreement with previously published data [32]. The critical temperature ranges from 19.2 K for the crystal with the lowest phosphorous concentration up to 29.5 K for the optimally-doped crystal.

Fig. 3.2.4 shows the critical current density as a function of the magnetic induction at different temperatures for all doping levels. J_c is in general lower than in BaK122. A critical current density higher than $10^{10}\mathrm{A/m^2}$ is reached only in the samples with $x = 0.29$ and $x = 0.3$ at 5 K up to a field of 0.5 T and at 10 K at a field not much higher than the self-field. The doping levels with J_c above $10^9\mathrm{A/m^2}$ at higher fields and temperatures are in a narrow range around $x = 0.29$ which shows the highest J_c [see Fig. 3.2.4(c)-(e)]. This is also the doping range were J_c depends

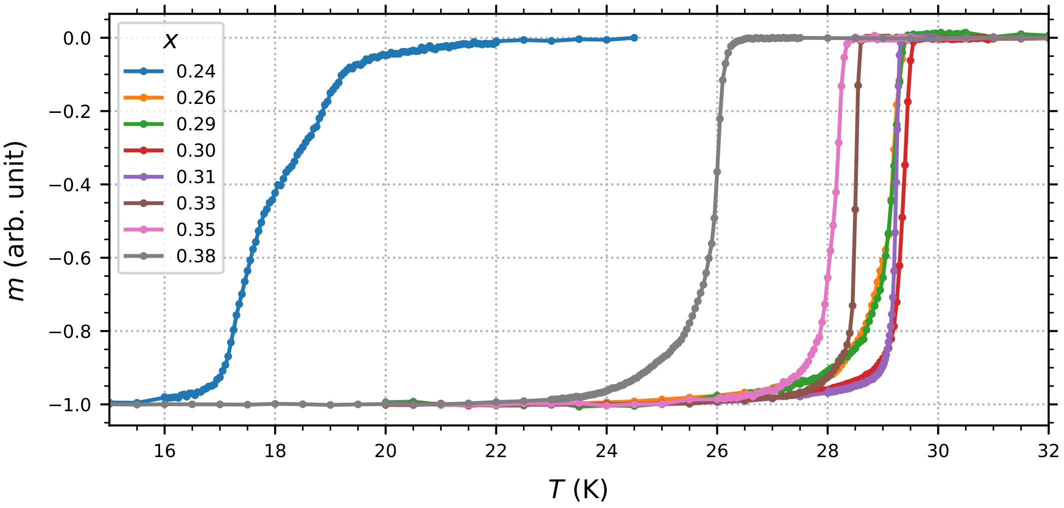

Fig. 3.2.2: Normalized magnetic moment as a function of the temperature for the pristine BaP122 samples.

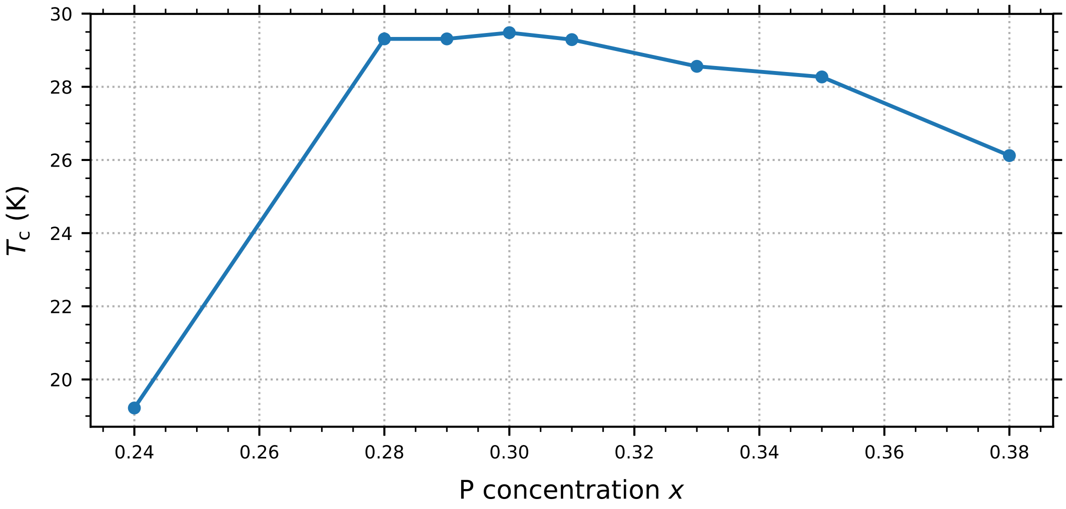

Fig. 3.2.3: Critical temperature of the pristine BaP122 samples as a function of the P concentration.

only little on B for temperatures up to 20 K. J_c of the crystals in this doping range decreases from its maximum at self-field and afterwards stays almost constant up to the maximum field of 5 T. Higher doping levels with $x \geq 0.31$ already show a smaller J_c which depends stronger on B [see Fig. 3.2.4(e)-(h)]. This can be seen by a stronger decrease of J_c after its initial maximum at self-field. The sample with the lowest P concentration [Fig. 3.2.4(a)] and the sample with the highest P concentration [Fig. 3.2.4(h)] exhibit the smallest J_c of this batch. J_c exceeds $10^9\,\mathrm{A/m^2}$ only at low temperatures and low fields. The critical temperature varies less than 0.2 K in the doping range $0.28 \leq x \leq 0.31$. Contrarily, the critical current density in the sample with $x = 0.29$ is almost double as in the one with $x = 0.31$. This is similar to the situation in BaK122 and shows the mismatch between $J_\mathrm{c}(x)$ and $T_\mathrm{c}(x)$.

All the investigated doping levels show a fishtail which occurs especially at higher temperatures closer to the respective T_c. Additionally, the samples can be divided into two groups by the shape of their $J_\mathrm{c}(B)$ curves. The first group, which consists of the samples with $x \leq 0.30$, shows no crossing of the $J_\mathrm{c}(B)$ curves at different temperatures. The samples with $x \geq 0.33$ form the second group where the $J_\mathrm{c}(B)$ curves at different temperatures cross each other. The crystal with the doping level $x = 0.31$ [Fig. 3.2.4(e)] is an intermediate between these two groups because the $J_\mathrm{c}(B)$ curves at different temperatures start to touch each other at this doping level.

The difference between $J_\mathrm{c}(x)$ and $T_\mathrm{c}(x)$ can be nicely seen in Fig. 3.2.5, where $T_\mathrm{c}(x)$ and $J_\mathrm{c}(x)$ at 1 T and different temperatures are shown. $J_\mathrm{c}(x)$ exhibits a clear peak at $x = 0.29$ which persists up to 15 K. At this dopant concentration $T_\mathrm{c}(x)$ shows a flat maximum spanning from $x = 0.28$ to $x = 0.31$. Therefore, the doping concentration with maximum T_c and maximum J_c almost coincide. In contrast to BaK122, the peak in BaP122 is more pronounced and not positioned in the under-doped range. After the peak $J_\mathrm{c}(x)$ shows a flat plateau and then starts to further decrease for higher doping concentrations. This plateau looks similar at temperatures up to 15 K. The sample with $x = 0.24$ shows almost no irreversible moment at 15 K and 1 T [see Fig. 3.2.4(a)] because this temperature is close to the wide transition of this crystal.

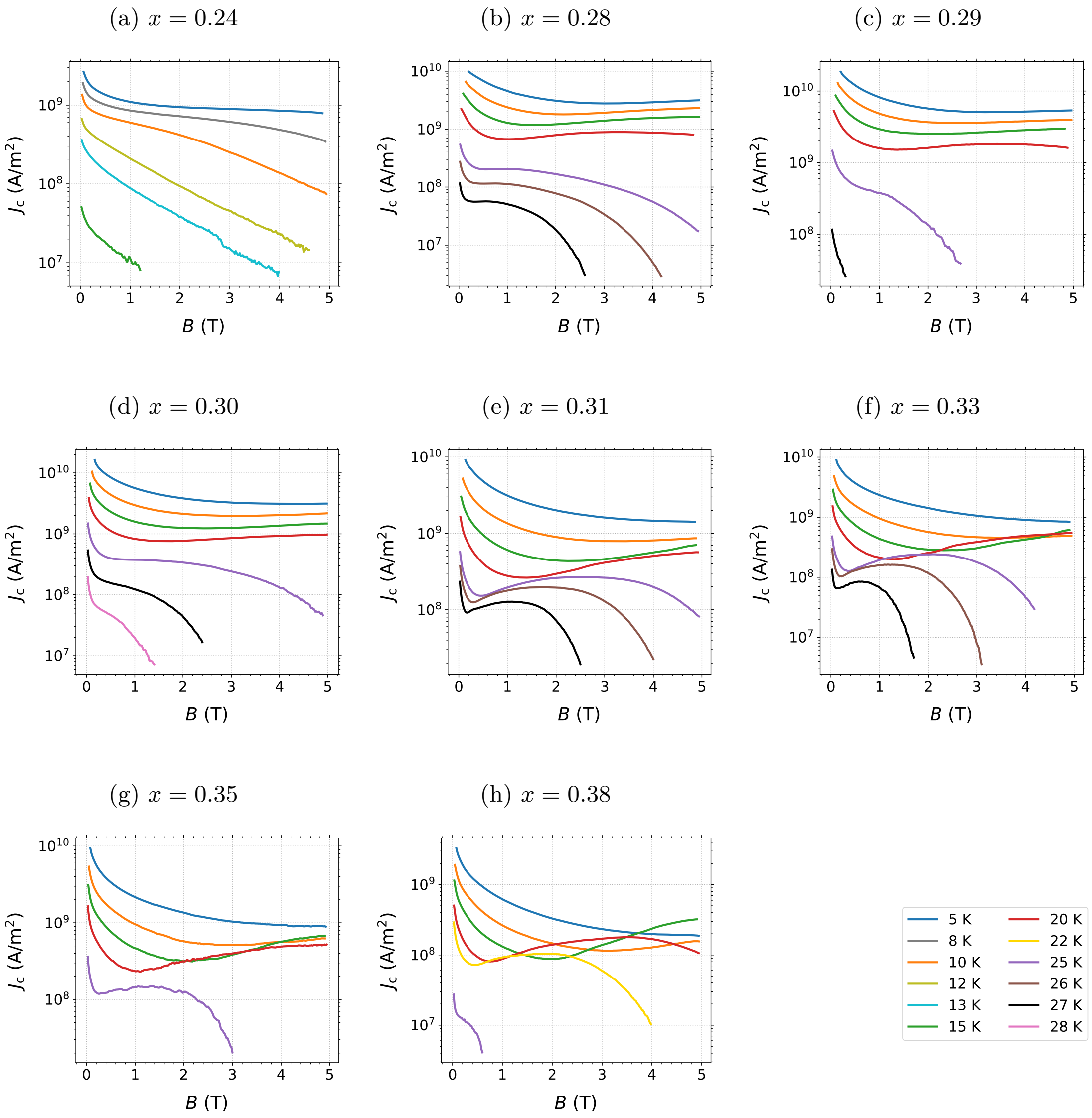

(a) $x = 0.24$ (b) $x = 0.28$ (c) $x = 0.29$

(d) $x = 0.30$ (e) $x = 0.31$ (f) $x = 0.33$

(g) $x = 0.35$ (h) $x = 0.38$

Fig. 3.2.4: Critical current density of the pristine BaP122 samples. Each subplot shows $J_c(B)$ at different temperatures for one dopant concentration.

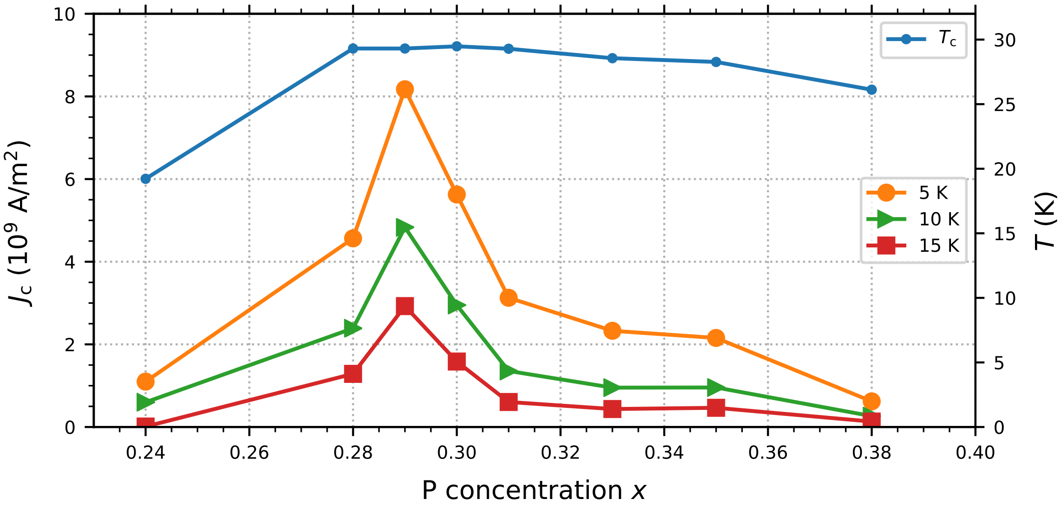

Fig. 3.2.5: Critical current density and critical temperature of the pristine BaP122 samples as a function of the P concentration. J_c is shown at $B = 1$ T and different temperatures.

3.2.2 Irradiated Crystals

The samples doped with phosphorous where irradiated with neutrons as described in Sec. 2.3. Since the investigation of the BaK122 samples showed no further changes after the first irradiation step, this set was irradiated in one step. A fluence of $3.4 \cdot 10^{21}$ m^{-2} was chosen to ensure the comparability between the doping sets and to ensure that the introduced defect landscape is more efficient for flux pinning than the defects in the pristine crystals.

The critical temperature decreased for all P concentrations as in the K-doped system. The relative decrease of T_c is shown in Fig. 3.2.6 which enables the comparison of the different doping levels with different pristine T_c values. This relative change decreases almost monotonically with increasing dopant concentration. An outlier of this trend is the crystal with $x = 0.29$, where the relative decrease exhibits a peak. This is the same doping level where the peak in $J_c(x)$ is present in the pristine crystals. The relative reduction of T_c for the samples with $x \geq 0.3$ is approximately 1% which is in the same order of magnitude as in BaK122. The peak at $x = 0.29$ is very similar to a peak in the relative decrease of T_c in BaK122 [see Fig.3.1.8]. However, the peak there is at a lower dopant concentration as the position of the peak in $J_c(x)$. The biggest relative and absolute reduction of T_c was measured in the sample with $x = 0.24$. This is also the

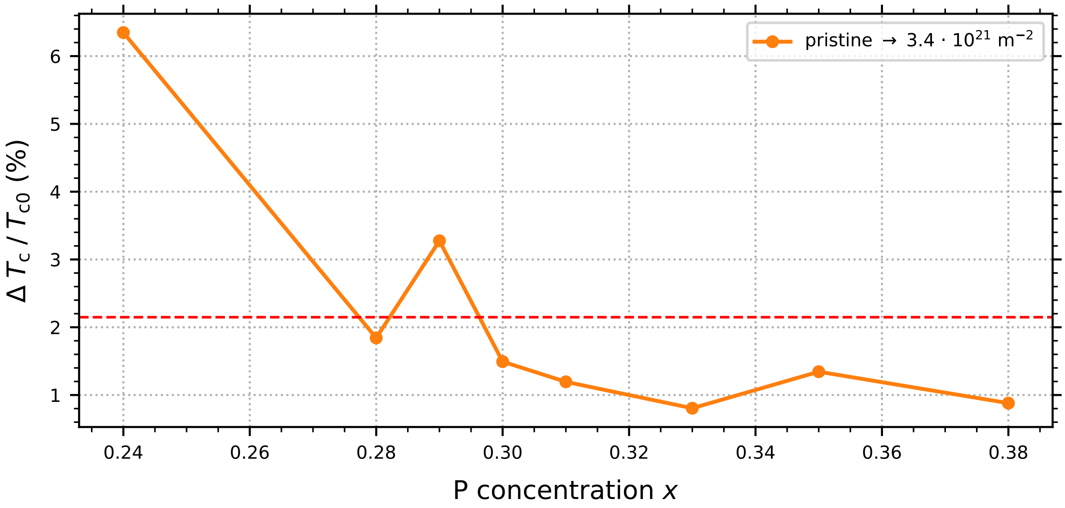

Fig. 3.2.6: Relative reduction of T_c after the irradiation in percent as a function of the P concentration.

sample with the widest transition seen in the $m(T)$ measurement.

The critical current density strongly increased for all dopant concentrations as in BaK122. Fig. 3.2.7 shows J_c as a function of B at different temperatures after the irradiation for all doping levels. The first obvious difference to the pristine crystals is the disappearance of the fishtail for all doping concentrations which was also observed in BaK122. The dependence of J_c on B is smaller for the irradiated crystals. Thus, J_c exhibits higher values also at higher fields. The pristine crystals showed $J_\mathrm{c} > 10^9\,\mathrm{A/m^2}$ at higher fields and temperatures only in a narrow doping range around $x = 0.29$. After irradiation this is reached in the samples with $0.28 \leq x \leq 0.35$ for temperatures up to 20 K in the whole measurement range with a maximum field of 5 T. Even $J_\mathrm{c} > 10^{10}\,\mathrm{A/m^2}$ is reached in the doping range $0.29 \leq x \leq 0.35$ at temperatures up to 10 K in the whole measurement range. Such high J_c was only reached at low temperatures and self-field in some pristine crystals. The maximum J_c of $4.9 \cdot 10^{10}\,\mathrm{A/m^2}$ is measured in the crystal with $x = 0.3$ at self-field and 5 K [see Fig. 3.2.7(d)]. This is almost half the value found in irradiated BaK122. The smaller J_c values lead to a smaller self-field because the sample sizes of BaK122 and BaP122 are comparable. The self-field does not exceed 1 T at any temperature for any doping level. Therefore the problems with high self-fields in the evaluation of J_c in irradiated

BaK122 did not occur in the irradiated BaP122 samples.

The samples with $x = 0.3$ and $x = 0.33$ have a very similar T_c and showed quite different J_c values before the irradiation. Comparing $J_c(B)$ of the irradiated crystals [Fig. 3.2.7(d) and 3.2.7(f)] does not show a big difference any more. The J_c values of both crystals are very similar. This change of $J_c(x)$ due to irradiation can be seen in Fig. 3.2.8. Fig. 3.2.8(a) shows $J_c(x)$ at 1 T and different temperatures alongside with $T_c(x)$. The increase of J_c is biggest in the optimally- and over-doped samples. This was also the case in the irradiated BaK122 samples. Furthermore, the peak present in the pristine crystals not only widened and shifted to higher doping levels but a second peak appeared [see Fig. 3.2.8(b)]. The dip at $x = 0.31$ is present in all measured temperatures but its depth decreases with increasing temperature.

The inspection of $J_c(B)$ of the crystal with $x = 0.31$ [Fig. 3.2.7(e)] does not reveal obvious differences to the surrounding doping levels. A possible explanation for the dip is a change of the superconducting volume fraction through the irradiation which would change the volume for the J_c evaluation [see Eq. 2.2.1]. Such a change would appear as a change in the magnetic moment in the superconducting phase. The $m(T)$ measurements of this crystal are shown in Fig. 3.2.9 with a magnification of the magnetic moment in the superconducting phase. This shows that the magnetic moment is smaller after the irradiation which indicates a change of the superconducting volume. Therefore, the crystal was inspected in a digital microscope for cracks which would change the superconducting volume. Fig. 3.2.10 shows two side views of the crystal where a crack is visible in Fig. 3.2.10(a). On the other side of the crystal [Fig. 3.2.10(b)] the crack is no longer visible which indicates that the crack does not reach through the whole crystal. Usually Ba122 single crystals easily cleave, but the crack visible in Fig. 3.2.10(a) left the crystal intact. This crack reaches along the *ab*-plane of the crystal, thus, J_c in the *ab*-plane should not be influenced. However, it could be possible that further damage along the crack was done which could effect J_c of the crystal.

3.3 BaCo122

Superconductivity is introduced in BaCo122 ($\mathrm{Ba(Fe_{1-x}Co_x)_2As_2}$) by electron doping. This is achieved by replacing iron with cobalt which directly affects the iron-arsenic-layers which are

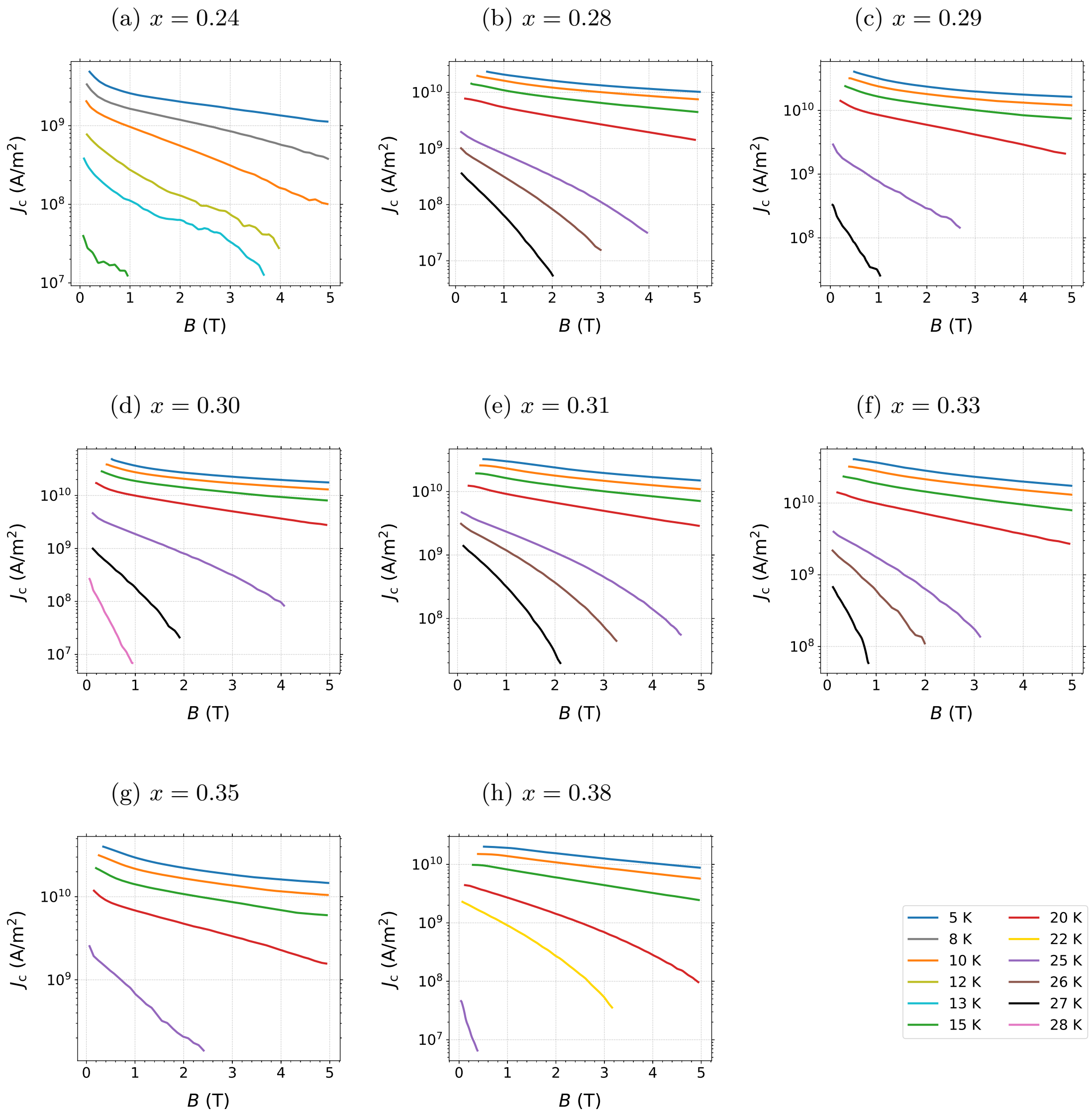

(a) $x = 0.24$

(b) $x = 0.28$

(c) $x = 0.29$

(d) $x = 0.30$

(e) $x = 0.31$

(f) $x = 0.33$

(g) $x = 0.35$

(h) $x = 0.38$

Fig. 3.2.7: Critical current density of the BaP122 samples irradiated to a fluence of $3.4 \cdot 10^{21}\,\mathrm{m}^{-2}$. Each subplot shows $J_c(B)$ at different temperatures for one dopant concentration.

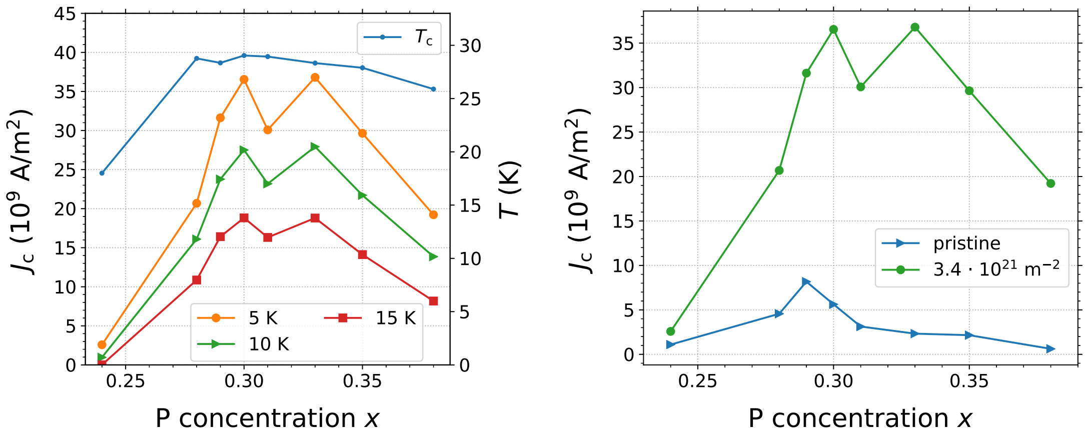
(a) (b)

Fig. 3.2.8: Critical current density as a function of the P concentration of the samples irradiated to a fluence of $3.4 \cdot 10^{21}\mathrm{m}^{-2}$. (a) $J_c(x)$ at 1 T and different temperatures alongside with $T_c(x)$ of the irradiated BaP122 samples. (b) Comparison of $J_c(x)$ prior to and after the irradiation.

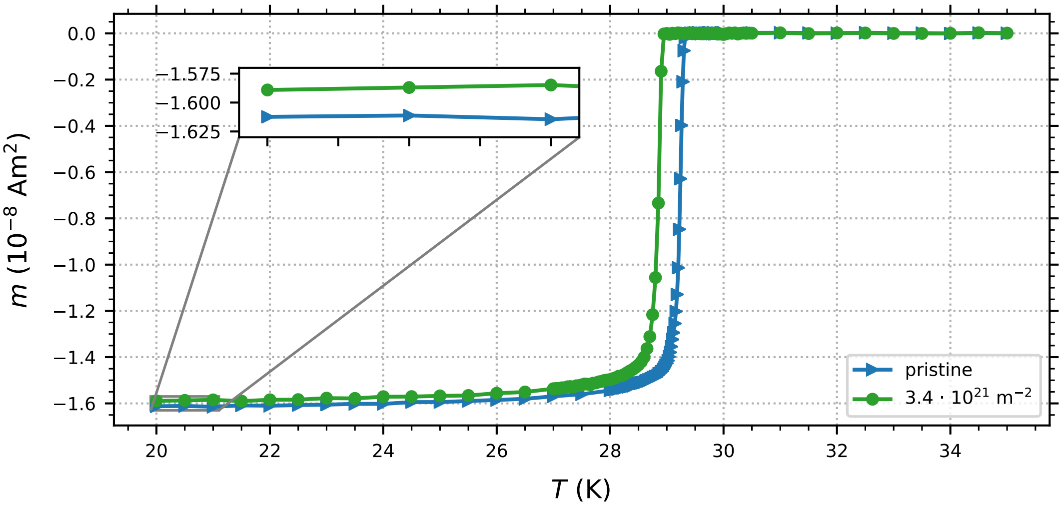

Fig. 3.2.9: Magnetic moment as a function of temperature of the sample with P concentration $x = 0.31$. $m(T)$ is shown prior to and after the irradiation. The insert shows a zoom to indicate the difference between the magnetic moment in the superconducting phase of the pristine and the irradiated sample.

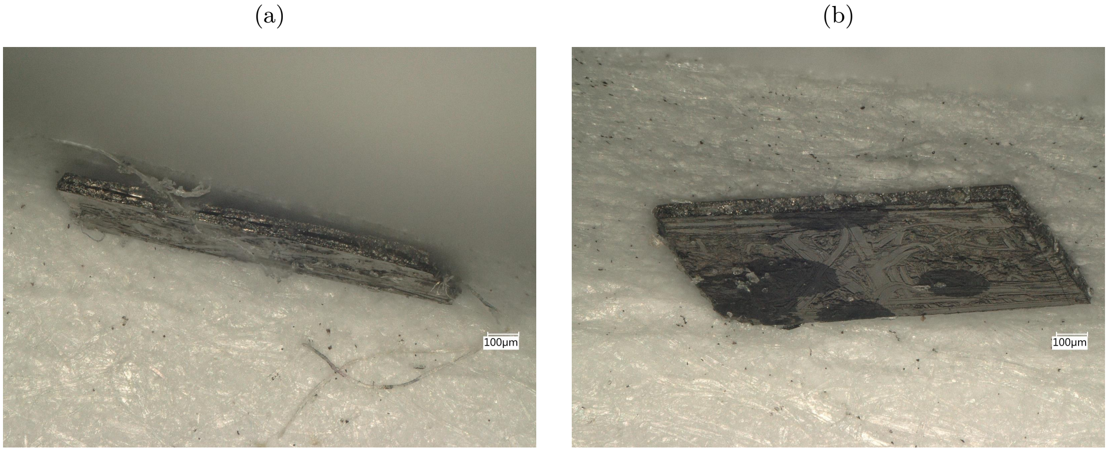

Fig. 3.2.10: Microscope image of the sample with P concentration $x = 0.31$. (a) Side view of the crystal. A crack through the whole side of the crystal is visible. (b) Side view of the other side of the crystal. No crack is visible indicating that the crack does not go through the whole crystal in this direction.

central for superconductivity in iron based materials. Therefore, the doping concentrations are significantly smaller than for example in the hole doped BaK122. The doping concentrations of the crystals in this doping set are chosen to cover the superconducting dome and resolve the maximum J_c at a slightly smaller dopant concentration than 0.06. Superconductivity and antiferromagnetism exist in close proximity in this system like in the other doping systems of Ba122. The doping concentrations of the samples in this set and the doping range where superconductivity and antiferromagnetism exist together are shown in Fig. 3.3.1.

Compared to BaK122 and BaP122, BaCo122 exhibits the smallest T_c and J_c. However, it is the doping system where the growth of crystals with a wide variety of doping concentrations is easiest. Therefore most of the studies of Ba122 are done with BaCo122. This is also the doping system where the thickest crystals can be grown.

The magnetization measurements to determine J_c were carried out not only in the VSM like in the other two doping systems. The pristine crystals were characterized in a VSM and after the irradiation the magnetization measurements were performed in a SQUID magnetometer because the VSM was out of service. These two devices produce not exactly the same results regarding J_c as mentioned in Sec. 2.2.1. One crystal was measured in the VSM and the SQUID to quantify the difference resulting from the different measurement technique. This difference was negligible

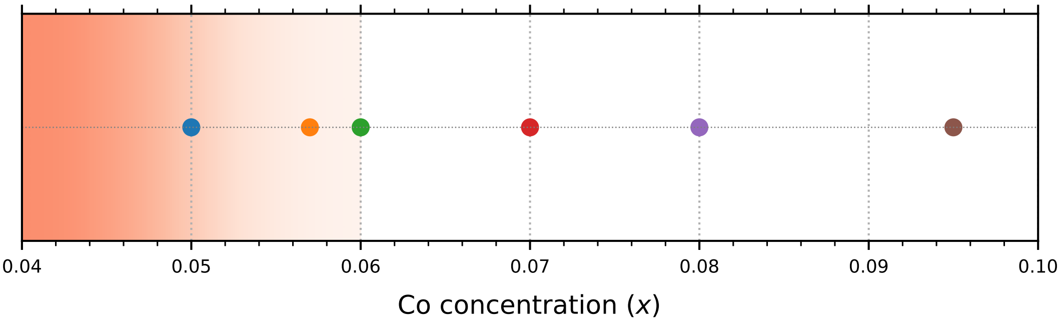

Fig. 3.3.1: Investigated doping levels of BaCo122. The proximity to antiferomagnetism is indicated by the shaded area where a darker color represents a higher Néel temperature.

regarding the strong increase of J_c after neutron irradiation.

3.3.1 Pristine Crystals

The critical temperature for all samples was evaluated using the $m(T)$ curves shown in Fig. 3.3.2. The transitions of all crystals are narrow which is a sign for the good sample quality. The crystal with the smallest cobalt concentration of $x = 0.05$ shows a transition with a tail after the transition reaching to smaller temperatures. This behavior was previously shown for under-doped samples [32]. The sample with the highest cobalt concentration of $x = 0.095$ has a transition which starts out less steep and reaches a slope which is comparable to the other samples in the middle of the transition.

The curves in Fig. 3.3.2 were used following Sec. 2.2.2 to evaluate the critical temperature of all samples. The doping dependence of T_c is shown in Fig. 3.3.3. The superconducting dome has a flat maximum at $x = 0.07$ where the maximum T_c of 24 K is reached. This is the smallest maximum T_c in the three investigated doping systems of Ba122. The crystal with $x = 0.05$ exhibits the smallest T_c of 14.7 K in this set. T_c increases with a steep slope from this doping level and reaches the flat maximum between a dopant concentration of 0.06 and 0.07. The decrease of T_c at higher doping concentrations has as smaller slope than the increase from under to optimal doping.

The critical current density as a function of B at different temperatures for all doping levels is shown in Fig. 3.3.4. J_c in the Co-doped system is the smallest among the three investigated

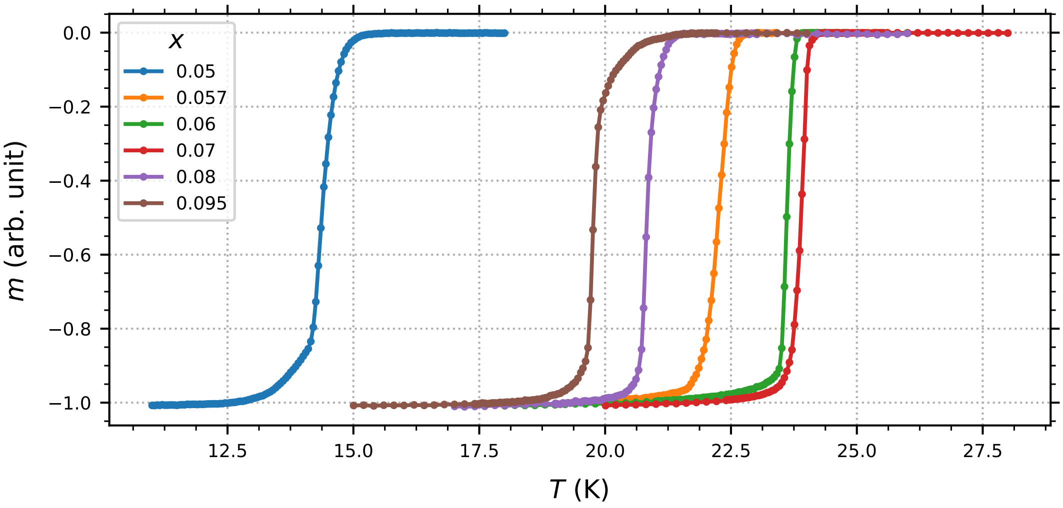

Fig. 3.3.2: Normalized magnetic moment as a function of the temperature for the pristine BaCo122 samples.

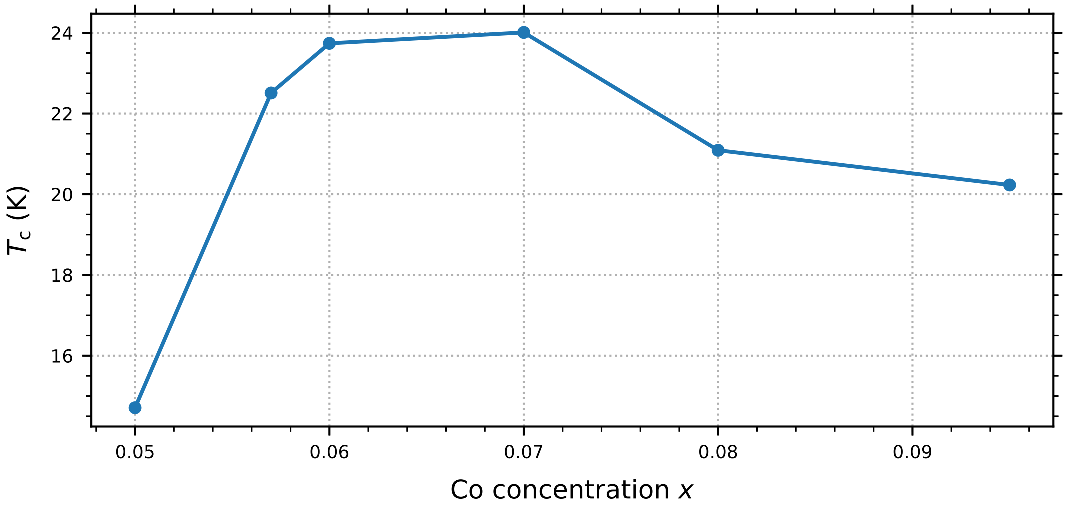

Fig. 3.3.3: Critical temperature of the pristine BaCo122 samples as a function of the Co concentration.

doping systems. A critical current density above $10^{10}\,\mathrm{A/m^2}$ is not achieved in any of the crystals. The highest J_c of $9.7 \cdot 10^9\,\mathrm{A/m^2}$ is reached in the sample with $x = 0.057$ at 5 K and self-field. The samples with $0.057 \leq x \leq 0.7$ [see Fig. 3.3.4(b)-(d)] have a J_c exceeding $10^9\,\mathrm{A/m^2}$ up to 5 T and 12 K. Apart from the sample with $x = 0.05$ all samples show a similar B dependence of the J_c curves. After a decrease at low fields, J_c stays almost constant up to 5 T at temperatures up to 10 K. The appearance of a fishtail is visible in all samples at higher temperatures. Its maximum shifts to smaller fields with increasing temperature but no crossover of $J_\mathrm{c}(B)$ curves at different temperatures like in BaP122 is visible. The critical current density in the sample with $x = 0.05$ [Fig. 3.3.4(a)] is the lowest in this set and shows a stronger field dependence than the other samples.

The critical temperature of the crystals with $x = 0.057$ and $x = 0.07$ are 1.5 K different from each other which is a difference of about 7%. Comparing J_c at self-field and 5 K of these crystals in Fig. 3.3.4(b) and 3.3.4(d) a difference of approximately 20% is observed. This mismatch is similar as in pristine BaK122 and BaP122. J_c at $B = 1$ T and T_c as functions of the doping concentration is shown in Fig. 3.3.5, where the different shape of $T_\mathrm{c}(x)$ and $J_\mathrm{c}(x)$ can be seen. The peak in $J_\mathrm{c}(x)$ is not as pronounced as in BaP122 [see Fig. 3.2.5] but a clear difference to $T_\mathrm{c}(x)$ can be seen. The crystal with maximum T_c is different from the crystal with maximum $J_\mathrm{c}$like in BaK122. The latter is at a lower doping concentration, $x = 0.057$, than the former, $x = 0.07$. The maximum in $J_\mathrm{c}(x)$ stays at the same position for temperatures up to 10 K. Higher temperatures are not plotted in Fig. 3.3.5 because J_c becomes small in the sample with $x = 0.05$ but the general shape of $J_\mathrm{c}(x)$ stays the same. The critical current density starts at $x = 0.05$ with a low value. After that, a strong increase to the maximum J_c at $x = 0.057$ takes place. Further doping results in a decrease of J_c up to the sample with the highest cobalt concentration of $x = 0.095$. J_c of this crystal is comparable with J_c of the sample with the lowest doping concentration.

3.3.2 Irradiated Crystals

The irradiation to a fluence of $3.4 \cdot 10^{21}\,\mathrm{m^{-2}}$ was done following Sec. 2.3. Like in BaP122, no intermediate irradiation step was performed. This was done to ensure the comparability of the

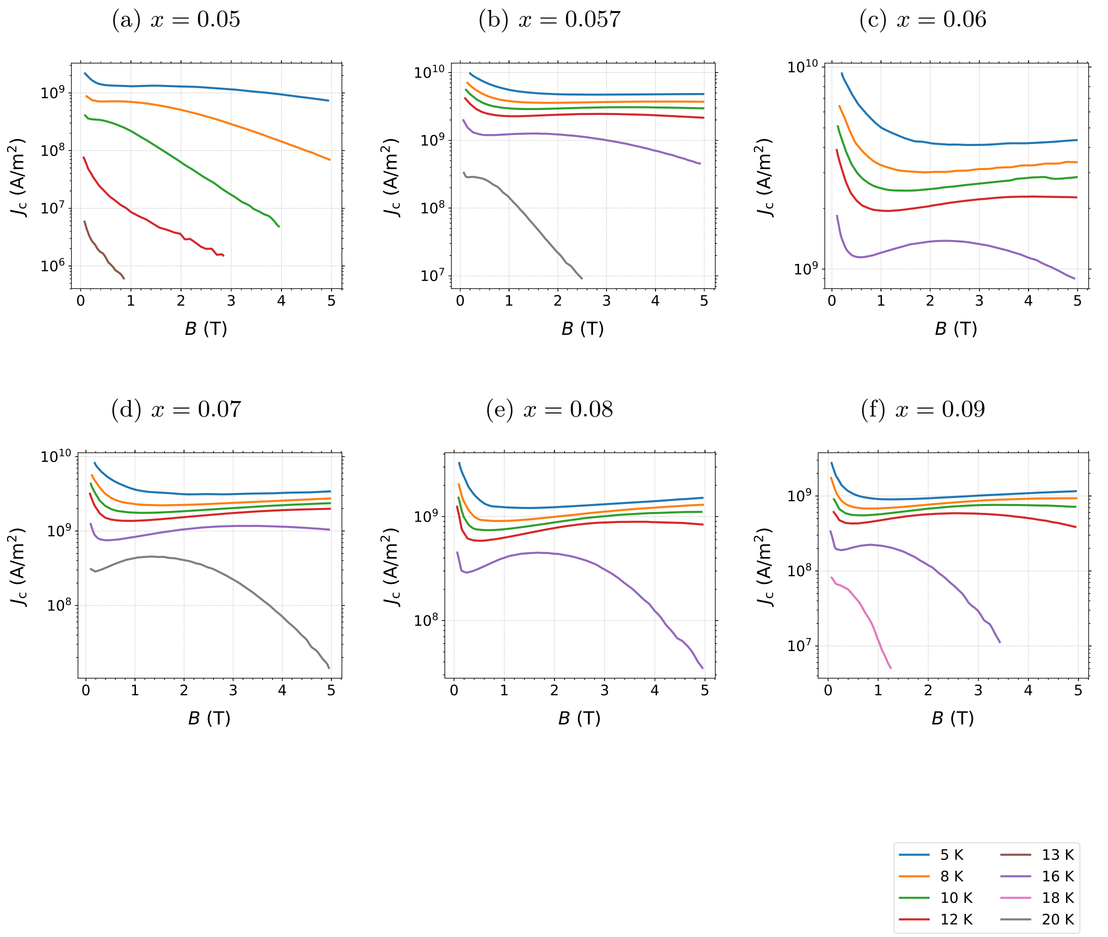

(a) $x = 0.05$ (b) $x = 0.057$ (c) $x = 0.06$

(d) $x = 0.07$ (e) $x = 0.08$ (f) $x = 0.09$

Fig. 3.3.4: Critical current density of the pristine BaCo122 samples. Each subplot shows $J_c(B)$ at different temperatures for one dopant concentration.

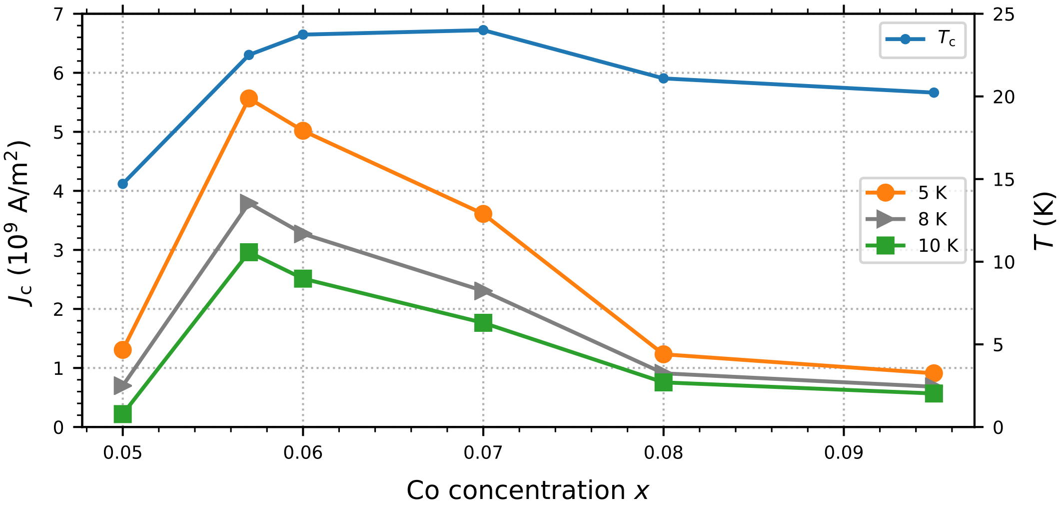

Fig. 3.3.5: Critical current density and critical temperature of the pristine BaCo122 samples as a function of the Co concentration. J_c is shown at $B = 1$ T and different temperatures.

three investigated doping systems and because the measurements on BaK122 showed that this fluence is sufficient to introduce a pinning landscape which is more efficient than the pristine one.

The critical temperature decreased in all cobalt doped crystals like in the phosphorus and potassium doped systems. Fig. 3.3.6 shows the relative T_c reduction for all Co-doped samples. The relative reduction makes it possible to compare samples with different dopant concentrations and therefore different critical temperatures. The biggest reductions are seen in the samples with $x = 0.05$ and $x = 0.095$ which are the samples with the smallest and highest cobalt concentration, respectively. This relative reduction is comparable to the maximum relative reduction measured in BaP122 which takes place in the crystal with the smallest phosphorus concentration [see Fig. 3.2.6]. Almost no T_c reduction after neutron irradiation is found in the sample with $x = 0.057$. For closer inspection, the $m(T)$ curve of this sample is shown in Fig. 3.3.7. The insert in this figure is a zoom to the onset of the transition which shows a smaller T_c for the irradiated sample. However, this difference is very small and the $m(T)$ curves of the pristine and irradiated crystal almost match each other. Especially, the magnetic moment in the superconducting phase is the same which indicates the same superconducting volume fraction prior to and after the

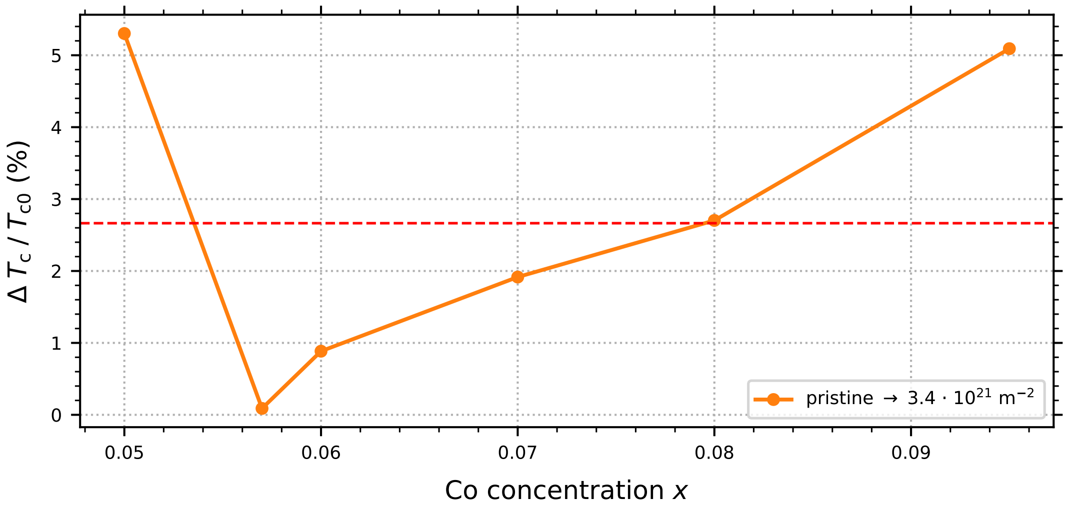

Fig. 3.3.6: Relative reduction of T_c after the irradiation in percent as a function of the Co concentration.

irradiation. The relative T_c reduction decreases from its maximum at $x = 0.05$ to its minimum at $x = 0.07$ and afterwards increases monotonically with further doping. The average T_c reduction is approximately 2.5% which is the highest decrease seen in the three investigated doping systems.

The critical current densities of all irradiated crystals as a function of the magnetic induction at different temperatures are shown in Fig. 3.3.9. J_c increased in all samples after the neutron irradiation. The smallest increase was measured in the crystal with $x = 0.05$ [see Fig. 3.3.8(a)]. All other crystals have J_c values higher than $10^{10}\mathrm{A/m^2}$ at self-field and 5 K which was not reached in any pristine crystal. The crystal with $x = 0.07$ reached the maximum J_c of this set which is $2.3 \cdot 10^{10}\mathrm{A/m^2}$. A J_c above $10^9\mathrm{A/m^2}$ is reached in the samples with $0.057 \leq x \leq 0.08$ at fields up to 4 T and temperatures below 12 K [see Fig. 3.3.8(b)-(e)]. The field dependence of J_c of all samples changed due to the neutron irradiation. The fishtail is not present any more in the investigated field and temperature range. Furthermore, all the $J_c(B)$ curves decrease with an almost constant slope in the logarithmic plot with increasing field. This contrasts the field dependence of J_c in the pristine crystals, where J_c strongly decreased at small fields and stayed almost constant for a further increase of the field [see Fig. 3.3.4]. As in all other three doping systems, an increase of the self-field due to the J_c increase can be observed in all samples.

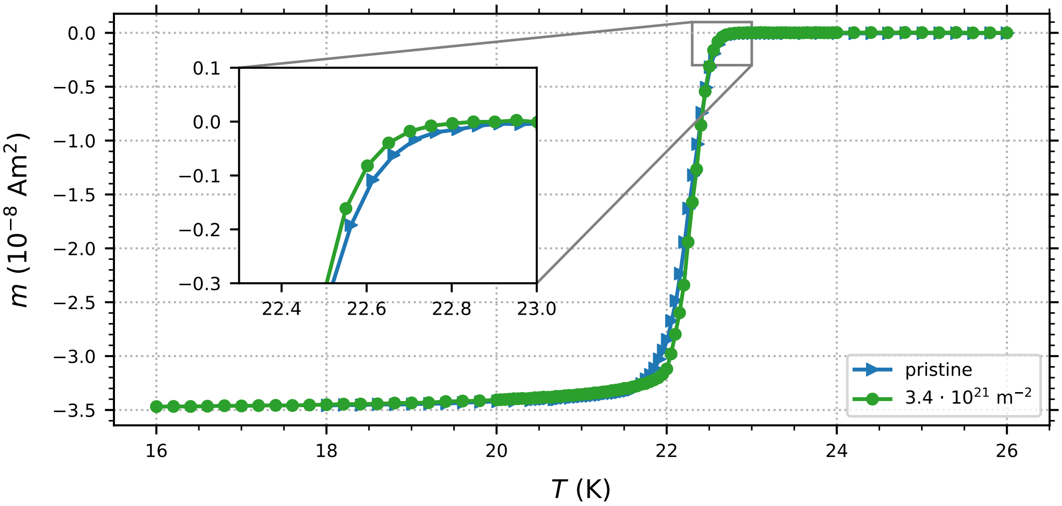

Fig. 3.3.7: Magnetic moment as a function of temperature of the sample with Co concentration $x = 0.057$. $m(T)$ is shown prior to and after the irradiation. The insert shows a zoom to the onset of the transition. The small T_c reduction due to the irradiation can be seen in this plot.

The self-field is smaller than 1 T at all measured temperatures like in BaP122. Thus the J_c evaluation does not suffer from problems like in BaK122. The $J_\mathrm{c}(B)$ curves of this doping set only extend to 4 T and not to fields close to 5 T like in the other doping sets. This can be attributed to the different magnetometer used for these crystals. They were measured in a SQUID magnetometer and not in a VSM like the other samples. This measurement technique involves usually bigger field steps especially at higher fields (> 3 T). The region where the field profile turns around is ignored in the J_c evaluation with both hysteresis branches [see Sec. 2.2]. Since the next measurement in the decreasing branch takes place at 4 T this is the last point where J_c is evaluated.

The strong increase of J_c due to the neutron irradiation can be seen by comparing the pristine and irradiated $J_\mathrm{c}(B)$ curves of the sample with $x = 0.07$ in Fig. 3.3.4(d) and Fig. 3.3.8(d), respectively. This is also reflected in the doping dependence of J_c. Fig. 3.3.9(a) shows $J_\mathrm{c}(x)$ at 1 T for different temperatures alongside with $T_\mathrm{c}(x)$. After the neutron irradiation the shape of $J_\mathrm{c}(x)$ is more similar to the dome formed by $T_\mathrm{c}(x)$. The sample with $x = 0.07$ is a small outlier to this shape. It is the sample with the maximum T_c and forms a small peak in $J_\mathrm{c}(x)$.

The peak in $J_\mathrm{c}(x)$ shifts to higher doping concentrations and widens as can be seen in

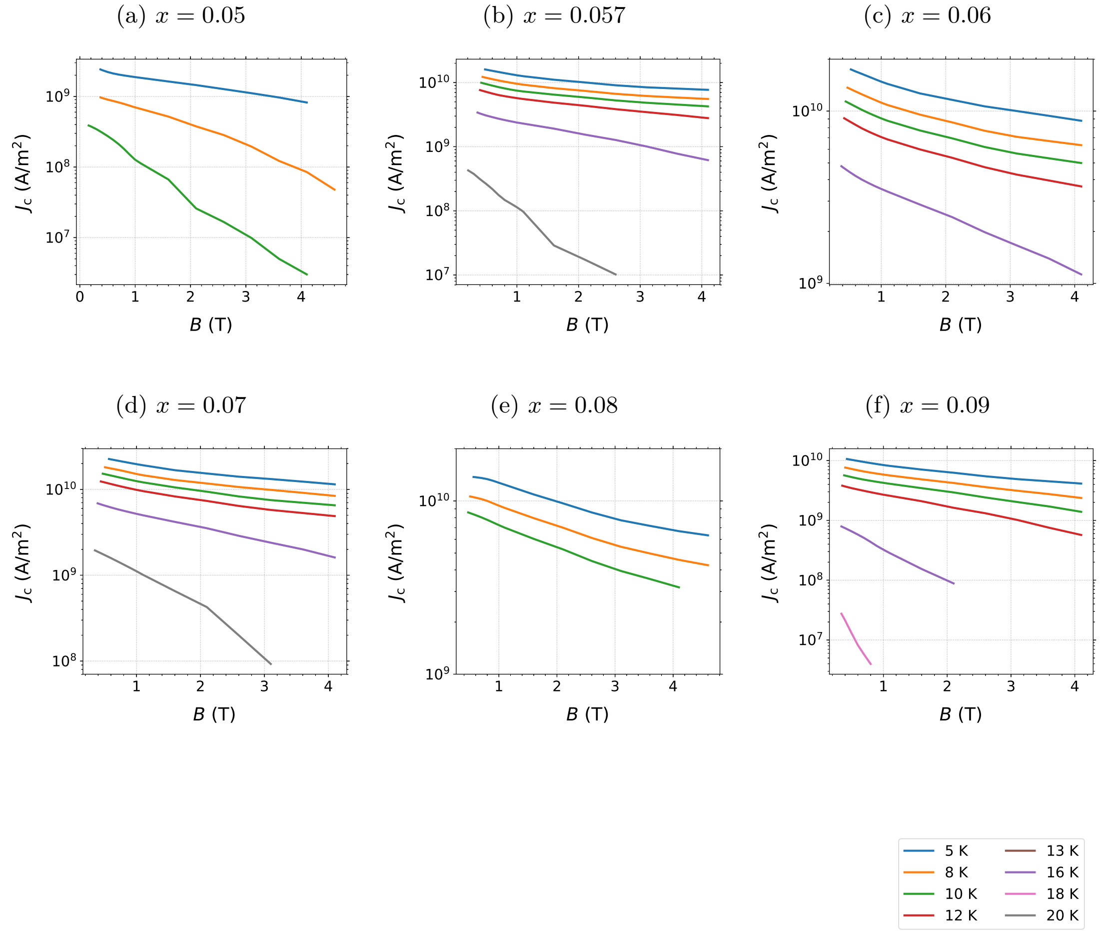
(a) $x = 0.05$ (b) $x = 0.057$ (c) $x = 0.06$
(d) $x = 0.07$ (e) $x = 0.08$ (f) $x = 0.09$

Fig. 3.3.8: Critical current density of the BaCo122 samples irradiated to a fluence of $3.4{\cdot}10^{21}\,\mathrm{m}^{-2}$. Each subplot shows $J_c(B)$ at different temperatures for one dopant concentration.

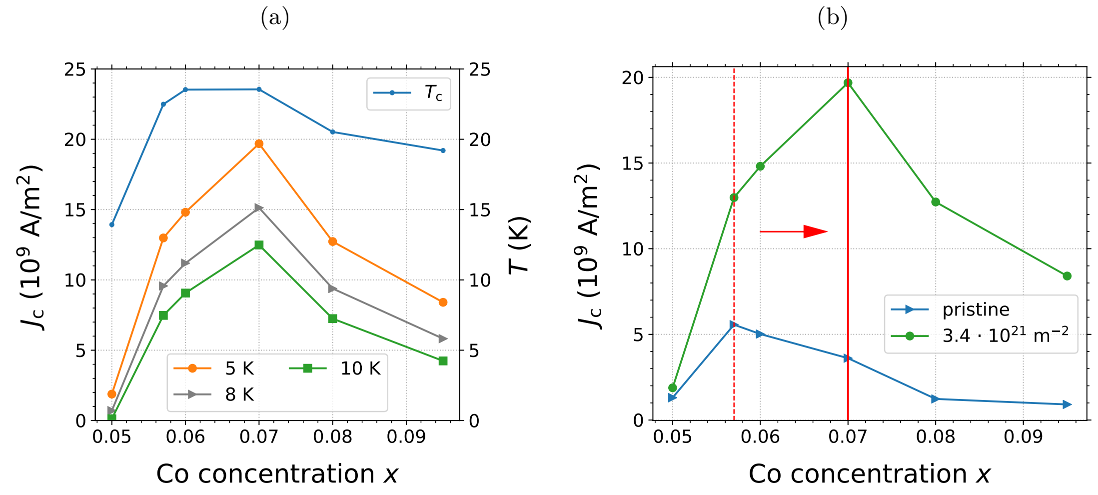

Fig. 3.3.9: Critical current density as a function of the Co concentration of the samples irradiated to a fluence of $3.4 \cdot 10^{21} \mathrm{m}^{-2}$. (a) $J_c(x)$ at 1 T and different temperatures alongside with $T_c(x)$ of the irradiated BaCo122 samples. (b) Comparison of $J_c(x)$ prior to and after the irradiation. The shift of the maximum is indicated by the red arrow.

Fig. 3.3.9(b) which shows $J_c(x)$ of the pristine and irradiated crystals at 1 T and 5 K. This figure also shows the strong J_c increase for the samples around the maximum T_c doping concentration of $x = 0.07$. The peak shifts from the under-doped region to the optimal T_c doping concentration. A similar shifting of this peak takes place in BaK122.

Chapter 4

Discussion

This chapter summarizes the change of T_c and J_c due to neutron irradiation of all doping systems and compares the different results. Furthermore, a correlation between J_c and T_c was found in the irradiated crystals which is motivated using known scaling relations in iron based superconductors. This correlation is used to calculate the doping dependence of the pinning efficiency of the pristine samples which is also discussed in this chapter.

4.1 Effect of neutron irradiation on T_c and J_c

The irradiation with neutrons introduces spherical defects through nuclear interactions or reactions in the samples [see Sec. 2.3]. These defects affect the superconducting properties of the samples. The effect on the two quantities, critical temperature and critical current density, are described in the following.

J_c is affected by the neutron irradiation through the spherical defects which act as pinning centers. These spherical pinning centers have radii in the order of the coherence length in iron based superconductors leading to efficient flux pinning. A pinning efficiency of 3-4% is reached by these defects in irradiated Ba122 [41] which is similar to values found in various compounds of the cuprate superconductors after neutron irradiation. This pinning efficiency is smaller than the maximum reachable value of approximately 32% [see Sec. 1.4 for the derivation] reached by columnar defects with the coherence length as the radius. This happens because just a

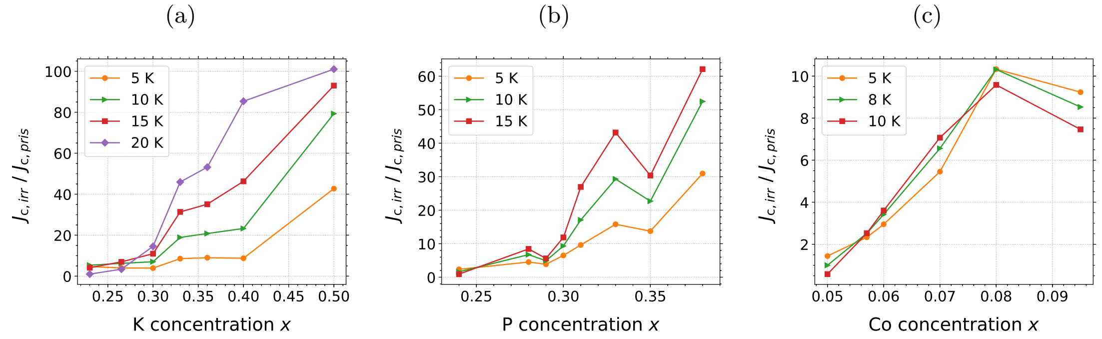
(a) (b) (c)

Fig. 4.1.1: Increase of the critical current density after irradiation ($J_{\mathrm{c},irr}/J_{\mathrm{c},pris}$) as a function of the dopant concentration at different temperatures. J_c at 1 T is used in all plots. (a) K-doped (b) P-doped (c) Co-doped samples

small fraction of the flux line is pinned by the spherical defect. Nevertheless, the pinning of the introduced defects is more efficient than the pinning of the pristine crystallographic defects. Therefore, J_c increases drastically after neutron irradiation in all three doping systems.

The J_c increase at 1 T and different temperatures is shown in Fig. 4.1.1(a), Fig. 4.1.1(b) and Fig. 4.1.1(c) for the K-doped, P-doped and Co-doped samples, respectively. The change of J_c depends strongly on the dopant concentration in one doping system, nevertheless the different doping systems behave similarly. All under-doped samples exhibit the smallest J_c increase. The samples with the smallest P and Co concentration show almost no increase of J_c [see also Fig. 3.2.8(b) and Fig. 3.3.9(b)]. The enhancement of the critical current density increases with increasing dopant concentration in all doping system. This increase is monotonic in the K-doped system for all temperatures. The Co-doped and P-doped samples show more scattering but a clear trend of an increasing enhancement with increasing dopant concentration is visible at all temperatures. The over-doped samples show the biggest increase in each doping system. However, after the irradiation a dome-like shape of $J_\mathrm{c}(x)$ is observed in all doping systems [see Fig. 3.1.10(a), Fig. 3.2.8(a) and Fig. 3.3.9(a)]. This can be explained by the smaller J_c of the over-doped pristine crystals. The increase for the optimally (regarding T_c) doped samples is smaller, but they exhibit already a high J_c in the pristine samples. Thus, they reach the maximum J_c after the irradiation.

The comparison of the increase at different temperatures shows that it is bigger for higher temperatures in the K-doped and P-doped samples and no clear difference is seen in the Co-

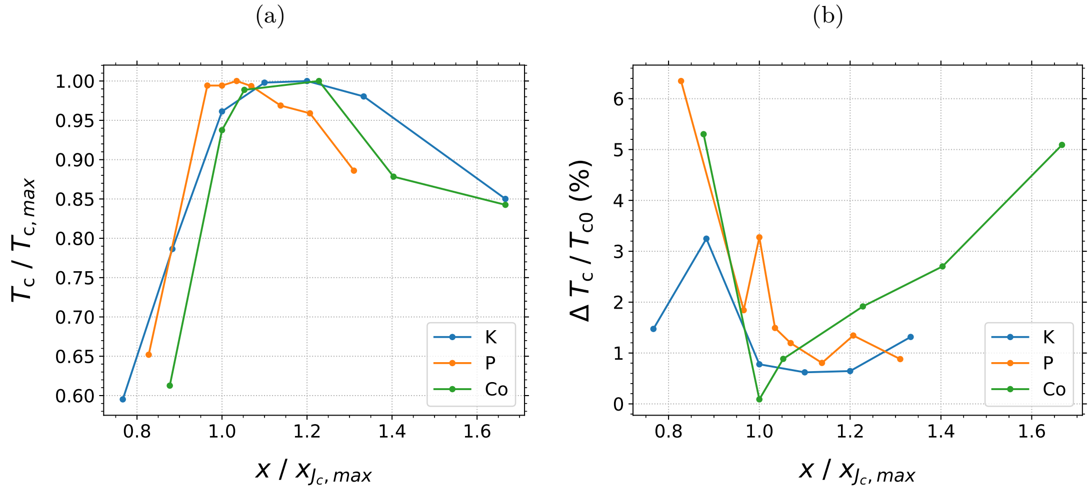

Fig. 4.1.2: Comparison of the change in critical temperature of all doping systems. (a) T_c of all doping systems normalized to its maximum value. The dopant concentration is normalized to the concentration which exhibits the maximum J_c in each pristine doping system. (b) Relative T_c reduction of all doping systems with the dopant concentration normalized as in (a)

doped samples. The latter can be associated with the already high pristine J_c of the over-doped BaCo122 samples compared to the over-doped samples in the other two systems. Therefore, the pinning is already strong in the over-doped BaCo122 samples and further pinning centers introduced by the irradiation do not increase J_c as strongly as in the other two doping systems. The pinning is weak at higher temperatures in pristine over-doped BaK122 and BaP122 which is increased by the additional defects from the neutron irradiation.

The biggest increase of J_c was found in the K-doped system although these crystals exhibit the highest pristine J_c. The maximum increase is found in the crystal with a K concentration of $x = 0.5$ at 20 K. J_c of this crystal increases by two orders of magnitude. The J_c increase is smaller in the P-doped system with a maximum increase by a factor of 60. The smallest J_c increase was found in the Co-doped system with a maximum increase by one order of magnitude.

The change of the critical temperature happens in a more indirect way as the change of J_c. The introduced defects from the neutron irradiation can affect T_c in two ways. First, these defects can change the lattice parameter of the sample due to strain in the lattice caused by the created defects. This change of the lattice parameter can be understood as internal pressure which acts like doping in Ba122 and thus changes the transition temperature. Second, the introduced defects act as scattering centers which can be pair breaking and therefore change T_c. The introduced defects are non-magnetic scattering centers which are not pair breaking in conventional single band s-wave superconductors. This is not the case for iron based superconductors because they are unconventional multi-band superconductors. These systems allow intra-band and inter-band scattering which do not preserve the energy of the particles and thus a reduction of T_c is possible [52, 53, 54, 55].

The critical temperature decreased for all investigated samples. The normalized T_c reduction is shown in Fig. 3.1.8, Fig. 3.2.6 and Fig. 3.3.6 for the K-doped, P-doped and Co-doped system, respectively. The comparison of the three doping systems is not straight forward because the dopant concentrations and T_c differ in all of them. For example, the doping where the maximum T_c is reached is 0.36 and 0.07 in the K-doped and Co-doped samples, respectively. To compare the doping systems, T_c of each doping system is normalized to its maximum and each dopant concentration is normalized to the concentration where J_c is maximal in the pristine crystals. The dopant concentration normalization is chosen because it represents a distinguished doping concentration which is speculated to coincide with the doping concentration where the antiferromagnetism vanishes in the phase diagram. The normalized $T_\mathrm{c}(x)$ curves and the normalized T_c reduction for all three doping systems is shown in Fig. 4.1.2. Plotting the doping dependence of T_c in this way [see Fig. 4.1.2(a)] makes it possible to compare the shape of $T_\mathrm{c}(x)$ of the different doping systems. The P-doped samples behave slightly different at the doping with the maximum J_c and higher doping concentrations. This different behavior could be explained by the different way of doping in the P-doped system. The K-doped and Co-doped crystals are doped with holes and electrons, respectively. The P doping is an isovalent doping where superconductivity is induced by internal pressure.

Fig. 4.1.2(b) summarizes the relative T_c reduction after the neutron irradiation of all doping systems. The dopant concentration is normalized to the dopant concentration with the maximal J_c of each doping system like in the previous $T_\mathrm{c}(x)$ plot. This comparison between the doping systems shows an in general similar behavior with slight differences. The doping dependence of $\Delta\ T_\mathrm{c}\ /\ T_\mathrm{c0}$ is shaped like the letter U. It starts from a high value at low dopant concentrations, reaches a minimum around optimal doping and increases again for higher dopant concentrations. The lowest K concentration does not follow this U-shape, but it has the lowest relative doping concentration with no comparable samples from the other doping systems. It is possible that samples with lower P and Co concentrations show a similar behavior. The over-doped area shows a similar increase in all doping systems with the Co-over-doped samples exhibiting the highest relative doping concentration and, therefore, the biggest T_c reduction in the over-doped area. Electron irradiation experiments on BaK122 have shown that the T_c reduction increases with further doping following the shape of BaCo122 [49]. The three doping systems behave differently at $x/x_{J_c,max} = 1$. The P-doped system shows a peak and, contrary, the Co-doped system exhibits a minimum at this dopant concentration. Furthermore, the K-doped system shows no significant feature at this dopant concentration.

As mentioned above, the neutron irradiation introduces impurities which act as scattering centers. The introduction of these defects make the superconducting gap more isotropic and the doping dependence of this change can be used to probe the pairing symmetry. The increase of the T_c reduction in the over-doped area could be interpreted as a change of the gap symmetry. However, probing the gap symmetry by disorder in iron based superconductors is maybe not as decisive as in cuprates and only qualitative conclusions can be drawn [56]. A comparison of the reduction in the under-doped and over-doped area is problematic because of magnetic order which is present in the under-doped area. The multiband nature of iron based superconductors makes it also very difficult to draw conclusions from T_c suppression alone because many parameters are involved in pair breaking in these systems.

4.2 Correlation between T_c and J_d

The unexpected shape of $J_\mathrm{c}(x)$ in all three doping systems is shown in Fig. 3.1.5, Fig. 3.2.5 and Fig. 3.3.5 for BaK122, BaP122 and BaCo122, respectively. This shape is significantly different from the dome-like shape of $T_\mathrm{c}(x)$ in all doping systems. After neutron irradiation, the shape of all $J_\mathrm{c}(x)$ curves changes significantly. They are shown in Fig.3.1.10(a), Fig. 3.2.8(a) and Fig. 3.3.9(a) for BaK122, BaP122 and BaCo122, respectively. The doping dependence of J_c after irradiation resembles the shape of $T_\mathrm{c}(x)$ in all doping systems. This observation rises the question if a correlation between T_c and J_c exists after irradiation. Such a correlation could be power law like, thus the critical current density and the critical temperature are plotted double

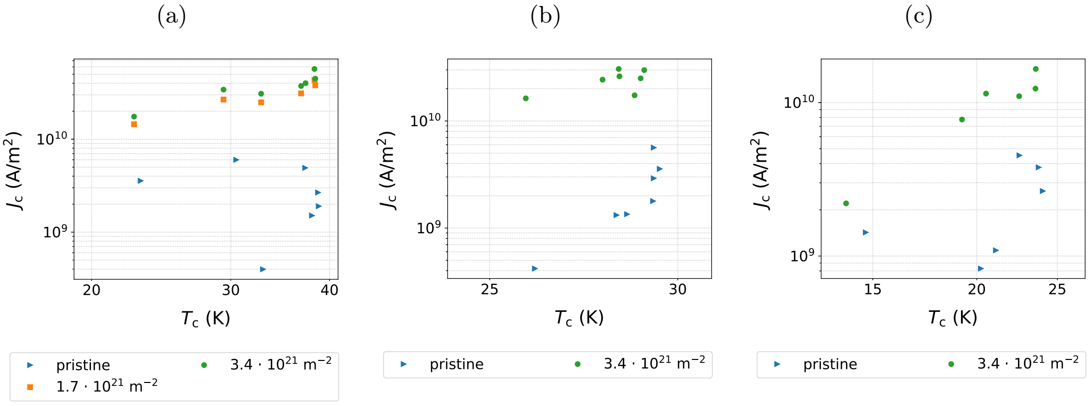

Fig. 4.2.1: J_c as a function of T_c at 1 T and $t = 0.3$ prior to and after irradiation. (a) K-doped (b) P-doped (c) Co-doped samples

logarithmically where a power law like correlation is linear. This is shown in Fig. 4.2.1 for the pristine and irradiated crystals of each doping set. The J_c values are taken at 1 T and a reduced temperature of $t = \frac{T}{T_c} = 0.3$ for better comparison. Especially, the under-doped samples exhibit a lower T_c than the optimally- and over-doped samples making a comparison at absolute temperatures problematic. The field of 1 T was chosen to eliminate the influence of different self-fields. Since the large field gradients within the samples potentially still influence the results, all evaluations were also performed for 2 T and the same behavior as at 1 T was found. Fig. 4.2.1(a) shows the K-doped samples prior to and after each irradiation step. The pristine crystals show no correlation and resemble the peak in $J_c(x)$. After irradiation, a linear correlation can be seen in the double logarithmic plot indicating a power law like correlation. This is already visible after the first irradiation step. Further irradiation results in a similar increase of J_c with respect to the previous irradiation for all crystals. The change from no correlation in the pristine crystals to a power law like correlation in the irradiated crystals is also observed in BaP122 and BaCo122 which is shown in Fig. 4.2.1(b) and Fig. 4.2.1(c), respectively.

The critical current density can be written as a product of pinning efficiency and depairing current density [see Eq. 1.4.1]. The depairing current density is the more promising parameter of these two to find a connection to the critical temperature. J_d is a function of the magnetic penetration depth and the coherence length [see Eq. 1.3.5] and can be re-written using the definition of the thermodynamic critical field, B_c [Eq. 1.2.7], as

$$J_\mathrm{d} \propto \frac{B_\mathrm{c}}{\lambda} \,. \tag{4.2.1}$$

These two parameters are further related to T_c by power laws as reported in literature. The Uemura relation [see Sec. 1.5] determines the dependence for λ which is $\frac{1}{\lambda} \propto T_\mathrm{c}^{0.5}$. The relation for B_c was extracted from thermal capacity measurements and found to be $B_\mathrm{c} \propto T_\mathrm{c}^{1.75}$ [57, 58]. These two relations combined result in a power law like correlation between the depairing current density and the critical temperature:

$$J_\mathrm{d} \propto T_\mathrm{c}^{2.25} \,. \tag{4.2.2}$$

This correlation between the depairing current density and the critical temperature is true for the pristine and for the irradiated crystals, but J_d is not measured directly. The measured quantity is J_c which is connected to J_d via the pinning efficiency. After neutron irradiation, a defect landscape is introduced which is more efficient for flux pinning than the defects of the pristine crystals. Since the radiation induced defect structure is essentially the same in all crystals a constant pinning efficiency governed by the introduced defects is assumed. Hence, J_c is directly proportional to J_d with the same proportionality factor for all samples and therefore also to $T_\mathrm{c}^{2.25}$. The pinning efficiency in the pristine crystals is expected to vary between different dopant concentrations because of the dopant atoms introduced in the lattice. Thus, the correlation between J_d and T_c can not be seen by measuring J_c because the pinning efficiency could vary between different dopant concentrations. This can already be seen in Fig. 4.2.1 and is summarized in Fig. 4.2.2 where J_c of the irradiated samples as a function of T_c is shown for all doping systems in one plot.

The red line in Fig. 4.2.2 is a fit of $J_\mathrm{c} = k \cdot T_\mathrm{c}^{2.25}$ to the experimental data of the irradiated samples with k as the only fit parameter. The exponent was fixed to the value predicted above [see Eq. 4.2.2]. The data points follow this prediction except the samples with the lowest P and Co concentration. It was previously shown that the coherence length depends on the dopant concentration in Ba122 [32]. The two samples not following the correlation are the only investigated samples with a coherence length above 3 nm. If the coherence length is bigger than the size of

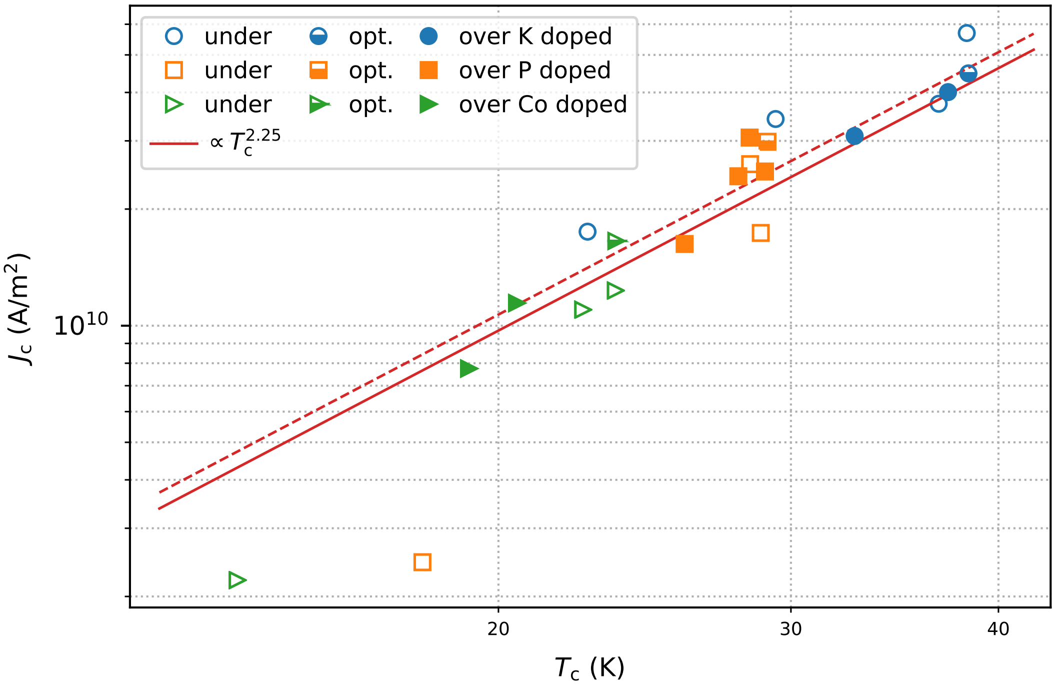

Fig. 4.2.2: Correlation between J_c and T_c at 1 T and $t = 0.3$ for the K-doped, P-doped and Co-doped samples. The open, half-filled and filled symbols indicate under, optimally and over-doped samples, respectively. The solid red line is a fit to all measured data points with the predicted power law: $J_c = k \cdot T_c^{2.25}$. The dashed red line is a fit to the data-set excluding the two samples with the lowest T_c.

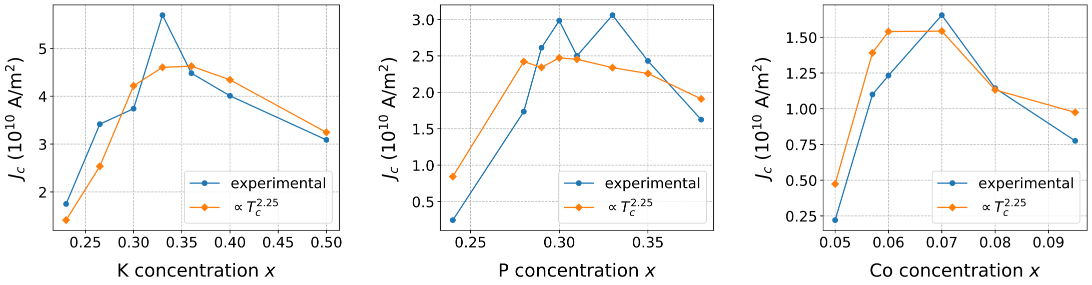

(a) (b) (c)

Fig. 4.2.3: Calculated ($\propto T_c^{2.25}$) and measured critical current density at 1 T and $t = 0.3$ of the irradiated samples as a function of the dopant concentration. The function to calculate J_c was obtained by a fit to the experimental data of all three doping systems combined and excluding the two samples with the lowest T_c(dashed red line in Fig. 4.2.2 and explanation in the text) (a) BaK122 (b) BaP122 (c) BaCo122

the introduced defects not the whole flux line core can save the condensation energy. Thus, the pinning is weaker and the increase of J_c by the introduced defects is smaller. A similar behavior was found in MgB_2 after neutron irradiation where the increase of J_c was smaller as expected because of the big coherence length of 12 nm compared to the defect size of approximately 5 nm [59].

As mentioned above, the two samples with the lowest T_c seem not to follow the expected behavior, therefore, they are excluded in the fit used for further calculations. This fit is shown in Fig. 4.2.2 as a dashed line and yields the coefficient of the function $J_c = k \cdot T_c^{2.25}$. It can be used to calculate J_c from the measured values of T_c which is shown together with the experimental values in Fig. 4.2.3 for all doping systems. The comparison of the measured and calculated $J_c(x)$ can show differences and similarities at certain doping ranges. Fig. 4.2.3(a) shows the data of BaK122 where the calculated values closely follow the experimental $J_c(x)$ curve except for the sample with a potassium concentration $x = 0.33$. This dopant concentration is in the area close to the maximum of T_c where $T_c(x)$ is very flat. The peak is not only present at low temperatures but preserved at all measured temperatures which is shown in Fig. 3.1.10.

The measured and calculated $J_c(x)$ of BaP122 is shown in Fig. 4.2.3(b). The general agreement between the two curves is not as good as in BaK122 but the calculated values reproduce the dome shape of the experimental data. Around the maximum of T_c the scattering of the measured values is biggest. This is the area where in BaK122 a peak in $J_c(x)$ is visible. Here, no clear peak is visible, but regarding the problems with the sample with phosphorous concentration $x = 0.31$ [see Sec. 3.2.2] this is not totally clear.

Fig. 4.2.3(c) compares the calculated and measured $J_\mathrm{c}(x)$ of BaCo122. The situation in this doping system is comparable to BaK122. The calculated values closely follow the experimental data but no clear peak is visible in the experimental values. The scattering of the measured J_c values around the calculated ones seem also to be bigger in this system compared to BaK122.

All three investigated doping systems show a general agreement between calculated and measured values in $J_\mathrm{c}(x)$. Around the doping concentration with maximum T_c the difference is biggest. BaK122 exhibits a peak in the measured $J_\mathrm{c}(x)$. BaP122 shows no clear peak but the measured J_c values are higher than the calculated ones in the area with maximum T_c. BaCo122 follows the calculated values and no clear peak is present. It is not clear at the moment if the peak in BaK122 can be considered as a normal sample-to-sample variation as seen in the other doping systems or an indication of physics beyond this model.

4.3 Pinning efficiency

The basic assumption for the irradiation experiments is the constant pinning efficiency of all samples after the irradiation which is indicated by the red line in Fig. 4.2.2. This constant pinning efficiency, η_irr, was calculated for the K doped crystal with $x = 0.4$ because the required parameters are reported in literature. The first step is the calculation of the depairing current density [see Eq. 1.3.5] using the superconducting coherence length, $\xi = 1.4\,\mathrm{nm}$ [32], and the magnetic penetration depth, $\lambda = 230\,\mathrm{nm}$ [60], which leads to $J_\mathrm{d} = 13.6 \cdot 10^{11}\ \mathrm{A/m^2}$. After that, the pinning efficiency can be calculated with $\eta_\mathrm{irr} = \frac{J_\mathrm{c}}{J_\mathrm{d}}$ where J_c is the critical current density of the crystal with K concentration $x = 0.4$ after the last irradiation step. The resulting pinning efficiency is 3.2%. This pinning efficiency is assumed to be the same for all the samples after neutron irradiation which is similar to pinning efficiencies found in various compounds of the cuprate superconductors after neutron irradiation.

Fig. 4.2.1 shows that the correlation between J_c and T_c does not hold for the pristine doping sets. This is a consequence of a pinning efficiency which depends on the dopant concentration in the pristine crystals. The pinning efficiency is the quotient of critical current density and

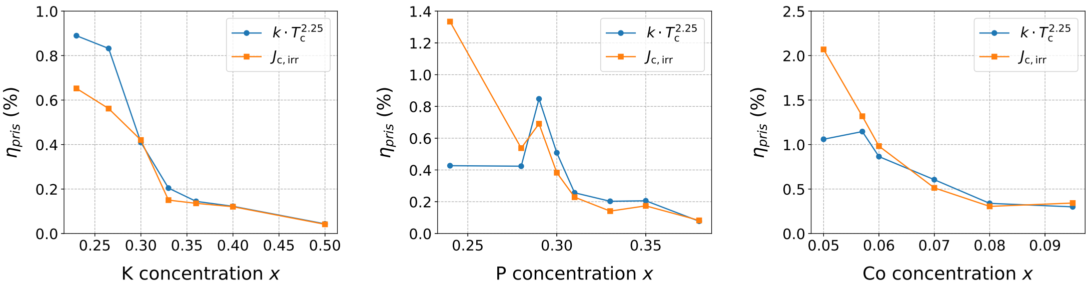
(a) (b) (c)

Fig. 4.3.1: Doping dependence of the pinning efficiency of the pristine crystals, η_{pris}, calculated in two different ways. First, by using the correlation between T_c and J_c entitled with $k \cdot T_\text{c}^{2.25}$. Second, using the critical current density of the irradiated crystals entitled with $J_{\text{c,irr}}$. Both approaches use the constant pinning efficiency of the irradiated samples which was calculated using literature values for the sample with K concentration $x = 0.4$. (a) samples doped with K (b) samples doped with P (c) samples doped with Co

depairing current density as can be seen in the definition of J_c: Eq. 1.4.1. The critical current density of the pristine crystals was measured, therefore, the depairing current density needs to be assessed to calculate the pinning efficiency. This can be done in two different ways. First, the measured J_c of the irradiated crystals together with η_{irr} can be used to calculate J_d. This leads to:

$$\eta_{\text{pris}} = \frac{\eta_{\text{irr}} \cdot J_{\text{c,pris}}}{J_{\text{c,irr}}} \ . \tag{4.3.1}$$

Second, the established power law can be used to calculate $J_{\text{c,irr}}$ using the measured T_c which leads to:

$$\eta_{\text{pris}} = \frac{\eta_{\text{irr}} \cdot J_{\text{c,pris}}}{k \cdot T_\text{c}^{2.25}} \ . \tag{4.3.2}$$

The doping dependence of η_{pris} calculated with the above described approaches is shown in Fig. 4.3.1 for all three doping systems. The two calculation methods agree for the optimally- and over-doped samples in all three doping systems. However, the resulting pinning efficiencies of the under-doped samples differ between the two methods. The difference is big for BaP122 and BaCo122, especially for the samples with the smallest dopant concentration. These are the two points in Fig. 4.2.2 with the biggest difference between the power law and the measured J_c values which could be attributed to a mismatch between coherence length and defect size as mentioned earlier. Hence, the pinning efficiency resulting from the measured value [Eq. 4.3.1] is

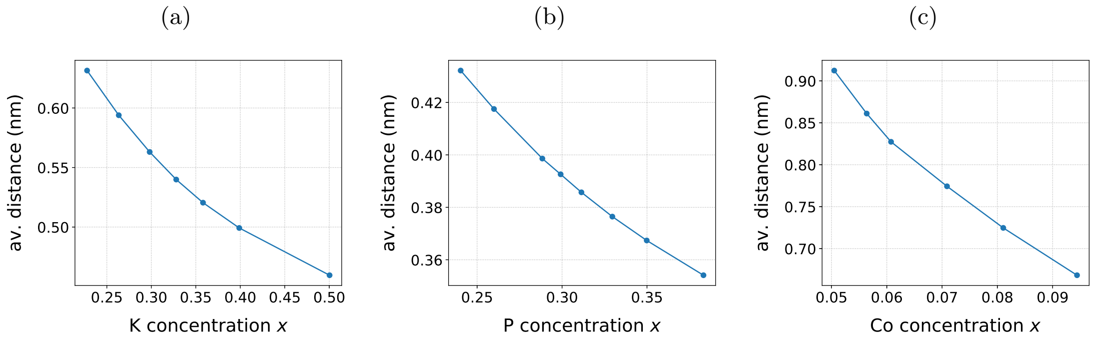

Fig. 4.3.2: Calculated average distance between randomly distributed doping atoms in a plane. A quadratic lattice with a lattice parameter of 0.4 nm, 0.28 nm and 0.28 nm was used as approximation for BaK122, BaP122 and BaCo122, respectively. (a) BaK122 (b) BaP122 (c) BaCo122

an overestimation and the pinning efficiencies resulting from the power law [Eq. 4.3.2] yield the more accurate value in the under-doped area. The difference between the calculation methods in general is smaller in BaK122, but it is also biggest in the under-doped area where the power law yields a bigger pinning efficiency than the measured J_c values.

The values of the pinning efficiencies are comparable in the over-doped areas and show differences in the optimally- and under-doped areas of all doping systems. The biggest pinning efficiency at optimal doping was found in BaCo122 which agrees with the small increase of J_c upon neutron irradiation in this doping system [see Fig. 4.1.1]. The pristine defects in BaCo122 are already efficient pinning centers, therefore, further defects do not increase J_c as much as in the other two systems where the pristine defects are not as efficient for flux pinning. Moreover, the pinning efficiencies in BaK122 and BaP122 are comparable which can also be seen in a similar increase of J_c after neutron irradiation [see Fig. 4.1.1]. BaP122 is the only doping system where the peak in $J_c(x)$ [see Fig. 3.2.5] is also visible in the pinning efficiency, Fig. 4.3.1(b), as a peak at $x = 0.29$. This peak is more pronounced when using the power law to calculate the pinning efficiency.

The pinning efficiencies show a similar decrease with increasing dopant concentration in all doping systems except the peak in BaP122. This could be a hint that the doping atoms themselves act as pinning centers. To examine this conception, the average distance between randomly distributed doping atoms was calculated. This calculation was done in two dimensions because the flux lines are aligned perpendicular to the ab-plane in the used measurement methods and only the distances in this plane are of interest. The doping dependence of the average distance as a function of dopant concentration using a lattice parameter of 0.4 nm is shown in Fig. 4.3.2. This plot shows a decrease of the average distance with increasing dopant concentration in all three doping systems which looks similar to the pinning efficiency in Fig. 4.3.1. However, the maximum average distance of 0.9 nm reached in BaCo122 is approximately one third of the coherence length in this material. Therefore, the individual doping atoms themselves cannot act as point pinning centers because they are too close together also in the under-doped range with a smaller dopant concentration. Thus, not the doping atoms but rather their fluctuations which could happen on length scales bigger than the average distance between the doping atoms could act as pinning centers. Such fluctuations would lead to areas with different doping concentrations and thus different T_c in the crystal. This spacial T_c variation could than be responsible for the flux pinning. It was previously shown that $\frac{\partial T_c}{\partial x}$ is largest in under-doped Ba122 [32] which could explain the larger pinning efficiency in this doping range. Furthermore, the calculations used randomly distributed doping atoms which does not take clustering of these atoms into account. This could happen in the under-doped samples and result in a bigger distance between the resulting clusters.

The under-doped range of all three doping systems have a magnetic and structural phase transition in common. This is a transition from a paramagnetic-tetragonal phase at high temperatures to an antiferromagnetic-orthorombic phase at low temperatures [see Sec. 2.1] [11]. The orthorombic phase transition results in the formation of twin domains with an alternating a- and b-axis orientation. These twin boundaries where previously discussed to act as pinning centers [35] which could explain the enhanced pinning efficiency in the under-doped area. However, a previous study on BaCo122 showed that the peak in $J_c(x)$ did not disappear after detwinning the samples by applying uniaxial pressure [61]. The peak in $J_c(x)$ is a direct consequence of the enhanced pinning efficiency and, thus, if the twin boundaries were the reason for the enhanced pinning efficiency in the under-doped area the peak in $J_c(x)$ should disappear after detwinning. However, it is not absolutely clear if the sample was detwinned completely and all twin boundaries were removed.

Another similarity of the under-doped range is the presence of the antiferromagnetic phase. Evidence has been found for microscopic coexistance of magnetism and superconductivity in

BaP122 using muon spin rotation and infrared spectroscopy [12]. This coexistance could play a role in vortex pinning. Therefore two different scenarios (and with that doping ranges) have to be taken into account. The first doping range is the area where the critical temperature for superconductivity, T_c, is higher than the Néel temperature of the antiferromagnetically ordered phase, T_N. This is a small doping range with lower dopant concentration than the doping concentration where maximum T_c is reached. Hence, the superconducting transition happens at higher temperatures than the magnetic ordering. Therefore, flux lines are present in the material before the magnetic transition happens. The magnetic ordering in the superconductor could happen just in and around the flux lines where the order parameter is zero or small. This would result in a small antiferromagnetic area with a net magnetic moment at the position of the flux lines which could enhance the pinning by electromagnetic interaction. The doping range where this could happen is also the range where the peak in $J_\mathrm{c}(x)$ appears in BaK122 and BaCo122. The second doping range is the area where T_N is higher than T_c. This is the range from the doping concentration where superconductivity emerges to the point where T_N and $T_\mathrm{c}(x)$ cross each other in the phase diagram. Thus, the magnetic ordering takes place at higher temperatures than the superconducting transition. Therefore, magnetic ordering is already present when the superconducting phase emerges. This could result in a microscopic coexistance of these two phases which could act as pinning centers. These pinning centers are not as efficient as the pinning centers in the first doping area, which can be seen in a decrease or flattening of $\eta(x)$ calculated via the power law in the under-doped range in Fig. 4.3.1. Furthermore, quantum criticality could play a role in the under-doped area which could enhance the energy of flux lines near a possible quantum critical point [62]. The peak in the pinning efficiency of BaP122 [see Fig. 4.3.1(b)] could be an indication of such a phenomena.

Chapter 5

Conclusion and Outlook

A detailed study of the doping dependence of the critical temperature and critical current density was carried out in three different doping systems of the iron based superconductor Ba122. Therefore, single crystals of Ba122 doped with potassium, phosphorous and cobalt were investigated. Their doping concentrations, including under-, optimally- and over-doped samples, were chosen to cover a big part of the superconducting dome. J_c in the pristine crystals showed an unexpected doping dependence which is different from the doping dependence of T_c in all doping systems. To understand this difference, neutron irradiation was performed which is known to introduce defects more efficient for flux pinning than the pristine crystallographic defects. The experiments were performed on the same sample set prior to and after neutron irradiation to reduce sample-to-sample variations and to be sure that the measured differences originate from the neutron irradiation. It was shown that J_c increased vastly in all samples independent of the doping system, whereas, the T_c decrease was small. Moreover, the doping dependence of J_c changed in all doping systems due to the neutron irradiation. The irradiated crystals showed a more dome like shape of $J_\mathrm{c}(x)$ which was more similar to $T_\mathrm{c}(x)$ than in the pristine samples. This indication led to the discovery of a power law correlation between J_c and T_c in all irradiated samples. The correlation seems to be universal for Ba122. The outliers were explained by a mismatch of the coherence lengths and the defect sizes. The correlation was explained by a correlation between the depairing current density and T_c resulting from the Uemura relation and a correlation between the thermodynamic critical field and T_c found experimentally. The constant pinning efficiency of all irradiated crystals made it possible to assess this correlation by measuring J_c. The correlation between J_d and T_c holds also true for the pristine samples hence the pinning efficiency has to vary between dopant concentrations to explain the doping dependence of J_c. The pinning efficiency of the pristine samples which depends on the dopant concentration was calculated using the power law and the constant pinning efficiency of the irradiated samples. The result showed the highest pinning efficiencies in the under-doped range of all doping systems. Furthermore, a peak in the pinning efficiency of BaP122 was found. The largest pinning efficiency lies in the region where the antiferromagnetic-orthorombic phase is present in the phase diagram. It is speculated that the proximity of superconductivity and antiferromagnetism or the fluctuations of the doping atoms are a reason for the large pinning efficiency. However, further experiments are needed to understand the underlying physics responsible for pinning in these materials.

The discovered power law between J_c and T_c in the irradiated samples seems to be universal for Ba122 but it is not clear yet if it is also true in other high temperature superconductors. The power law relies on the Uemura relation which was first discovered in the cuprates. Therefore, it would be very interesting to investigate irradiated cuprates with different T_c and check if the same power law is found. It is not clear at present how the correlation between B_c and T_c looks like in cuprates. Thus, the power law between J_c and T_c could have an exponent which depends on the type of high temperature superconductor. A correlation which is true for different high temperature superconductors could lead to a better understanding of high temperature superconductivity.

A continuation of the findings in this thesis would be the investigation of samples with smaller dopant concentrations than the ones used in this thesis. This could help to understand the universality of the correlation between J_c and T_c of the irradiated crystals and the doping dependence of the pinning efficiency in the pristine crystals. Furthermore, the investigation of the small peak in $J_\mathrm{c}(x)$ in BaK122 after neutron irradiation could help to understand if it is just sample-to-sample variation or physics beyond this model.

Bibliography

[1] J. G. Bednorz and K. A. Müller, “Possible highT_c superconductivity in the Ba-La-Cu-O system,” *Zeitschrift für Physik B Condensed Matter*, vol. 64, pp. 189–193, June 1986.

[2] Y. Kamihara, T. Watanabe, M. Hirano, and H. Hosono, “Iron-based layered superconductor La[$O_{1-x}F_x$]FeAs (x= 0.05-0.12) with $T_c = 26$ K,” *Journal of the American Chemical Society*, vol. 130, pp. 3296–3297, Mar. 2008.

[3] X. Wang, Q. Liu, Y. Lv, W. Gao, L. Yang, R. Yu, F. Li, and C. Jin, “The superconductivity at 18 K in LiFeAs system,” *Solid State Communications*, vol. 148, pp. 538–540, Dec. 2008.

[4] F.-C. Hsu, J.-Y. Luo, K.-W. Yeh, T.-K. Chen, T.-W. Huang, P. M. Wu, Y.-C. Lee, Y.-L. Huang, Y.-Y. Chu, D.-C. Yan, and M.-K. Wu, “Superconductivity in the PbO-type structure-FeSe,” *Proceedings of the National Academy of Sciences*, vol. 105, pp. 14262–14264, Sept. 2008.

[5] M. Rotter, M. Tegel, and D. Johrendt, “Superconductivity at 38 K in the iron arsenide $(Ba_{1-x}K_x)Fe_2As_2$,” *Physical Review Letters*, vol. 101, Sept. 2008.

[6] A. Iyo, K. Kawashima, T. Kinjo, T. Nishio, S. Ishida, H. Fujihisa, Y. Gotoh, K. Kihou, H. Eisaki, and Y. Yoshida, “New-structure-type Fe-based superconductors: $CaAFe_4As_4$ (A = K, Rb, Cs) and $SrAFe_4As_4$ (A = Rb, Cs),” *Journal of the American Chemical Society*, vol. 138, pp. 3410–3415, Mar. 2016.

[7] K. Kawashima, T. Kinjo, T. Nishio, S. Ishida, H. Fujihisa, Y. Gotoh, K. Kihou, H. Eisaki, Y. Yoshida, and A. Iyo, “Superconductivity in fe-based compound $EuAFe_4As_4$ (A = Rb and Cs),” *Journal of the Physical Society of Japan*, vol. 85, p. 064710, June 2016.

[8] H. Hosono, A. Yamamoto, H. Hiramatsu, and Y. Ma, “Recent advances in iron-based superconductors toward applications,” *Materials Today*, vol. 21, pp. 278–302, Apr. 2018.

[9] M. Eisterer, “Predicting critical currents in grain-boundary limited superconductors,” *Physical Review B*, vol. 99, Mar. 2019.

[10] Z.-A. Ren, G.-C. Che, X.-L. Dong, J. Yang, W. Lu, W. Yi, X.-L. Shen, Z.-C. Li, L.-L. Sun, F. Zhou, and Z.-X. Zhao, “Superconductivity and phase diagram in iron-based arsenic-oxides $\mathrm{ReFeAsO}_{1-\delta}$ (Re = rare-earth metal) without fluorine doping,” *EPL (Europhysics Letters)*, vol. 83, p. 17002, June 2008.

[11] G. R. Stewart, “Superconductivity in iron compounds,” *Reviews of Modern Physics*, vol. 83, pp. 1589–1652, Dec. 2011.

[12] B. P. P. Mallett, C. N. Wang, P. Marsik, E. Sheveleva, M. Yazdi-Rizi, J. L. Tallon, P. Adelmann, T. Wolf, and C. Bernhard, “Muon spin rotation and infrared spectroscopy study of magnetism and superconductivity in $\mathrm{Ba}_{1-x}\mathrm{K}_x\mathrm{Fe}_2\mathrm{As}_2$,” *Phys. Rev. B*, vol. 95, p. 054512, Feb 2017.

[13] J. Hänisch, K. Iida, R. Hühne, and C. Tarantini, “Fe-based superconducting thin films-preparation and tuning of superconducting properties,” *Superconductor Science and Technology*, vol. 32, p. 093001, Aug. 2019.

[14] Y. Ma, “Progress in wire fabrication of iron-based superconductors,” *Superconductor Science and Technology*, vol. 25, p. 113001, Sept. 2012.

[15] F. London and H. London, “The electromagnetic equations of the supraconductor,” *Proceedings of the Royal Society of London. Series A - Mathematical and Physical Sciences*, vol. 149, pp. 71–88, Mar. 1935.

[16] L. Landau, “Zur theorie der phasenumwandlungen ii,” *Phys. Z. Sowjetunion*, vol. 11, no. 545, pp. 26–35, 1937.

[17] L. D. Landau and V. Ginzburg, “On the theory of superconductivity,” *Zh. Eksp. Teor. Fiz.*, vol. 20, p. 1064, 1950.

[18] A. A. Abrikosov, "An influence of the size on the critical field for type ii superconductors," *Dokl. Akad. Nauk SSSR*, vol. 86, p. 489, 1952.

[19] A. A. Abrikosov, "Nobel lecture: Type-II superconductors and the vortex lattice," *Reviews of Modern Physics*, vol. 76, pp. 975–979, Dec. 2004.

[20] W. Buckel and R. Kleiner, *Superconductivity: fundamentals and applications.* John Wiley & Sons, 2008.

[21] A. A. Abrikosov, "On the magnetic properties of superconductors of the second group," *Sov. Phys. JETP*, vol. 5, pp. 1174–1182, 1957.

[22] J. Bardeen, "Critical fields and currents in superconductors," *Reviews of Modern Physics*, vol. 34, pp. 667–681, Oct. 1962.

[23] M. Eisterer, "Radiation effects on iron-based superconductors," *Superconductor Science and Technology*, vol. 31, p. 013001, Dec. 2017.

[24] A. Glatz, I. A. Sadovskyy, U. Welp, W.-K. Kwok, and G. W. Crabtree, "The quest for high critical current in applied high-temperature superconductors," *Journal of Superconductivity and Novel Magnetism*, vol. 33, pp. 127–141, Sept. 2019.

[25] Y. Uemura, G. Luke, B. Sternlieb, J. Brewer, J. Carolan, W. Hardy, R. Kadono, J. Kempton, R. Kiefl, S. Kreitzman, *et al.*, "Universal correlations between T_c and n_s/m^* (carrier density over effective mass) in High-T_c cuprate superconductors," *Physical review letters*, vol. 62, no. 19, p. 2317, 1989.

[26] I. Božović, X. He, J. Wu, and A. T. Bollinger, "Dependence of the critical temperature in overdoped copper oxides on superfluid density," *Nature*, vol. 536, pp. 309–311, Aug. 2016.

[27] Y. Uemura, "Energy-scale phenomenology and pairing via resonant spin–charge motion in FeAs, CuO, heavy-fermion and other exotic superconductors," *Physica B: Condensed Matter*, vol. 404, pp. 3195–3201, Oct. 2009.

[28] T. J. Williams, A. A. Aczel, E. Baggio-Saitovitch, S. L. Bud'ko, P. C. Canfield, J. P. Carlo, T. Goko, H. Kageyama, A. Kitada, J. Munevar, N. Ni, S. R. Saha, K. Kirschenbaum,

J. Paglione, D. R. Sanchez-Candela, Y. J. Uemura, and G. M. Luke, “Superfluid density and field-induced magnetism in Ba($Fe_{1-x}Co_x$)$_2$As$_2$ and Sr($Fe_{1-x}Co_x$)$_2$As$_2$ measured with muon spin relaxation,” *Physical Review B*, vol. 82, Sept. 2010.

[29] J. P. Carlo, Y. J. Uemura, T. Goko, G. J. MacDougall, J. A. Rodriguez, W. Yu, G. M. Luke, P. Dai, N. Shannon, S. Miyasaka, S. Suzuki, S. Tajima, G. F. Chen, W. Z. Hu, J. L. Luo, and N. L. Wang, “Static magnetic order and superfluid density of RFeAs(O, F)(R=La, Nd, Ce) and LaFePO studied by muon spin relaxation: Unusual similarities with the behavior of cuprate superconductors,” *Physical Review Letters*, vol. 102, Feb. 2009.

[30] C. C. Homes, S. V. Dordevic, M. Strongin, D. A. Bonn, R. Liang, W. N. Hardy, S. Komiya, Y. Ando, G. Yu, N. Kaneko, X. Zhao, M. Greven, D. N. Basov, and T. Timusk, “A universal scaling relation in high-temperature superconductors,” *Nature*, vol. 430, pp. 539–541, July 2004.

[31] Y. J. Uemura, *Muon spin relaxation studies of unconventional superconductors: First-Order behavior and comparable Spin-Charge energy scales.* Springer, 2015.

[32] S. Ishida, D. Song, H. Ogino, A. Iyo, H. Eisaki, M. Nakajima, J. Shimoyama, and M. Eisterer, “Doping-dependent critical current properties in K, Co, and P-doped $BaFe_2As_2$ single crystals,” *Phys. Rev. B*, vol. 95, p. 014517, Jan 2017.

[33] D. Song, S. Ishida, A. Iyo, M. Nakajima, J. Shimoyama, M. Eisterer, and H. Eisaki, “Distinct doping dependence of critical temperature and critical current density in $Ba_{1-x}K_xFe_2As_2$ superconductor,” *Sci. Rep.*, vol. 6, p. 26671, May 2016.

[34] S. Demirdiş, Y. Fasano, S. Kasahara, T. Terashima, T. Shibauchi, Y. Matsuda, M. Konczykowski, H. Pastoriza, and C. J. van der Beek, “Disorder, critical currents, and vortex pinning energies in isovalently substituted bafe$_2$(as$_{1-x}$p$_x$)$_2$,” *Phys. Rev. B*, vol. 87, p. 094506, Mar 2013.

[35] R. Prozorov, M. A. Tanatar, N. Ni, A. Kreyssig, S. Nandi, S. L. Bud’ko, A. I. Goldman, and P. C. Canfield, “Intrinsic pinning on structural domains in underdoped single crystals of Ba($Fe_{1-x}Co_x$)$_2$As$_2$,” *Phys. Rev. B*, vol. 80, p. 174517, Nov 2009.

[36] J. Paglione and R. L. Greene, “High-temperature superconductivity in iron-based materials,” *Nature Physics*, vol. 6, pp. 645–658, Aug. 2010.

[37] K. Kihou, T. Saito, K. Fujita, S. Ishida, M. Nakajima, K. Horigane, H. Fukazawa, Y. Kohori, S. Uchida, J. Akimitsu, A. Iyo, C.-H. Lee, and H. Eisaki, “Single-Crystal Growth of $Ba_{1-x}K_xFe_2As_2$ by KAs Self-Flux Method,” *Journal of the Physical Society of Japan*, vol. 85, p. 034718, Mar 2016.

[38] M. Nakajima, S. Ishida, K. Kihou, Y. Tomioka, T. Ito, Y. Yoshida, C. H. Lee, H. Kito, A. Iyo, H. Eisaki, K. M. Kojima, and S. Uchida, “Evolution of the optical spectrum with doping in $Ba(Fe_{1-x}Co_x)_2As_2$,” *Physical Review B*, vol. 81, Mar. 2010.

[39] M. Nakajima, S. ichi Uchida, K. Kihou, C.-H. Lee, A. Iyo, and H. Eisaki, “Growth of $BaFe_2(As_{1-x}P_x)_2$ single crystals ($0 \leq x \leq 1$) by Ba_2As_3/Ba_2P_3-flux method,” *Journal of the Physical Society of Japan*, vol. 81, p. 104710, Oct. 2012.

[40] C. P. Bean, “Magnetization of high-field superconductors,” *Reviews of Modern Physics*, vol. 36, pp. 31–39, Jan. 1964.

[41] V. Mishev, M. Nakajima, H. Eisaki, and M. Eisterer, “Effects of introducing isotropic artificial defects on the superconducting properties of differently doped Ba-122 based single crystals,” *Scientific Reports*, vol. 6, June 2016.

[42] M. Zehetmayer, “Simulation of the current dynamics in superconductors: Application to magnetometry measurements,” *Physical Review B*, vol. 80, Sept. 2009.

[43] J. Clarke and A. I. Braginski, eds., *The SQUID Handbook*. Wiley, Aug. 2006.

[44] M. Frischherz, M. Kirk, J. Farmer, L. Greenwood, and H. Weber, “Defect cascades produced by neutron irradiation in $YBa_2Cu_3O_7$,” *Physica C: Superconductivity*, vol. 232, pp. 309–327, Nov. 1994.

[45] M. Aleksa, P. Pongratz, O. Eibl, F. Sauerzopf, H. Weber, T. Li, and P. Kes, “TEM observation of neutron-induced collision cascades in Bi-2212 single crystals,” *Physica C: Superconductivity*, vol. 297, pp. 171–175, Mar. 1998.

[46] T. Yano, M. Pekala, A. He, A. Wisniewski, and M. Jenkins, "Microstructural obserations on neutron-irradiated $YBa_2Cu_4O_8$ superconductor," *Physica C: Superconductivity*, vol. 247, pp. 55–61, May 1995.

[47] M. Zehetmayer, M. Eisterer, J. Jun, S. M. Kazakov, J. Karpinski, B. Birajdar, O. Eibl, and H. W. Weber, "Fishtail effect in neutron-irradiated superconducting MgB_2 single crystals," *Physical Review B*, vol. 69, Feb. 2004.

[48] D. Kagerbauer, S. Ishida, V. Mishev, D. Song, H. Ogino, H. Eisaki, M. Nakajima, A. Iyo, and M. Eisterer, "Doping dependence of the pinning efficiency in K-doped Ba122 single crystals prior to and after fast neutron irradiation," *Superconductor Science and Technology*, vol. 32, p. 094004, July 2019.

[49] K. Cho, M. Kończykowski, S. Teknowijoyo, M. A. Tanatar, Y. Liu, T. A. Lograsso, W. E. Straszheim, V. Mishra, S. Maiti, P. J. Hirschfeld, and R. Prozorov, "Energy gap evolution across the superconductivity dome in single crystals of $(Ba_{1-x}K_x)Fe_2As_2$," *Science Advances*, vol. 2, no. 9, 2016.

[50] V. Mishev, *Studying flux pinning phenomena in BaFe2As2 based superconducting single crystals and single crystalline thin films.* Wien, Techn. Univ., Diss., 2015.

[51] K. Hashimoto, K. Cho, T. Shibauchi, S. Kasahara, Y. Mizukami, R. Katsumata, Y. Tsuruhara, T. Terashima, H. Ikeda, M. A. Tanatar, H. Kitano, N. Salovich, R. W. Giannetta, P. Walmsley, A. Carrington, R. Prozorov, and Y. Matsuda, "A sharp peak of the zero-temperature penetration depth at optimal composition in $BaFe_2(As_{1-x}P_x)_2$," *Science*, vol. 336, pp. 1554–1557, Jun 2012.

[52] V. G. Kogan and R. Prozorov, "Interband coupling and nonmagnetic interband scattering in ±s superconductors," *Physical Review B*, vol. 93, June 2016.

[53] D. V. Efremov, M. M. Korshunov, O. V. Dolgov, A. A. Golubov, and P. J. Hirschfeld, "Disorder-induced transition between $s_\pm$ and s_{++} states in two-band superconductors," *Physical Review B*, vol. 84, Nov. 2011.

[54] Y. Wang, A. Kreisel, P. J. Hirschfeld, and V. Mishra, “Using controlled disorder to distinguish $s_\pm$ and s_{++} gap structure in Fe-based superconductors,” *Physical Review B*, vol. 87, Mar. 2013.

[55] Y. Bang, H.-Y. Choi, and H. Won, “Impurity effects on the ±s-wave state of the iron-based superconductors,” *Physical Review B*, vol. 79, Feb. 2009.

[56] P. J. Hirschfeld, M. M. Korshunov, and I. I. Mazin, “Gap symmetry and structure of Fe-based superconductors,” *Reports on Progress in Physics*, vol. 74, p. 124508, Oct. 2011.

[57] F. Hardy, A. E. Böhmer, L. de’ Medici, M. Capone, G. Giovannetti, R. Eder, L. Wang, M. He, T. Wolf, P. Schweiss, R. Heid, A. Herbig, P. Adelmann, R. A. Fisher, and C. Meingast, “Strong correlations, strong coupling, ands-wave superconductivity in hole-doped $BaFe_2As_2$ single crystals,” *Phys. Rev. B*, vol. 94, p. 205113, Nov 2016.

[58] J. Xing, S. Li, B. Zeng, G. Mu, B. Shen, J. Schneeloch, R. D. Zhong, T. S. Liu, G. D. Gu, and H.-H. Wen, “Power-law-like correlation between condensation energy and superconducting transition temperatures in iron pnictide/chalcogenide superconductors: Beyond the BCS understanding,” *Physical Review B*, vol. 89, Apr. 2014.

[59] M. Eisterer, “Magnetic properties and critical currents of MgB_2,” *Superconductor Science and Technology*, vol. 20, pp. R47–R73, Oct. 2007.

[60] M. Hiraishi, R. Kadono, S. Takeshita, M. Miyazaki, A. Koda, H. Okabe, and J. Akimitsu, “Full gap superconductivity in $Ba_{0.6}K_{0.4}Fe_2As_2$ probed by muon spin rotation,” *Journal of the Physical Society of Japan*, vol. 78, p. 023710, Feb 2009.

[61] J. Hecher, S. Ishida, D. Song, H. Ogino, A. Iyo, H. Eisaki, M. Nakajima, D. Kagerbauer, and M. Eisterer, “Direct observation of in-plane anisotropy of the superconducting critical current density in $Ba(Fe_{1-x}Co_x)_2As_2$ crystals,” *Phys. Rev. B*, vol. 97, p. 014511, Jan 2018.

[62] C. Putzke, P. Walmsley, J. D. Fletcher, L. Malone, D. Vignolles, C. Proust, S. Badoux, P. See, H. E. Beere, D. A. Ritchie, S. Kasahara, Y. Mizukami, T. Shibauchi, Y. Matsuda, and A. Carrington, “Anomalous critical fields in quantum critical superconductors,” *Nature Communications*, vol. 5, Dec. 2014.